# 2D PIV experiments of oscillatory flow in a stenosis

## A study into the physics of flow of cerebrospinal fluid

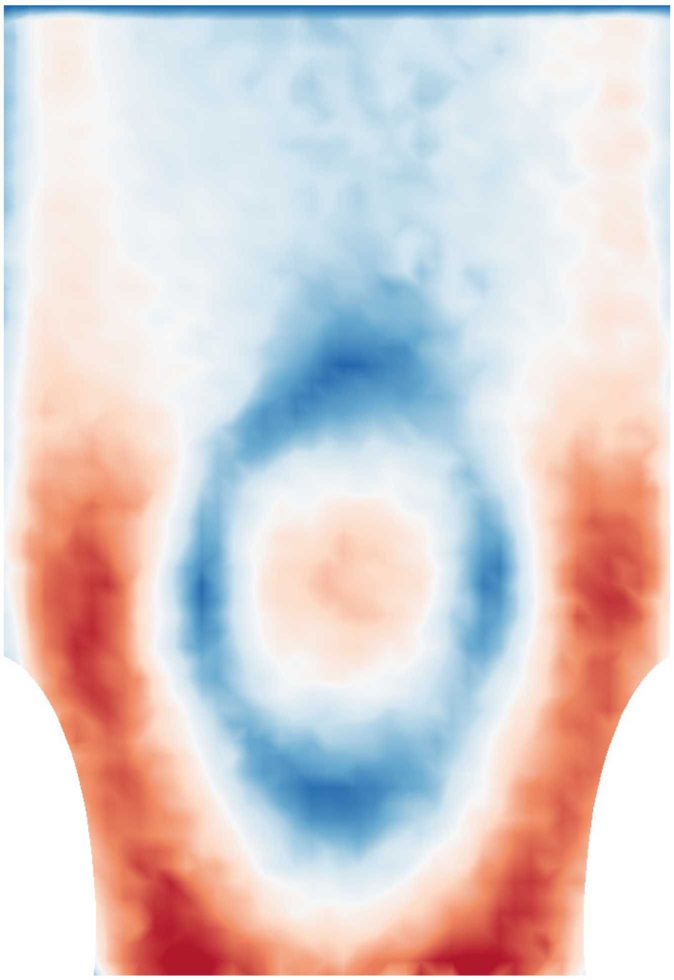

Koen Busink

University of Twente

Document nr. 371

*Graduation committee:*
Chairman: Dr. Ir. R.Hagmeijer
Supervisor: Dr. E. Groot Jebbink
Supervisor: Dr. K. Jain
External member: Dr. A. Marin

*Details:*
2D PIV experiments of oscillatory flow in a stenosis; a study into the physics of flow of cerebrospinal fluid
Document number: 371
K.V. Busink, student number: s1728741
Engineering Fluid Dynamics, Mechanical Engineering, Engineering Technology
University of Twente, Enschede, The Netherlands
Colloquium date June 16, 2021

*Front page*: The vortex ring which is visible during the experiments at $Re_{max}$ = 500.

*"[To] mechanical progress there is apparently no end: for as in the past so in the future, each step in any direction will remove limits and bring in past barriers which have till then blocked the way in other directions; and so what for the time may appear to be a visible or practical limit will turn out to be but a bend in the road."*

Osborne Reynolds

# Abstract

Cerebrospinal fluid (CSF) serves several key functions in the central nervous system, as it protects the brain and spinal cord, clears waste and transports nutrients. Researchers established links between neurological conditions and the flow and composition of CSF. Although these discoveries indicate the importance of CSF, the flow dynamics are still poorly understood. The complex geometry of the brain can even lead to a transition to turbulence in the flow of CSF. In the first part of this research a setup was built and characterized that is representative for the flow of CSF. In the second part oscillatory flow experiments in a stenosis were conducted, to study the flow dynamics and investigate the transition to turbulence.

As CSF is considered an oscillating flow with a zero mean, a setup had to be designed that is able to create this type of flow and that can capture the velocity components. A piston pump was used to create a sine waveform and by using laser particle image velocimetry (PIV) it was possible to extract the velocity data in a straight pipe phantom. The setup has been modified to increase the Reynolds number at which the experiments could be performed and to optimize the sine waveform, to a maximum deviation of 10%. To reduce the required entrance length to ensure fully developed flow, a straw holder has been designed. The highest obtained Reynolds number in the experiments is 2200, at which no signs of a transition to turbulence are observed. The Reynolds number is too low or there is lack of a disturbance, which can be a distorted waveform or geometry, and thus turbulence is not yet triggered in the flow.

In the second part of the research, experiments in an axisymmetric stenosis of 75% were performed. The setup that had been built in the initial part of the research was used to conduct these experiments and study the possible transition to turbulence. A jet is formed, which breaks down in between 2 and 3 diameters downstream of the stenosis and this locations shifts closer to the stenosis throat with increasing Reynolds number. The centerline velocities have been used to plot the power spectral density, and based on these results it cannot be be said conclusively if the flow is in the transitional regime. However, it is clear that at $Re_{max} > 2000$, the flow can be referred to as non-laminar. Completely different and unexpected flow phenomena were observed at $Re_{max} = 500$. There was no jet, but a vortex ring formed just downstream of the stenosis throat which kept moving forwards.

The designed setup can create oscillatory flows up to Reynolds numbers of 2200 and laser PIV is capable of extracting the velocity data. As the conditions in the experiments were not perfect and inaccuracies were introduced into the axisymmetric stenosis, this influences the jet breakdown location and lowers the critical Reynolds number at which the flow transitions. In future experiments the setup can be optimized and more physiological effects of CSF can be implemented, to further increase the knowledge of the flow and the effects on the human body.

# *Acknowledgements*

When I started my master's thesis, I had little to no experience in experimental research and biophysical fluids. Now, nine months later, I have learned so much in the topics of cerebrospinal fluid, oscillatory flows and experimental techniques, which results in this thesis. Even though I spent most time in the lab performing experiments or behind my laptop analyzing data, it definitely feels like a great journey. Fortunately, I did not undertake this journey alone, but I received help from many people.

All the attendees of the weekly flow meeting; you have not only provided valuable feedback, you have also given insights in other research topics and provided a pleasant informal social hour. Guillaume Lajonie in special, for suggesting the straw idea, which led to interesting results and offers a great future research direction. The experimental knowledge from Hadi Mirgolbabaee was indispensable during the production of the phantom and the execution of the experiments. Thanks to both of you, as it definitely improved my research and the content of this thesis.

I want to thank the technicians Martin Bos and Henny Kuipers for brainstorming about the improvements for the setup. The straw holder produced by Martin is magnificent and the stenosed phantom is fantastic due to the printing and design capabilities of Henny.

Erik and Kartik, you have been great supervisors and your enthusiasm really inspired me. During our weekly meetings you provided valuable feedback and suggested new ideas. Your involvement in this research created a pleasant atmosphere, as it felt like a joint research. Erik, I really enjoyed our, unfortunately limited, time in the lab together. Your profound knowledge and experience in the experimental techniques helped me to quickly find my way in the lab and set a research direction. Kartik, your expertise in cerebrospinal fluid and oscillatory flows is amazing. Your research into biophysical flows is fascinating and I am glad that you can now look at your stenosed model in real life. I would never have gotten to this end result without the two of you, thank you so much.

Last, but not least, I want to thank my friends and family, who have not only supported me during my last year of research, but during my whole studies. This thesis marks the end of an incredible time, of which you have been the most important part.

Koen Busink
June 2021

# Contents

# List of Figures

# List of Tables

# List of Abbreviations

| | |
|---|---|
| **ABS** | Acrylonitrile Butadine Styrene |
| **ALS** | Amyotrophic Lateral Sclerosis |
| **BMF** | Blood Mimicking Fluid |
| **CFD** | Computational Fluid Dynamics |
| **CLAHE** | Contrast Limited Adaptive Histogram Equalization |
| **CMI** | Chiari I Malformation |
| **CNS** | Central Nervous System |
| **CP** | Choroid Plexus |
| **CSF** | Cerebrospinal Fluid |
| **DCC** | Direct Cross-Correlation |
| **DFT** | Direct Fourier Transform |
| **FOV** | Field Of View |
| **FPS** | Frames Per Second |
| **IA** | Interrogation Area |
| **ISF** | Interstitial Fluid |
| **MRI** | Magnetic Resonance Imaging |
| **PDMS** | Polydimethylsiloxane |
| **PMMA** | Polymethyl Methacrylate |
| **PIV** | Particle Image Velocimetry |
| **PVS** | Perivascular Space |
| **PSD** | Power Spectral Density |
| **RI** | Refraction Index |
| **ROI** | Region Of Interest |
| **SAS** | Subarachnoid Space |

# Chapter 1

# Introduction

The final goal of this thesis is to experimentally study the fluid dynamics of cerebrospinal fluid (CSF) in an idealized stenosis. Before an experimental setup can be built to investigate the flow of cerebrospinal fluid, background information regarding several topics is needed. In Chapter 2 the theory regarding CSF and Womersley flow, and more specifically, oscillatory flow, is explained. This chapter concludes with theory regarding the used experimental technique, laser particle image velocimetry (PIV). In the third chapter the obtained knowledge is applied to create an experimental setup which can create and visualize oscillatory flow. This knowledge is required before the fluid mechanics in a stenosis under oscillatory flow conditions can be studied, which is the main topic in Chapter 4. Both research directions are briefly introduced below.

## 1.1 Characterizing and building a setup to create and visualize the flow of CSF

One of the vital parts of the central nervous system (CNS) is CSF. This fluid protects the brain and spinal cord and serves several key functions in the glymphatic system [1] [2]. Although this fluid plays an important role in the body, the physiology is poorly understood. Recent research established a link between the composition and flow of CSF and several neurological conditions [3] [4]. This illustrates the importance of a thorough understanding of CSF and its flow in the body.

To better understand the fluid mechanics of CSF, computational oscillatory flow simulations have been performed by Jain et al. [5] [6]. However, there is a lack of experimental knowledge on the fluid dynamics of oscillatory flow and no experimental verification has been performed based on the simulations of Jain. Before these experiments can be performed, a setup has to be designed which is able to create and visualize oscillatory flow. The laser PIV technique is used to experimentally obtain velocity data of oscillating flow in a tube. In Chapter 3 a setup to create and visualize oscillatory flow is proposed and experiments in a straight pipe are performed. These results lay the foundation for the second part of this thesis. The latter results in the following research questions.

- How can a 2D PIV setup be built that is realistic given the conditions of CSF flow in the brain?
- What are the flow dynamics of a sinusoidally oscillating flow in a pipe?
- Up to what Reynolds number can the experiments be conducted?

[1] The glymphatic system is the lymphatic system of the brain. This is a concept that has recently been introduced by researchers and consists of a network of vessels that clears waste from the brain [1].

## 1.2 Fluid mechanics in a stenosis under oscillatory flow conditions

As described in the previous section, CSF is believed to have an impact on a variety of diseases. In several conditions, such as Chiari I Malformation (CMI) in which the cerebellum descends and blocks the spinal cord, the flow of CSF is obstructed which can lead to a wide range of symptoms such as neurological conditions [7]. The flow dynamics of CSF of people with Alzheimer's seem to differ from healthy people [3] and recently links between Amyotrophic lateral sclerosis (ALS) and the flow of CSF have been established [4]. Therefore, it is important to fully understand the impact of an obstruction on the flow of CSF. The brain has a very complex geometry, which can even lead to a transition to turbulence in the flow of CSF [8] [9]. As this onset of turbulence can have a huge impact on the flow dynamics, this is of major importance to understand the role of CSF in the central nervous system.

In this part of the thesis oscillatory flow experiments through a stenosis are performed, to investigate the influence of an obstruction on the fluid dynamics of CSF. As the onset of turbulence is physiologically relevant and of interest in this thesis, the experiments are performed at increasing Reynolds numbers. The setup that is built in Chapter 3 is used to visualize the oscillatory flow through the stenosis in Chapter 4. The following research questions are posed given the background on stenosed CNS channels:

- What are the physics of flow of a sinusoidally oscillating flow in a stenosed pipe?
- What is the Reynolds number at which the flow transitions from the laminar to the turbulent regime in oscillatory flow through a stenosis?

# Chapter 2

# Theory

In this chapter the theory behind the various topics is discussed. It starts with an explanation about CSF, its anatomy, physiology, pathophysiology and its medical relevance. Then the fluid mechanics of oscillatory flow is discussed in detail, as CSF shows a bidirectional flow nature with a net zero displacement. This, together with the theory of the used experimental technique, PIV, provides broad background information that helps to answer the research questions.

## 2.1 Cerebrospinal fluid

Cerebrospinal fluid is a colorless body fluid that flows around the brain and the spinal cord. It has several crucial functions in the central nervous system, it protects the brain and spinal cord from shocks and it removes waste materials. The first mention of CSF is by Hippocrates when examining cases of hydrocephalus (Section 2.1.3) [10]. However, as the physiology and pathophysiology of CSF are still unclear to scientists; a lot of research is conducted into this area. Some conflicting theories have emerged over the years, which will be discussed. In the following sections the anatomy, physiology and pathophysiology of CSF are further explained.

### 2.1.1 Anatomy

In Figure 2.1 the flow of CSF in the brain is displayed. The CSF is contained in the subarachnoid space (SAS) and in the ventricular system inside and around the brain and spinal cord. The cerebral ventricles are four ventricles that are located in the centre of the brain. There are two lateral ventricles (left and right) in the two cerebral hemispheres that are connected by the interventricular foramen to the third ventricle. The third ventricle is located in between both lateral ventricles and is connected to those on the top. The cerebral aqueduct, or aqueduct of Sylvius, is located at the bottom of the ventricle and connects the third and the fourth ventricle. After the fourth ventricle the CSF passes into the SAS through one of the four openings. it can enter the central canal of the spinal cord, the median aperture or one of the two lateral apertures.

The brain and the spinal cord are covered by three different membranes. The first and most outermost layer is called the dura mater. This is a thick and tough layer that protects the CNS. The arachnoid mater is the middle layer, which lays directly under the dura mater and it is a protective membrane. The innermost layer is the pia mater, which is tightly adhered to the surface of the brain and spinal cord. As this layer is very thin, it follows the contours of the brain. These three membranes are called meninges. These are of interest as in between the pia mater and the arachnoid mater, the SAS is located. See Figure 2.2 for an overview of the meninges.

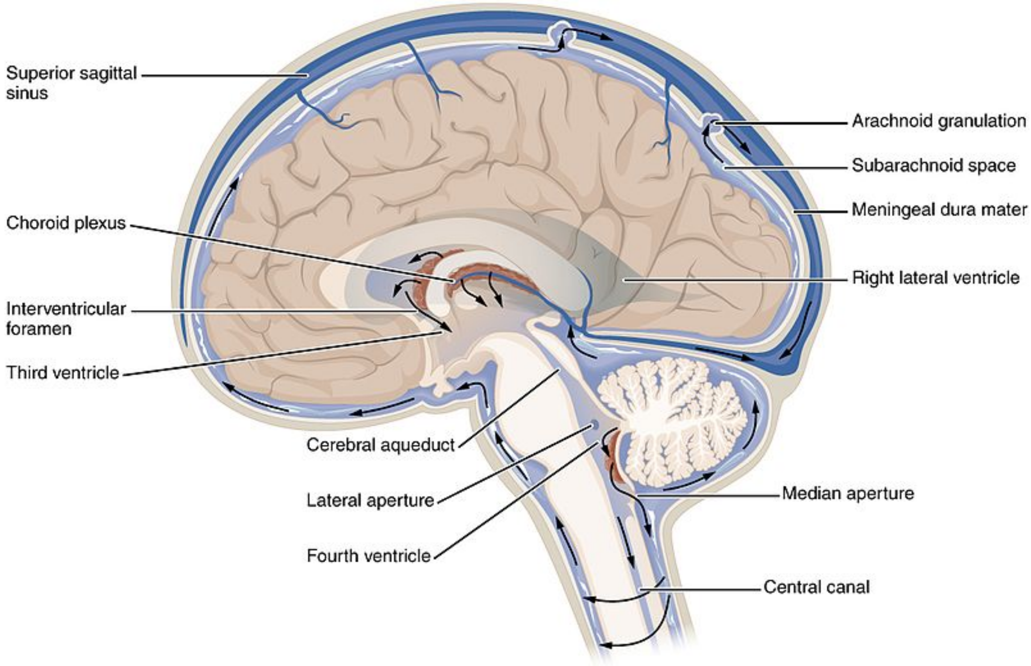


FIGURE 2.1: A schematic overview of the flow of CSF in the brain. Image from Anatomy and Physiology [11]

.

At places where the distance between the arachnoid and pia mater is large, cisterns are located. As described, CSF enters the SAS through the apertures to these cisterns. The blockage of some of these cisterns are of interest as they are associated with certain diseases (see Section 2.1.3).

Inside the four ventricles, the choroid plexus (CP) are located. According to the "classical theory", the CSF is produced in these cells. The CP consists of modified ependymal cells which surround a core of capillaries. Blood is filtered and the fluid that flows through will eventually become CSF. Next to production of CSF, it also serves as a blood-CSF barrier. It removes metabolic waste and regulates the content of CSF. More information and recent theories will be discussed in Section 2.1.4

### 2.1.2 Physiology

#### Function

CSF serves several purposes in the CNS:

1. **Buoyancy**: The mass of the human brain is 1.4-1.5 Kg, but due to the buoyancy of the CSF the net weight of the brain is only 25-50 grams. Otherwise the blood supply in the brain would be cut off and the forces exerted by the brain on the spinal cord would be too high [13].

2. **Protection**: CSF protects the brain tissue and spinal cord from injuries. The CSF acts as a fluid buffer that absorbs shocks from mechanical impact.

3. **Clearing waste**: Metabolic waste products diffuse into the CSF and are absorbed into the bloodstream. Therefore, CSF is one of the important factors in the glymphatic system, a network of vessels that clears the waste in the CNS [14] [15].

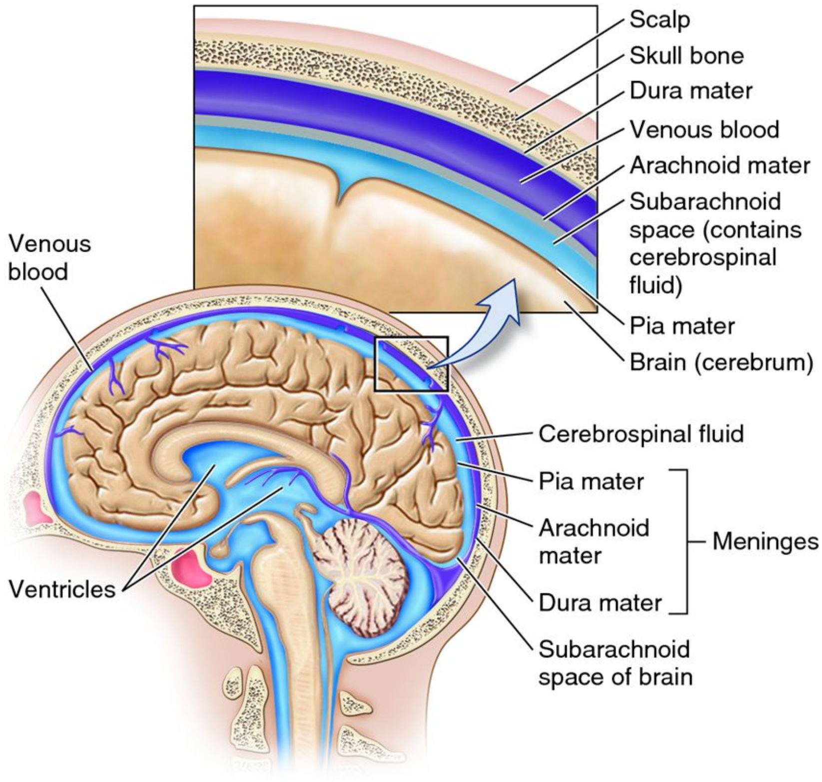


FIGURE 2.2: Schematic overview of the meninges, including the subarachnoid space and the CSF [12].

4. **Homeostasis and nutrition**: CSF is used for the transport of biological substances in the brain. It allows the transport of substances produced in the hypothalamus to all the places around the brain and the spinal cord. The CSF also carries neurotransmitters and neuroactive substances and is thus of vital importance for the neuroendocrine system [16] [17].

**Production and flow**

In the cells in the CP, CSF is produced by filtrating blood plasma. CSF is mainly composed of water with a small amount of other substances such as proteins, chloride, potassium and sodium. In depth information regarding the composition of CSF can be found in Spector et al. [1]. Due to the nature of CSF, the physical properties of CSF are the same as those of water at 37 °C. This means that it is a Newtonian fluid with density ($\rho$) = 1000 $\frac{kg}{m^3}$ and dynamic viscosity ($\mu$) = 0.7 x $10^{-3}$Pa·s. The CSF is produced in the CP and absorbed into the circulating blood flow in the arachnoid villi [5]. This reabsorption is driven by a pressure difference between the CSF in the SAS and the blood in the dural sinus.

According to the classical theory about CSF introduced by Cushing [18], CSF circulates and it is known as the third circulation [2]. This theory was widely accepted over the years and it assumed CSF circulation through the ventricles and the SAS after which it was reabsorbed in the arachnoid villi. New research led to the insight that this theory has its limitations. These theories will be discussed in Section 2.1.4

[2]The other two circulations are the cardiovascular and lymphatic system

As CSF is continuously produced and absorbed, the net flow of CSF is nearly zero. There are two main factors that are believed to drive the flow of CSF. The first, and biggest contributor is the cardiac cycle. The expansion and contraction of cerebral arteries drives the CSF in a pulsatile manner [5]. The second, and smaller, contribution is attributed to the respiratory system [19].

### 2.1.3 Pathophysiology

Different pathological conditions are associated with CSF. Three of those, Chiari I Malformation (CMI), Syringomyelia and hydrocephalus, will be described as they are of interest for this thesis.

#### Chiari I Malformation

Chiari I malformation is the most common type of Chiari malformation, which affects about one in thousand people [7]. The neurological symptoms associated with Chiari I malformation are caused by the herniation of cerebellar tissue through the foramen magnum. Although the first descriptions on Chiari I are in the 19th century, it was not until the 1970s that research led to new insights. Scientist discovered that CSF was not able to move out of the fourth ventricle into the spinal cord [20] [21]. Different symptoms are associated with CMI, ranging from symptoms related to CSF obstruction to spinal cord dysfunction [22]. The obstruction of CSF can lead to headache and hydrocephalus, which is discussed in Section 2.1.3. Other symptoms related to the dysfunction of the brainstem, cerebellum and spinal cord cover a wide range of neural activities such as motor neuron signs, vision, dizziness and hearing [7].

In Figure 2.3 a schematic overview of Chiari I malformation is displayed. The tonsillar herniation can lead to a higher pressure on the spinal cord and thus an obstructed CSF flow. Imaging techniques such as MRI lead to more diagnosis of CMI nowadays, as it was hard to discover. As mentioned before, the symptoms are very broad and can be associated with various other pathological conditions. It is estimated that 1 in every 1000 persons has CMI. However, as most cases are asymptomatic and the symptoms vary, this number might be higher [7]. Surgery is used to restore the CSF hydrodynamics by enlarging the space for the cerebellum. But the exact influence of CMI on CSF hydrodynamics is unknown [5].

#### Syringomyelia

Syringomyelia is a condition that is often associated with CMI [22] [24]. Fluid filled cavities, syrinxes, form in the spinal cord tissue and can cause a range of neurological conditions. In Figure 2.3 a case of CMI and Syringomyelia is displayed.

The development of syrinxes in the spinal cord can have different causes. The abnormal CSF pressure, due to a stenosis, can lead to the formation of Syringomyelia [25]. This is believed to be the reason why a Syringomyelia is common in patients with CMI. Trauma and hemorrhage can also lead to syrinx formation [20]. The complex fluid-structure interaction in spinal cord and spinal SAS make it difficult to understand the CSF hydrodynamics. It is believed that the presence and the location of the stenosis and syrinx have a large impact on the pressure [25]. The location of the syrinx in the spinal cord determines the symptoms associated with the disease. This includes chronic pain and muscle weakness.

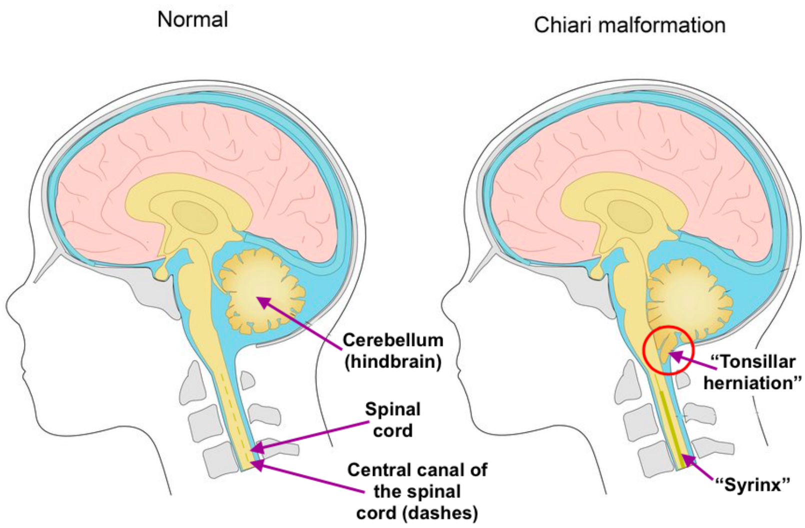


FIGURE 2.3: Schematic of a person with Chiari I malformation, image from CNS Neurosurgery [23]. On the left a healthy person is displayed, the cerebellum is located in the correct position and the CSF can flow freely. The person on the right suffers from Chiari I malformation, due to which the flow of CSF is blocked by the tonsillar herniation. Syringomyelia is displayed in the spinal cord, which is a fluid filled cavity.

#### Hydrocephalus

Hydrocephalus leads to an increased pressure in the skull caused by the accumulation of CSF in the brain. This accumulation is the result of an imbalance between CSF production and absorption. The condition can occur due to birth defects or be acquired later in life. Hydrocephalus can arise from a variety of conditions: brain tumours, meningitis and hemorrhage.

Hydrocephalus can be classified into two categories: communicating and non communicating. In communicating hydrocephalus there is a free CSF flow to the SAS but an impaired CSF reabsorption. Therefore, the CSF is not absorbed at the same rate as it is being produced [26]. Neurological conditions can result in an impairment of the arachnoidal granulations, which are the sites of the CSF reabsorption. Noncommunicating hydrocephalus, also known as obstructive hydrocephalus, is caused by an obstruction in one of the passages from the ventricles. Without treatment, permanent disability or even death may occur. But most cases can be treated by the placement of a shunt.

### 2.1.4 New research

The traditional theory of CSF physiology is based on animal experimentation, which led to the concept of the "third circulation". However, recent research led to different insights on the CSF physiology, which challenges several aspects of the classical theory [27]. This includes the rate and location of the CSF formation and absorption, which was primarily believed to occur in the choroid plexus and the arachnoid villi respectively.

An extensive historical overview of the controversies regarding CSF has been given by Mantovani et al. [28]. Here they show the misconceptions regarding the production of CSF, absorption of CSF and the most important factor for this thesis, the CSF flow. In the classical theory a unidirectional flow of CSF is described by Cushing [18], which led to the term "third circulation". Extensive research by Orešković & Klarica [29] provides new theories about the production location and the direction of the flow. They state that the idea that CSF is only produced in the CP in the ventricles, then flows unidirectionally through the SAS to be passively absorbed by the arachnoid villi is incorrect. Their theory states that CSF is produced and absorbed inside the entire CSF system [29]. Water is filtered and absorbed through the capillary walls into the interstitial fluid (ISF) of the surrounding brain tissue [30]. This new theory contradicts the classical theory, as there is no unidirectional "circulation". This new theory suggests that CSF flows bidirectionally along the CSF spaces, it oscillates with a net movement of zero. Therefore, they propose to no longer use the term CSF circulation, but CSF flow or CSF movement [30].

Around the blood vessels in the brain, the perivascular space (PVS) is located. These are channels that are filled with CSF and they play an important role in the waste clearance from the brain [15]. A schematic overview of the PVS is shown in Figure 2.4.

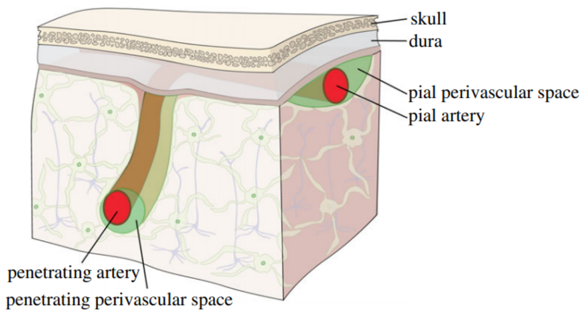


FIGURE 2.4: Schematic of the PVS around arteries in the brain. Image copyright from Thomas [15]

Recent research showed that these PVS play an important role in the movement of CSF. Hadaczek et al. [31] introduced the term perivascular pumping to describe the flow. The heartbeat creates arterial pulsations that lead to a peristaltic flow. Research by Mestre et al. [32] proves that the flow of CSF in PVS is driven by oscillations of the artery wall due to the heartbeat and the net flow is in the direction of the blood flow. According to Mestre et al. [32], the cardiac cycle is the driving factor of CSF movement, which confirms the results from Friese et al. [19].

In the research from Ladrón-de-Guevara [33], results from theory, experiments and simulation are all consistent and prove that perivascular pumping is the main driver in the flow of CSF. However, as this is an emerging area, more research into the driving mechanisms of the flow is needed. The movement of CSF differs at every location in the SAS and spinal cord, due to differences in anatomy [34].

For more background information regarding CSF and its fluid dynamics, the reader is referred to Thomas [15] Brinker et al. [27], Orešković & Klarica [29], Mestre et al [32] and Ladrón-de-Guevara et al. [33].

**Medical relevance**

The knowledge of CSF has increased considerably in recent years. The PVS and CSF are now viewed as an option to deliver drugs into the brain tissue. A very detailed overview of CSF and drug delivery is written by Kouzehgarani et al. [35].

Recent research also establishes a link between various neurological diseases and the flow of CSF. One of the important roles of CSF is the clearance of waste in the brain, such as the protein amyloid-$\beta$. High levels of this protein may be a cause of neurological diseases such as Alzheimer's [3]. In recent research, altered CSF dynamics are linked to Alzheimer's disease [36] [37].

Recently a correlation was found between CSF and amyotrophic lateral sclerosis (ALS), which is a progressive neurodegenerative disease. MRI research showed that the CSF flow in patients with ALS is disrupted [4]. Researchers found a delay in CSF flow at systole and a higher maximum velocity than in healthy patients. Other research confirms the influence of the glymphatic system on different aspects of ALS and the relationship with CSF flow [38] [39].

Even though the recent advancements show great results in the understanding of CSF and its flow, researchers are also unanimous that more research is needed. As more information on the CNS, CSF and associated diseases are known, more questions regarding the nature of the flow arise.

## 2.2 Oscillatory flow

A detailed description of the flow of CSF is given Section in 2.1. The overall motion of CSF is considered to be oscillatory, in both the SAS and PVS. As there is no net movement of the fluid out of a particular section, it is a zero-mean flow.

In this thesis oscillatory flow in a simple, but yet anatomically relevant geometry is studied. Two different geometries have been investigated: a straight tube and a tube with a stenosis. The periodic variations in the flow lead to a pulsatile flow, which is also known as Womersley flow. In this chapter Womersley flow and in particular oscillatory flow with a zero mean, will be discussed. Furthermore, relevant research regarding pulsatile flow, oscillatory flow and the transition to turbulence will be elaborated on.

### 2.2.1 Womersley flow

Flow with periodic variations are named after J.R. Womersley, who was the first to derive the pulsatile velocity profiles [40]. The pulsatile velocity profiles depend on the Womersley number, which is denoted by $\alpha$:

$$\alpha = L\left(\frac{\omega\rho}{\mu}\right)^{\frac{1}{2}} \tag{2.1}$$

This is a dimensionless expression of the pulsatile flow frequency in relation to the viscous effects. L is the characteristic length, $\omega$ is the angular frequency, $\rho$ is the density and $\mu$ the dynamic viscosity of the fluid.

For small values of $\alpha$, the viscous forces dominate the flow. This results in a parabolic velocity profile. If $\alpha \geq 2$, the velocity profile will be flatter. In this case the viscous forces will still dominate near the boundary layer, but the inertial forces dominate in the centre of the flow. The pulsatile velocity profile in a straight pipe can be described by:

$$u(r,t) = \mathrm{Re}\left\{\sum_{n=0}^{N}\frac{iP'_n}{\rho n\omega}\left[1-\frac{J_0\left(\alpha n^{1/2}i^{3/2}\frac{r}{R}\right)}{J_0\left(\alpha n^{1/2}i^{3/2}\right)}\right]e^{in\omega t}\right\} \tag{2.2}$$

For more information on how to derive this equation and background information regarding the analytical solution, the reader is referred to Womersley [40], Mirgolbabaee [41] and van de Vosse [42].
In Figure 2.5 the analytical Womersley profiles are plotted for different values of $\alpha$. As described, for low values of $\alpha$, the profile is parabolic and for high values of $\alpha$ the profile is more plug-like.

### 2.2.2 Entrance length

The entrance length is the distance a fluid needs to travel after entering a pipe before it becomes fully developed. At a certain distance the boundary layers merge on the centerline of the pipe and the flow is fully developed. The characteristics of the flow will no longer change along the flow direction of the pipe.
The entrance length for a laminar oscillating pipe flow can be estimated by [43] [44]:

$$L_e = 0.03 \cdot Re \cdot D \tag{2.3}$$

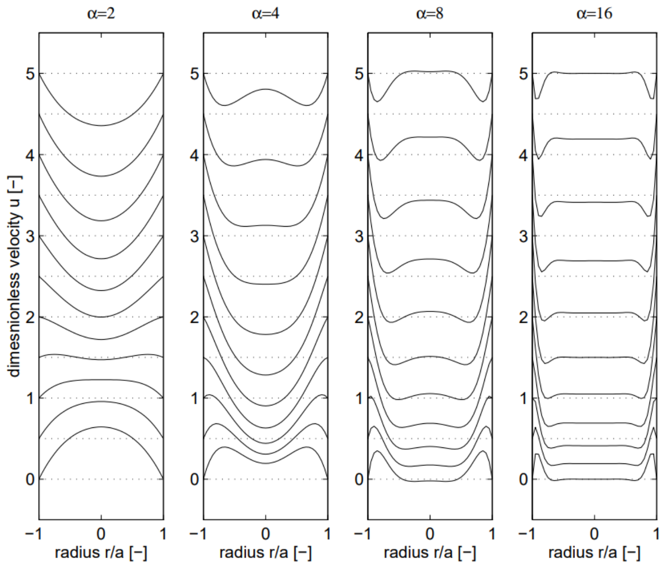


FIGURE 2.5: Womersley profile of pulsating flow in a pipe for different Womersley numbers. The circular cross sectional profiles are displayed in a 2D plot. Image from van de Vosse [42]

In this equation $L_e$ is the required entrance length, $D$ the diameter of the pipe and $Re$ the Reynolds number, which is $\frac{\rho U D}{\mu}$. By rewriting this equation and inserting the Reynolds number in Equation 2.3, the following form is obtained:

$$L_e = 0.03 \cdot \frac{4}{\pi} \frac{\rho}{\mu} \cdot Q \tag{2.4}$$

As can be seen in this formula, the entrance length of the pipe is dependent on Q, the volumetric flow rate. Thus to decrease the entrance length of the pipe, the volumetric flow rate has to be decreased.

### 2.2.3 Relevant research

Due to the growing interest from the medical field in pulsatile and oscillatory flows, more research is being conducted. In this section an overview of pulsatile and oscillatory flow research is discussed, which are of interest for the cardiovascular and glymphatic system respectively. In this thesis, oscillatory flow with a zero mean is the most important, as this represents the flow of CSF. However, due to a large number of similarities and the often accompanied research of pulsatile flows, this is included in this section. Furthermore, a distinction is made between flows in a straight pipe and pipes with a stenosis.

#### Straight pipe flow

Çarpinlioğlu et al. [43] described four stages in the transition from the laminar to the turbulent regime in an oscillating flow.

1. During the early accelerating phase disturbed flow with small amplitude perturbations will appear

2. Small amplitude perturbations persist in the high velocity phase

3. Turbulent bursts occur in the deceleration phase

4. Turbulent bursts may also occur in the accelerating phase, leading to an almost uniform distribution of the turbulent bursts in the velocity wave form. However, acceleration of the flow field stabilizes the flow due to reduction in pressure gradients. This will be further explained in the next paragraph.

Çarpinlioğlu et al. based their stages on previous research, which investigated the onset of turbulence in oscillatory and pulsatile flows:

Hino et al. [45] performed experiments on the transition to turbulence in a purely oscillatory flow. They detected three types of turbulent flow regimes: weakly turbulent flow, conditionally turbulent flow and fully turbulent flow. At low Reynolds numbers there are small amplitude perturbations superposed in the laminar velocity profile, which is called weakly turbulent flow. They found that with an increasing Womersley number, the first transition is observed at a lower Reynolds number. At higher Reynolds numbers, the second type of turbulence is observed; fluctuations arise at the peak of the velocity profile. These disturbances have a higher amplitude and lower frequency than the first type of turbulence described above. As this turbulence only appears in the decelerating phase and it stabilizes during the reversal and accelerating phase, it is called conditional turbulence. During this relaminarization process the turbulent energy that is generated in the decelerating phase is transferred back to the main flow [44]. Their comparison with theoretical results shows a large deviation with experiments, which can be attributed to non-perfect conditions in experiments. In a follow up research from Hino et al. [46] they studied the turbulence in an oscillatory flow. The same types of turbulence are confirmed as in their previous research. In the deceleration phase, they observed that the spectral decay shows similarities to the $\frac{-5}{3}$ decay of Kolmogorov, which indicates high energy dissipation.

Ohmi [47] investigated the transition to turbulence in a pipe flow for both pulsatile and oscillatory flow. He discovered that in pulsatile flow that reverses in direction and shows signs of relaminarization, the physical phenomena are comparable as in an oscillatory pipe flow with a zero mean. The fluid is accelerated and will burst into chaotic motion, which will be repeated every cycle. Whether or not the relaminarization takes place is an important difference between these flows. As in the flows where relaminarization occurs, the velocity distribution can be described by a transient pulsatile flow, while in the turbulent phase the 1/7 power law can be used.

Xu et al. [48] described three regimes in which the transition to turbulence in a pulsating pipe flow can be classified. The first regime is in the high frequency limit, with $\alpha \geq 12$, the flow pulsation does not influence the transition threshold. They assume that the flow rate changes too fast for the turbulence to react. Instead, when the average Reynolds number is equal to the steady flow threshold, turbulence will become sustained.
The second regime is for low Womersley numbers, $\alpha \leq 2.5$. In this case the changes in Reynolds numbers are lower and the turbulent structures are able to adjust to the instantaneous Reynolds number.
In between $2.5 \leq \alpha \leq 12$ the transition adjusts smoothly between the two above mentioned limits.

Recent research by Feldmann et al. [49] and Xu et al. [50] confirms that the instability occurs during the deceleration phase of the cycle. Only small perturbations, such as geometric deviations, are needed to trigger the transition. In their research they investigated the role of helical mechanisms, which play a role in the transition to turbulence [51]. These helical disturbance are more important at high pulsation amplitudes and are triggered by small imperfections [50].

Experimental research into the transition to turbulence and relaminarization in pulsatile flows was conducted by Gomez et al. [52]. They analyzed pulsatile flows that involve flow reversal and studied their phenomena in the transition phase. They performed experiments in a straight tube at different Reynolds and Womersley numbers. At low Reynolds numbers, Re = 535 and 1140, they found that there is confined turbulence in the near-wall region. At higher Reynolds numbers the flow decelerates further which leads to turbulence characteristics in the whole flow field. During the acceleration phase of the flow there are asymmetries between the top- and lower-wall regions, which reduces when the flow accelerates. With increasing Womersley number there seems to be no relaxation time for the turbulence and thus a completely turbulent flow is obtained.

**Pipe flow with a stenosis**

Barrere et al. [53] investigated vortex dynamics under pulsatile flow in axisymmetric constricted tubes. The flow pattern consists of two main structures. A central jet around the axis which develops in the stenosis and a re-circulation zone close to the wall, where vortices shed.

Ahmed & Giddens [54] studied the physics of pulsatile flow in a tube with an axisymmetric stenosis. They found that turbulence only occurs in models with a high degree of stenosis, with an area reduction of 75%. The models with a stenosis of 25% and 50% showed a stable flow. In the model with 75% stenosis they noticed different forms of disturbance, however, turbulence only occurs further downstream of the stenosis, in the deceleration phase. Furthermore, they compared the centerline velocity up- and downstream of the stenosis. In their results they show that the higher the degree of stenosis, the higher the velocities downstream of the stenosis. However, the centerline velocities remain relatively constant in the post-stenotic field for all degrees of stenosis. Further downstream, the centerline velocity decreases to the upstream velocity value.

Varghese et al. [55] studied the flow through axisymmetric and eccentric stenosis models. These models match the geometry of the research from Ahmed & Giddens [54]. They concluded that at the same Reynolds numbers the flow would stay laminar in the axisymmetric case, but the introduction of an eccentricity in the stenosis resulted in jet breakdown and a periodic, local transition to turbulence. This transition to turbulence occurred during the deceleration phase. During the mid-deceleration phase the inlet flow lost its momentum and the turbulent intensity reduced, which leads to relaminarization of the flow.

Research by Samuelsson et al. [56] confirms that the introduction of a slight eccentricity (0.3% of the pipe diameter) can strongly decrease the Reynolds number at which the flow becomes unstable. This is an important finding as slight inaccuracies in experimental models are inevitable, while numerical models can be perfectly symmetrical. This can lead to a difference in results for comparable research. Thus, it is more likely to observe unsteady flow and a transition to turbulence in experiments than in numerical simulations, as the critical Reynolds number is lowered due to asymmetries in the model.

Jain [57] looked into the transitional flow regime of a steady flow in a FDA (US Food and Drug Administration) nozzle. The aim was to investigate the transition to turbulence and compare the obtained numerical results to the experimental data. Even though some flow phenomena are different in a steady than an oscillating flow, the methods that are applied are useful for this thesis. By comparing the centerline velocity along the axial profile of the pipe, the breakdown location of the jet can be determined. Turbulent activity can be investigated by using a power spectral density (PSD) plot, as in the research from Hino et al. [45].

Steady and pulsatile flows through stenosed tubes were experimentally and numerically investigated by Trigui et al. [58]. Their experiments showed good agreements with their computational models for both steady and pulsatile flows. They analysed two axisymmetric geometries of a 50% and 75% reduction in diameter. The stenosis drastically increases the velocity of the flow and creates a plug shaped profile. The stenotic jets and separation region extend to 2.5D downstream of the phantom in the 75% stenosis case with pulsatile flow. During several phases the flow reversal is visible, where the central core moves forward but the fluid near the wall has reversed in direction. Recirculation zones can be seen on both sides of the central core.

**CSF flow research**

During the last decades computational fluid dynamics (CFD) has been increasingly used to predict fluid flows. This is a widely used tool to investigate complex biomedical flows, such as the flow of CSF. In Section 2.1 various conditions are described in which the flow of CSF is obstructed. Helgeland et al. [9] investigated the flow of CSF in the SAS in a patient with CMI. Most studies assume that the flow of CSF is laminar, as the Reynolds number ranges from 150-700 [9]. However, due to the oscillating flow and complex geometries in the canals, higher Reynolds numbers can occur locally. At these locations, the flow is very close to a transition to turbulence. Slight disturbances such as an increase in velocity or frequency can trigger turbulence in the flow. According to this research, it is likely that there is a transition to turbulence in the flow of CSF. However, much is still unclear about the transition to turbulence, especially in oscillatory flows.

Jain et al. [6] researched the hydrodynamics of CSF in patients with CMI, in which the CSF dynamics are altered due to an obstruction in the SAS. They conclude that even though the Reynolds numbers are low, the flow seems to transition from laminar to turbulent. Due to the complex geometry of the SAS and the bidirectional flow nature, the critical Reynolds number is decreased. However, due to the nature of CSF flow, which has a net volumetric rate of almost zero, the turbulent kinetic energy that is produced in the forward phase decreases again in the backwards flow [45]. Thus, it is not likely that fully developed turbulence will occur in these flows [47].

In the research from Helgeland et al. [9] and Jain et al. [6] the same flow phenomena were observed as in a tube with an oscillatory flow. The transition occurs during the deceleration phase and during the acceleration phase the flow relaminarizes. The severity of the CMI influenced the fluctuations, as the flow was more disturbed. According to Ahmed & Giddens [54] the degree of stenosis was of great influence on the transition, which is displayed by these results. However, the physical phenomena behind the transition to turbulence are still unclear.

Simulations of oscillatory and pulsating flow through a pipe with a stenosis were performed by Jain [5]. The geometry of the model in that research is similar to Ahmed & Giddens [54] and Varghese et al. [55], and includes an axisymmetric and an eccentric stenosis. He discovered that the critical Reynolds number is 3 times

higher in a purely oscillating flow compared to pulsatile flow in the same geometry. In the oscillatory flow the turbulent fluctuations decay rapidly, as the flow lost its momentum due to the reversal of the flow. In the pulsatile flow the disturbances in the flow are noticed further away from the stenosis throat. The same conditionally turbulent flow is observed as in previous research mentioned earlier.
More simulations of an oscillatory flow through stenosis were performed by Jain [8]. Two different geometries with an axisymmetric and eccentric stenosis of 75% were used to investigate the transition to turbulence. He found that the flow transitions at a lower Reynolds number when an eccentricity is introduced and the intensity of the fluctuations is higher. This is a confirmation of the results of the simulations in the SAS [6], where flow transition was observed, even though the Reynolds numbers were considerably lower than the generally accepted threshold. The pulsation frequencies did not influence the critical Reynolds number, but the location of flow breakdown and stabilization were affected as they shifted closer to the stenosis throat as the frequency increased.

## 2.3 Particle image velocimetry

This section starts with an introduction to particle image velocimetry (PIV). It explains the historical context and applicability of the technique. The techniques behind PIV, including the post-processing and the used algorithm are discussed.

### 2.3.1 Introduction and historical context

The moving patterns of fluids are of interest in many different application areas. This ranges from water flow around a ship, to blood flow in a vessel and air flow around an airfoil of a plane. Even though fluid mechanics have been studied for centuries, the addition of particles to a fluid to study its flow is relatively recent. In the early 20th century Ludwig Prandtl was the first to use particles to study the flow of fluids. He designed an experimental setup in which he could study the process of flow separation, see Figure 2.6a. By adding small particles into a water flow he could visualize flow separation in his water tunnel. By taking pictures of the flow he acquired the first time resolved PIV images.

His method of adding additives to a fluid became a wide spread method to visualize the flow, as in this way scientists were able to qualitatively study the flow characteristics. As researchers were interested in quantitative measurements, they developed several particle based methods to quantify the flow. Some of these methods include laser Doppler velocimetry, particle tracking velocimetry and particle image velocimetry (PIV) [59]. In these methods the fluid is seeded with tracer particles, which are assumed to follow the flow (see section 2.3.3). By using a light source the particles will become visible and the motion of these particles can be used to quantify the flow. An extensive description of all flow visualization methods is given by Tropea et al. [59], where in-depth information is provided by the author. In this research PIV is used to quantify the flow during the experiments, thus this method will be discussed in the upcoming sections.

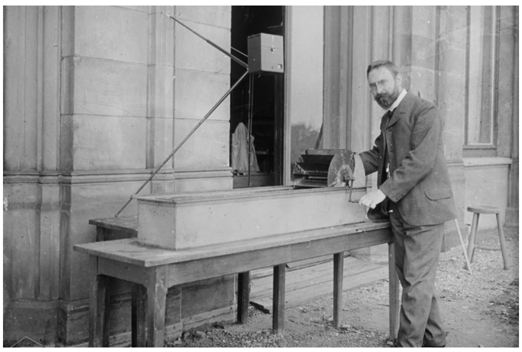

(A) Prandtl in front of his water tunnel

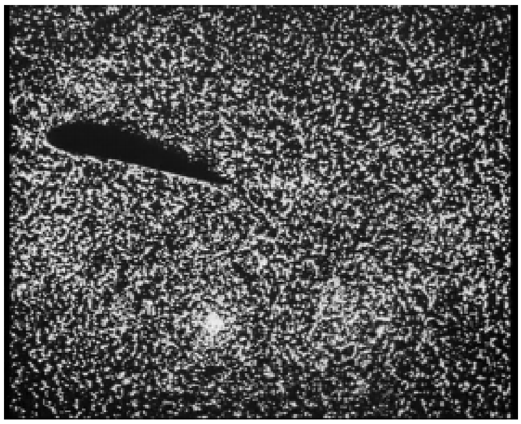

(B) One frame of the airfoil.

FIGURE 2.6: One of the first visualization methods designed by Prandtl. Images from DLR [60] and Willert et al. [61]

As computing power has increased significantly in recent decades, PIV has become the most widely used technique. This has led to new insights and improvements of the technique, which were unknown back in the days of Prandtl. Even though Prandtl was the first person to introduce the concept of PIV, he was not able to quantify the flow characteristics. Researchers have studied the pictures he took a hundred years ago and found that the seeding and quality of images is sufficient for modern PIV analysis techniques [61]. An example of Prandtl's experiment with flow around an airfoil can be seen in Figure 2.6b, where the homogeneous particle distribution is clearly visible. This illustrates the high quality of his experiments and the huge potential of the PIV technique.

### 2.3.2 PIV technique in oscillatory and turbulent flows

In this thesis, research was conducted into oscillatory flows as this type of flow represents the movement of CSF. The onset to turbulence in the flow of CSF is physiologically relevant and is therefore studied in the experiments. Particle image velocimetry (PIV) and holographic particle image velocimetry (HPIV) are able to compute the velocity field in 2D and 3D, respectively. By only using one camera, the out-of-plane component of the velocity is difficult to determine. Other techniques such as stereoscopic PIV and Tomographic-PIV involve more cameras and are therefore better suited to obtain all three components of the velocity field. In this research a 2D-2C PIV setup is used, this limits the possibilities to capture 3D data which is especially relevant in the highly 3D velocity field in the turbulent regime. Even though the use of a 2D-2C setup has its limitations, Ayegba et al. [62] state in their research that 2D velocity vector fields provide useful information in the turbulence regime.

### 2.3.3 Hardware

A schematic of a typical PIV setup can be found in Figure 2.7. The hardware of the setup consists of a camera, light source and the tracer particles which are added to the fluid. In the upcoming sections the requirements and theory of these components are explained.

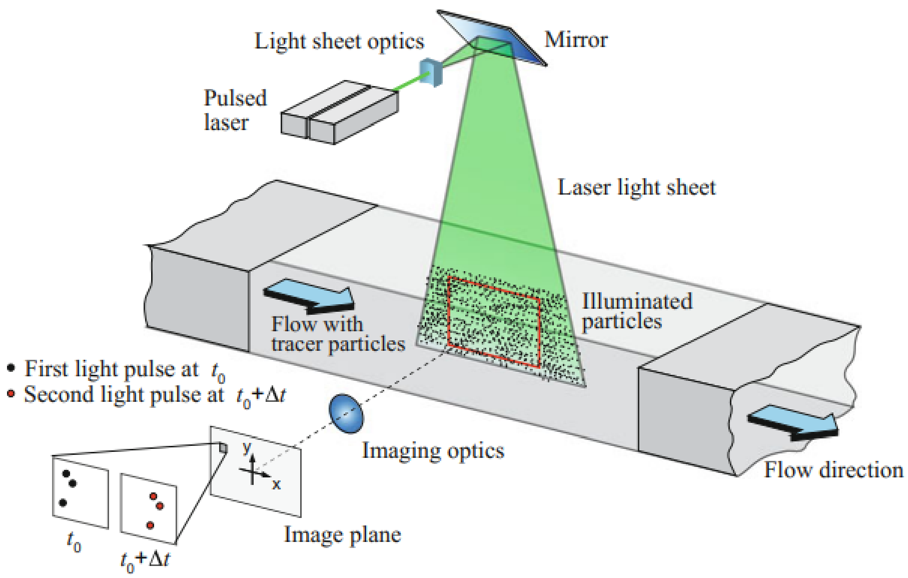


FIGURE 2.7: Schematic of a Particle Image Velocimetry (PIV) setup, image from Raffel et al. [63]. The picture displays the hardware that is used and the general idea of the PIV analysis

### Camera and light source

As explained in the introduction, the principle of PIV is based on recording the motion of the tracer particles. In order to visualize the particles, a laser is used. By using the right optics, a thin laser sheet can be created which illuminates the particles in the flow. The illuminated particles can be recorded by using a high-speed camera, which is positioned perpendicular to the laser sheet. The movement of the particles can be captured by recording several frames.

These images can be used to determine the velocity of the particles (and thus the flow field), by measuring the traveled distance between two consecutive images. The setup and the principle of how the data is extracted from the images is shown in the Figure 2.7.

### Tracer particles

During PIV measurements the velocity of the tracer particles is determined, instead of the velocity of the fluid itself. It is assumed that the tracer particles follow the flow faithfully, thus the motion of the particles represents the motion of the flow. However, this assumption is not always valid. Therefore, a careful examination of the properties of the fluid and the particles is required, to avoid undesirable interactions. These properties can be defined by the characteristic times. The characteristic time of the carrier fluid, shown in Equation 2.5 and the relaxation time of the particle, shown in Equation 2.6. In these equations $L_c$ is the characteristic length of the fluid flow, $U_f$ the velocity of the fluid, $d_p$ is the particle diameter, $\rho_p$ is the density of the particle and $\mu_f$ is the viscosity of the fluid [63].

$$\tau_f = \frac{L_c}{U_f} \tag{2.5}$$

$$\tau_p = \frac{\rho_p d_p^2}{18\mu_f} \tag{2.6}$$

A widely used indicator for the traceability of the particles is the Stokes number, which is defined in Equation 2.7 [64]. The Stokes number is the ratio of the characteristic times of the flow and particles and gives an indication of the ability of a certain particle to track the flow. Based on the magnitude of the Stokes number, a decision can be made if the chosen particle is able to closely follow the motion of the carrier fluid. For low Stokes numbers, the particle is able to respond quickly to changes in the flow. However, for large Stokes numbers the tracer particle is not able to respond to rapid changes in the motion of the fluid. Particles with a $\mathrm{St} < 0.1$ have an acceptable accuracy and are thus suitable as a flow tracer [63].

$$St = \frac{\tau_p}{\tau_f} = \frac{\rho_p d_p^2 U_f}{18\mu_f L_c} \tag{2.7}$$

The effects of the buoyancy on the particles can be expressed by using the Archimedes number:

$$Ar = \frac{g d_p^3 \rho_f \left(\rho_p - \rho_f\right)}{\mu_f^2} \tag{2.8}$$

In which $\rho_f$ is the density of the fluid and g the acceleration gravity constant. An appropriate value for the Archimedes number is if $\mathrm{Ar} < 5 \cdot 10^{-2}$ [64].

Besides, the tracer particles have to be captured by the camera and thus the optical properties of the tracer particles are important as well. The refractive index of the tracer particles should be different from the fluid, such that the laser sheet will reflect off of the particles and this light can be captured by the camera.

The desired Stokes and Archimedes numbers can be achieved by either choosing a small diameter, or choosing neutrally buoyant particles. However, when the particle diameter is too small, the scattered light can become too weak. Therefore, a proper tradeoff must be made between all options. Tracer particles for liquids flow are usually in an order size of 10-100 $\mu$m [63].

The number of spurious vectors in PIV data drops as the seeding density increases [65]. There is however a maximum, as a very high seeding density can alter the characteristics of the flow and make it difficult to distinguish particles in the region of interest. Tropea et al. gives an indication of a 0.05 particles/pixel.

### 2.3.4 Software

To quantify the data recorded by the images, PIV analysis software is used. For this research, a modified version of the PIVlab toolbox in MATLAB is used to perform the PIV analysis [66] [67]. This section provides a brief overview of the theory involved in PIV analysis. For more in depth information, the reader is referred to Tropea et al. [59], Raffel et al. [63], Thielicke et al. [66] and Westerweel et al. [68].

#### Masking

As not the whole field of view (FOV) of the recorded images will be investigated, a region of interest (ROI) is determined. Regions that are not of interest for the PIV analysis will be masked. In this case the regions where no fluid is passing will be masked. After masking certain areas of the FOV, the ROI, which contains the flow field, remains. The ROI is used as input for the PIV analysis. In this research simple geometries are used, thus the ROI can be selected by using rectangles or splines. More advanced methods will be discussed later in Section 3.7 .

#### Image pre-processing

To decrease the error in the PIV data resulting from incorrect velocity vectors, preprocessing of the data is performed. Different techniques are available to improve the quality of the images before performing the PIV analysis. Several pre-processing filters are implemented in PIVlab [67].

The contrast limited adaptive histogram equalization (CLAHE) is used as a preprocessing step in this research, and will be briefly explained.
To improve the readability of medical imaging, Pizer et al. [69] proposed the CLAHE filter. By using this filter the regions in the captured image with high and low exposure are optimized independently. This is achieved by dividing the image in a number of small tiles. In these regions the most frequent intensity of the histogram is spread out within that region. To prevent visible boundaries after the histogram equalization, interpolation is used to combine the neighbouring regions.

This filter can be also be applied in other digital imaging areas, such as PIV analysis. The Gaussian intensity distribution of a laser beam can lead to a non-uniform exposure of the ROI. By using the CLAHE filter, the influence of this effect can be reduced [70].

### PIV algorithm

The most essential, but also sensitive, part of the PIV analysis is the used algorithm. To quantify the data from the captured images and obtain the velocity data, the images are divided into smaller regions which are called interrogation areas (IA). The most probable particle displacement between two consecutive frames is obtained by employing the cross-correlation technique [71] [72]. According to Thielicke et al. [66] the cross-correlation is a statistical pattern matching technique. It tries to find the particle pattern from interrogation area A in interrogation area B [3]. By using the discrete cross correlation function this statistical technique can be implemented: [73]

$$C(m,n) = \sum_i \sum_j A(i,j)B(i-m, j-n) \tag{2.9}$$

Here A and B are corresponding IAs from image A and image B. There are different ways to solve equation 2.9. The most common approaches are direct cross-correlation (DCC) to compute the correlation matrix in the spatial domain or to compute to correlation matrix in the frequency domain using the discrete Fourier transform (DFT). The accuracy of the DCC method is better than the DFT method [73]. However, the disadvantage of DCC is the drastically increased computational power that is needed [4].

Therefore, in this research DFT is used to compute the correlation matrix in the frequency domain. A fast Fourier transform (FFT) was used to compute the DFT. As IAs of identical sizes are used, every particle displacement induced a loss of information. The increasing background noise in the correlation matrix illustrates this problem. The introduction of background noise limits the ability to detect the intensity peak and thus decreases the accuracy [66]. To decrease the amount of background noise, as a rule of thumb, the displacement of the particles should be no more than one quarter of the IA to prevent decorrelation between frames [65].

If multiple passes of the DFT method are used, the results of the first pass can be used as an offset for the IA in the next passes. This minimizes the loss of information due to particle displacement [76].

The data from the correlation matrix determines the start and end point of the velocity vector, which represents the velocity of the fluid. A representation of the above described method is depicted in Figure 2.8. To increase the accuracy of the PIV analysis, the Gaussian peak fit function [71] is used in this research. By using this sub-pixel algorithm, the spatial resolution will be improved. Detailed information regarding this and other sub-pixel algorithm can be found in Raffel et al. [71].
PIVlab uses an iterative multigrid PIV algorithm. Several passes are used and the grid size of the interrogation area can be refined in every subsequent step [66]. As mentioned above, this minimizes the loss due to particle displacement. But furthermore, by using a finer grid size, the final velocity vector map will be of a high spatial resolution.

Due to non-uniform particle motion during an experiment, the intensity peak in the correlation matrix will be broadened and this will lead to deteriorated results. In PIVlab a window deformation technique is implemented to account for the transformation of the IAs. A bi-linear interpolation or spline interpolation is used. The first one is faster, but has a lower accuracy. In this research the spline method was used. More background information regarding the different approaches and algorithms

[3] It is assumed that between two consecutive frames, all particles within an IA have the same motion

[4] The DCC involves $\mathcal{O}(N^4)$ and DFT $\mathcal{O}(2N^2 \log_2 N)$ [74] [75]

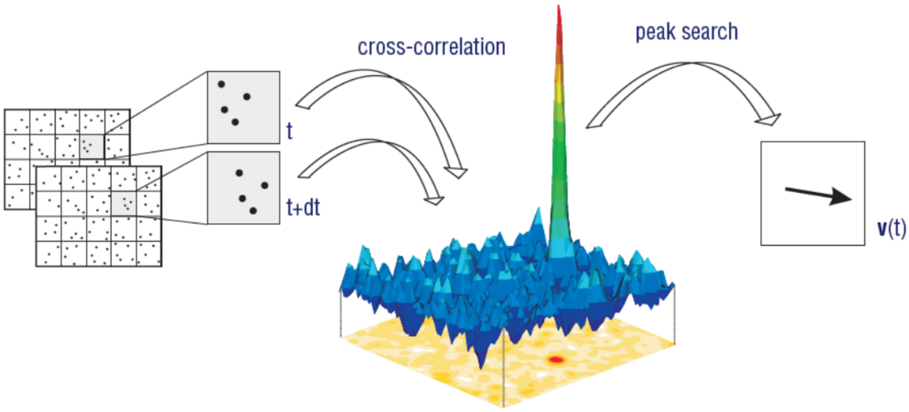


FIGURE 2.8: Cross correlation technique used in PIV, image from Wieneke [77].

can be found in these references: Tropea et al. [59], Raffel et al. [63], Scarano et al [78] and Keane et al. [79].

### Data validation

If there is physical knowledge of the minimum and maximum velocities of the flow, velocity limits can be implemented. In this method velocity thresholds are manually introduced and velocity vectors outside this range are removed from the results.

Another method to determine the velocity threshold is the standard deviation filter. The standard deviation can be calculated from the cross-correlation of two images. Combined with a factor that can be determined by the user, it leads to an upper and lower threshold for the velocity:

$$\begin{cases} u_{lower} = \bar{u} - n \cdot \sigma_u \\ u_{upper} = \bar{u} + n \cdot \sigma_u \end{cases} \tag{2.10}$$

In which $u_{lower}$ and $u_{upper}$ denote the lower and upper velocity limits, $\bar{u}$ the mean velocity and $\sigma_u$ the standard deviation of velocity u. By varying the value of n, the strictness of the filter can be controlled. The user can take the physics of the flow into account and choose an appropriate value of n. Therefore, this filter can also be applied when not all the physical knowledge regarding the flow field is available.

A detection method that automatically adapts to local flow conditions has been designed by Westerweel et al. [80]. The local median filter is a universal outlier detection method that selects velocity data and its $3 \cdot 3$ neighbours. Based on the median of these neighbouring velocity vectors a velocity fluctuation is computed. A threshold is set and when the computed normalized fluctuation exceeds this threshold, the data is regarded as being erroneous. More details and information regarding the threshold values can be found in Westerweel & Scarano [80].

### Data interpolation

Once the filters have been applied and certain velocity vectors have been removed, there is data missing in the vector field. These missing vectors have to be replaced by interpolated data [67]. A boundary value solver is implemented in PIVlab for interpolation of the data.

# Chapter 3

# Characterizing a setup to create and visualize oscillatory flow

## 3.1 Introduction

In this chapter a setup will be designed and characterized that is representative for the flow of CSF in the CNS. In Section 2.1 the flow of CSF is described as an oscillatory flow with a zero mean. The theory from Chapter 2 will be used to design a setup that is able to create an oscillatory flow with a zero mean and that can capture the velocity data using laser PIV. The experimental setup will be described in detail after which the used PIV method is explained. The setup is tested with a straight phantom and several optimizations are implemented to achieve the best results.

In the second part the results of the oscillatory flow in a straight tube are presented and discussed. As the transition to turbulence is of interest, the Reynolds numbers at which the experiments are performed range from 500-2000. The obtained results in this chapter form the foundation for the research in a stenosed pipe, which is conducted in Chapter 4.

## 3.2 Experimental setup

The experimental setup used for the PIV experiments is presented in this section. The setup consists of the flow setup, which creates the oscillatory flow, and the PIV setup to capture the velocity data. Other aspects, such as the flow phantom and the choice of the working fluid, are discussed and the implemented waveform and flow rates are explained. As the high Reynolds numbers lead to an increased entrance length, a special piece of equipment has been designed to decrease the required entrance length.

### 3.2.1 Overview of the setup

The experimental setup that is used is shown in Figure 3.2 and the corresponding schematic overview is depicted in Figure 3.1. The setup consists of two parts; the flow setup and the setup to perform PIV measurements.

#### Flow setup

The flow phantom, which is labeled A in Figure 3.2, is placed in between the two pipes which are labeled B and C. A straw holder is placed in the entrance pipe of the forward flow, to ensure a fully developed flow in the phantom. More information regarding the straw holder and fully developed flow can be found in Section 3.2.5. A reservoir was filled with the working fluid (labeled D in Figure 3.2) and a gear pump (labeled E) was used to fill the system. As soon as the system was filled with the fluid, a valve that is located right after the gear pump was switched to block the flow in this direction. The Vivitro pump, labeled F, (SuperPump, ViVitro labs, Victoria, Canada) was used to create the oscillatory waveform (see Section 3.2.4). In this picture the Sonotec Ultrasound flow sensor (CO.55/260H V2.0, Sonotec, Germany), labeled F, is used, but in earlier experiments the Bronkhorst (Coriolis MX55, Bronkhorst High-Tech B.V., The Netherlands) flow sensor was used. More details regarding the flow sensors can be found in Section 3.5.

### PIV setup

The hardware of a PIV setup has already been described in section 2.3.3; this consists of a laser, a camera and tracer particles. The laser, which is labeled H in Figure 3.2, is a continuous-wave laser (5W DPSS laser, 532 nm; Cohlibri, Light-line, Germany). Optical lenses (Thorlabs, NJ, USA) are placed between the laser and the phantom to form a laser sheet. This thin laser sheet is positioned at the center of the phantom, such that the fluid there is illuminated. Perpendicular to the laser sheet and exactly above the phantom, a high-speed camera was mounted (FASTCAM SA-Z; Photron Inc, West Wycombe, Buckinghamshire, UK). A special 50 mm macro lens (Sigma Benelux, Japan) was mounted to take highly detailed images at a short focusing distance. The camera and lens are mounted to the camera holder which is labeled I in Figure 3.2. The last requirement for the PIV experiments is the addition of suitable tracer particles. Rhodamine coated fluorescent polymethyl methacrylate particles (PMMA) (Rhodamine; Dantec Dynamics A/S, Skovlunde, Denmark) with an average diameter of 10 $\mu$m and a density of 1190 kg/m$^3$ were suspended in the working fluid. More details regarding the tracer particles can be found in Section 3.2.3. To increase the quality of the images and only capture the light emitted by the tracer particles, an optical notch filter was attached under the lens (monochromatic 532 nm; Edmund Optics, Barrington, NJ, USA).

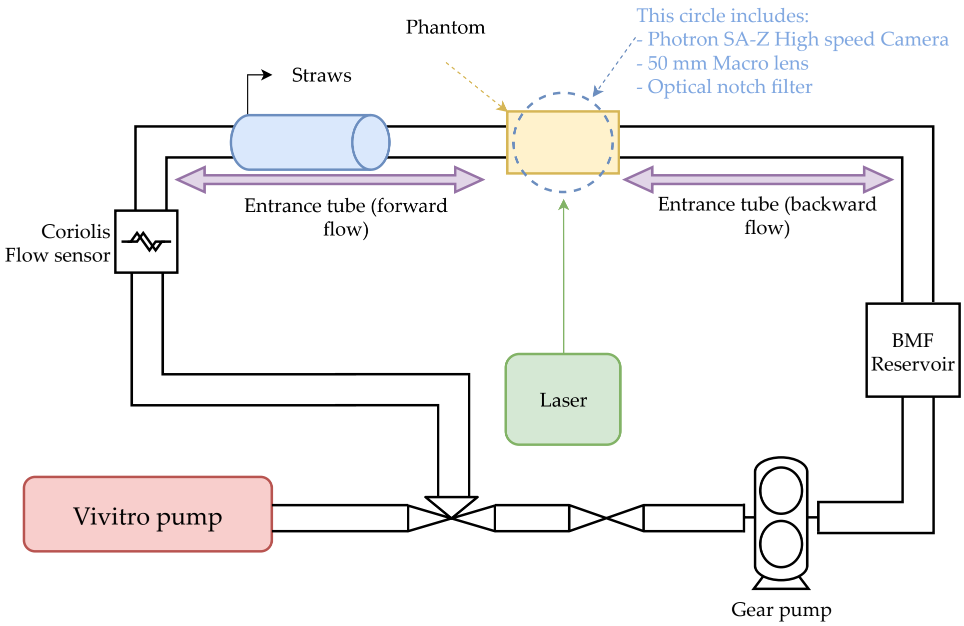


FIGURE 3.1: Schematic of the experimental setup to investigate oscillatory flow.

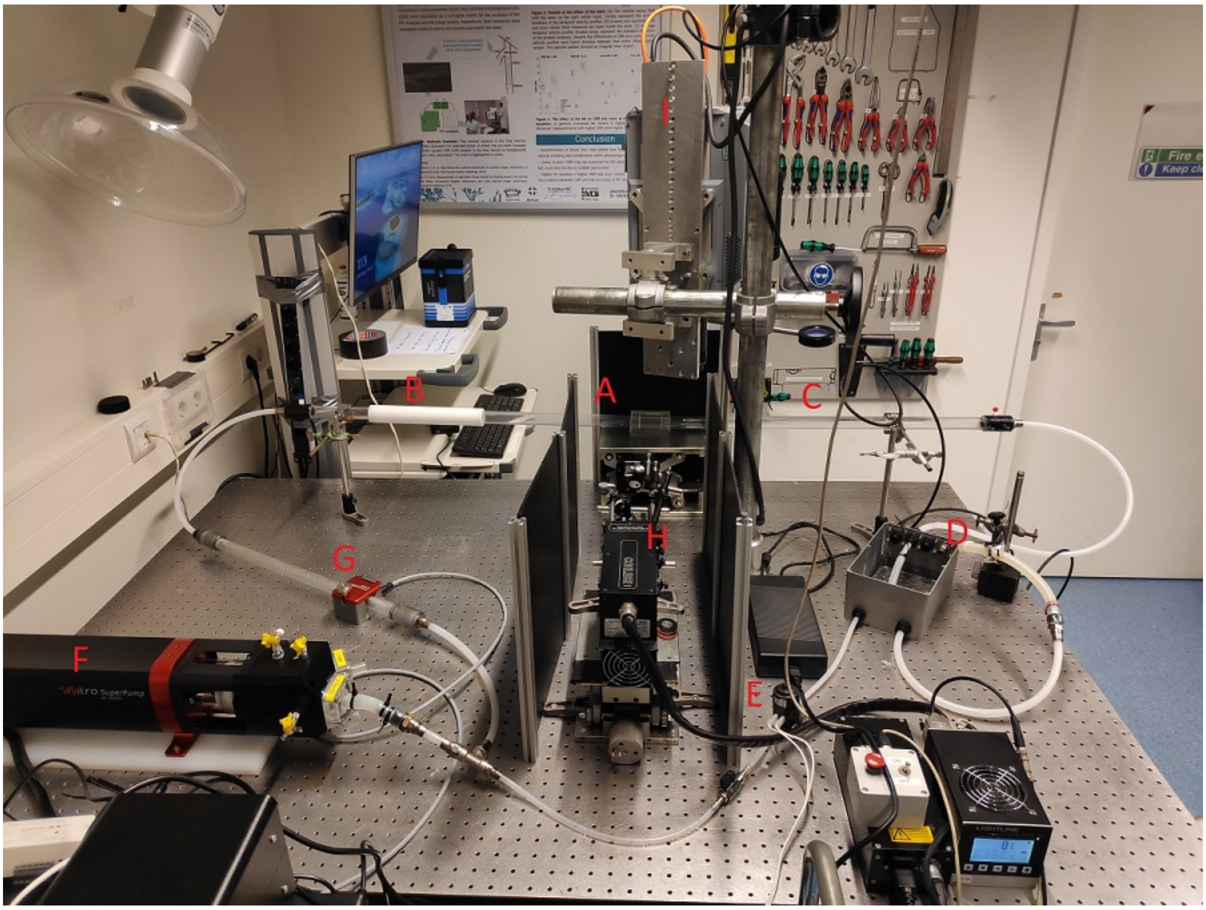


FIGURE 3.2: Overview of the experimental setup to investigate oscillatory flow. The equipment is: A. Flow phantom, B.Entrance pipe including straw holder (forward flow), C. Entrance pipe (backward flow), D. Reservoir, E. Gear pump, F. Vivitro pump, G. Ultrasound flow sensor, H. Continuous wave laser and optics, I. High speed camera, macro lens and optical notch

### 3.2.2 Phantom

The flow phantom used in this part of the research is a straight phantom with an inner diameter of 24.25 mm. A schematic overview of the geometry is shown in Figure 3.3 and the phantom is demonstrated in Figure 3.4. As the goal of this initial research is to build a setup that is able to create and visualize oscillatory flow, a straight phantom is used. An overview of the production method of the phantom is described by Mirgolbabaee [41]. More background information on phantom fabrication methods for PIV experiments is provided by Hoving et al. [81] and Yazdi et al. [82].

### 3.2.3 Working fluid

As described in the theory, the properties of CSF are similar to water. Therefore, the best option for a working fluid would be to use water. However, there are several requirements for the combination of a working fluid, tracer particles and the material of the phantom. The current phantom is made of PDMS (RI = 1.414 [82] [83]), which limits the possibilities for the choice of the working fluid. The refractive index (RI) of the material of the phantom and the working fluid should match, to avoid distortions in the images and limit light refraction on the interface of the PDMS and

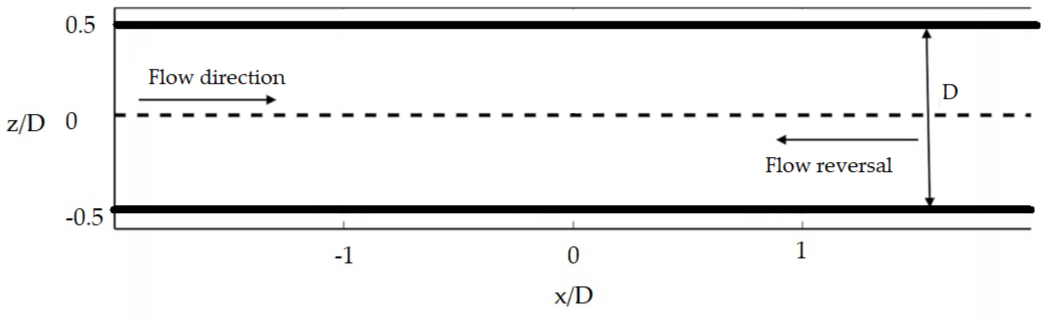


FIGURE 3.3: Schematic geometry of the straight pipe phantom. Image is modified from Jain [8].

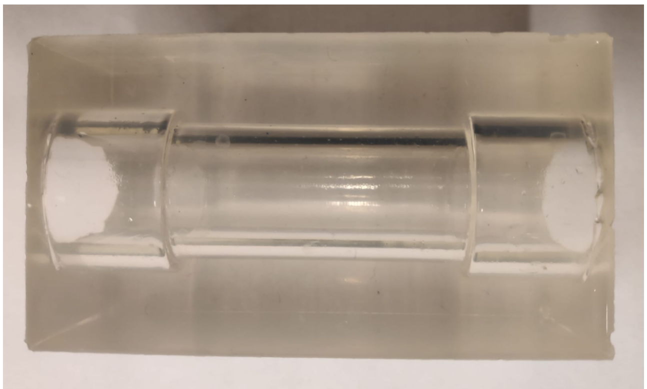

FIGURE 3.4: Picture of the straight pipe phantom.

the working fluid. The RI of PDMS has been matched with blood mimicking fluid (BMF), which is described by Brindise et al. [83]. This mixture of water, glycerol and urea has the fluid properties of blood and the RI matches with PDMS. The exact composition can be found in Table 3.1.

| **Working fluid** | **Component** | **Weight percent [%]** | **Density** $\left[\frac{kg}{m^3}\right]$ | **Viscosity** $[mPa \cdot s]$ | **RI** |
|---|---|---|---|---|---|
| Water | - | - | 1000 | 0.7-1 | 1.33 |
| BMF | Water<br>Glycerol<br>Urea | 44.07<br>34.52<br>21.41 | 1147 | 4.2 | 1.4124 |

TABLE 3.1: Overview of the physical properties of BMF and water.

The choice of BMF as a working fluid has to match with the choice of the tracer particles, as described in Section 2.3.3. The Stokes number is $\approx 2 \cdot 10^{-5}$ in the experiment with the highest velocities and the Archimedes number is $2.8 \cdot 10^{-5}$, therefore it can be concluded that these particles are perfect tracers of the fluid. Other possibilities for the combination of working fluid and phantom material will be explained in the discussion. To ensure that the tracer particles are well distributed in the fluid, the gear pump was turned on after each measurement to circulate the flow. This prevents the particles from oscillating at a specific location, due to the net zero movement of the sine waveform, affecting the quality of the PIV data.

### 3.2.4 Waveform profile

The zero-mean oscillatory flow is achieved by implementing a sine waveform with a frequency of 1 Hz. The maximum Reynolds number in a flow can be determined by:

$$Re_{max} = \frac{\rho v_{max} D}{\mu} \tag{3.1}$$

In order to reach the desired Reynolds numbers, the Vivitro pump is used to generate the sine waveform. The Vivitro pump is a piston pump that represents a simplified model of the human heart. Usually an in- and output is used, and the controllable piston pushes the fluid through the outflow valve into the system. Then the piston moves backwards to its initial position and the inflow valve fills the fluid chamber, which represents the ventricle. In this research the inflow is closed and only a push-pull system is created to obtain the sine waveform.

To make a conversion from the desired Reynolds number to the volumetric flow rate, a method is applied to estimate the peak volumetric flow rates and correlate this to the peak velocities and thus Reynolds numbers. In Figure 3.5 different velocity profiles of the Hagen-Poiseulle and Womersley flow are plotted. The shape of the velocity profile depends heavily on the Womersley number. For lower Womersley numbers the velocity profile is similar to a Hagen-Poiseulle flow and the profile shifts towards a plug-like profile with increasing Womersley numbers. In this research the Wo ≈ 15.9, which leads to a plug-shaped velocity profile.

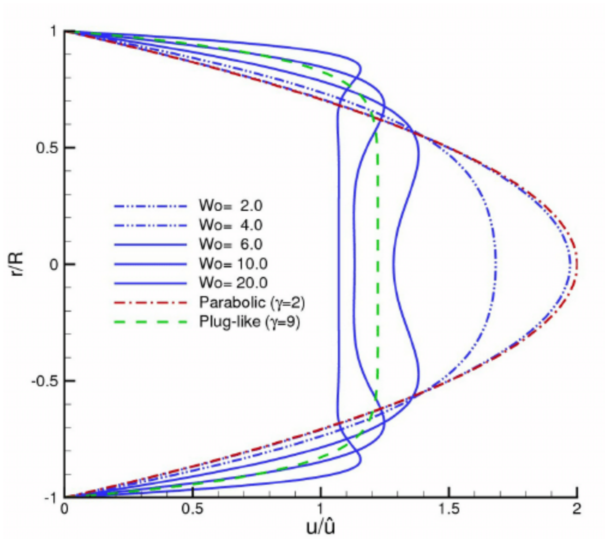


FIGURE 3.5: Steady Hagen-Poiseuille parabolic and plug-like velocity profiles and Womersley flow at five different Womersley numbers. Image from San et al. [84]

There are known relations for the average velocity and the maximum velocity in Poiseuille flow. These relations are unknown for a Womersley flow. Thus as a starting point the relation between the average and maximum velocity in a Poiseuille flow is used, as described in Equation 3.2

$$v_{max} = 2 * v_{avg} \tag{3.2}$$

The volumetric flow rate in a circular tube can be described by:

$$Q = v_{avg} * A = v_{avg} * \pi * \left(\frac{D}{2}\right)^2 \tag{3.3}$$

In which Q is the volumetric flow rate, A is cross sectional area and D is the diameter of the pipe. While inserting the maximum velocity in Equation 3.3 it leads to:

$$Q = \frac{\frac{1}{2} v_{max} \pi D^2}{4} \tag{3.4}$$

By rewriting Equation 3.1 and inserting this in Equation 3.4 an expression for the volumetric rate is found. As the density and the viscosity of the used liquid and the diameter of the tube are constant, the Reynolds number is the only variable.

$$Q = \frac{Re \mu D \pi}{8 \rho} \tag{3.5}$$

In Table 3.2 an overview of the desired Reynolds numbers and corresponding volumetric flow rates is shown.

| $Re_{max}$ | $v_{max}$ [m/s] | $Q_{max}$ [ml/s] |
|---|---|---|
| 500 | 0.0756 | 17.45 |
| 1000 | 0.01511 | 34.90 |
| 1500 | 0.2267 | 52.35 |
| 2000 | 0.3023 | 69.80 |

TABLE 3.2: Overview of $Re_{max}$, velocities and flow rates based on the assumption of Hagen-Poisseule flow.

The implemented sine waveform is displayed in Figure 3.6. The waveform consists of a positive component which accounts for the forward flow and a negative component which accounts for the backward flow. As both components are of equal size, the net flow is zero. The data is analyzed at six equidistant locations along the sine waveform. The temporal locations which are analyzed are displayed by the red dots. These are: $\theta = \frac{\pi}{6}, \frac{\pi}{2}, \frac{5\pi}{6}, \frac{7\pi}{6}, \frac{3\pi}{2}, \frac{11\pi}{6}$.

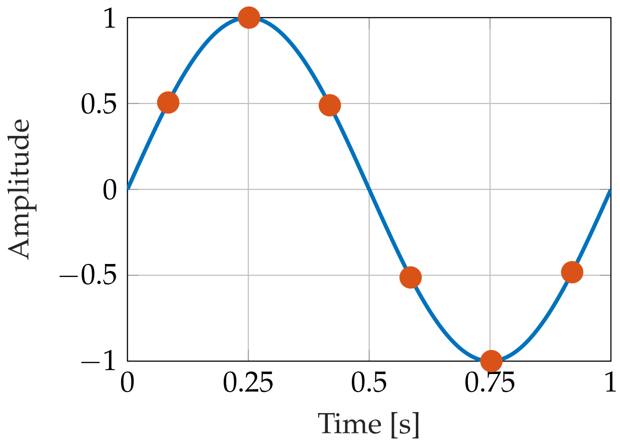


FIGURE 3.6: The implemented waveform including 6 equidistant points along the sinusoidal cycle. The interested temporal locations are: $\theta = \frac{\pi}{6}, \frac{\pi}{2}, \frac{5\pi}{6}, \frac{7\pi}{6}, \frac{3\pi}{2}, \frac{11\pi}{6}$. The forward and backward flow are illustrated by the positive and negative component of the sine. This leads to a purely oscillating flow with zero mean.

**Flow sensors**

There are two types of flow sensors used in the research: A Coriolis flow sensor and an Ultrasound flow sensor. The working principles will be described briefly.

A Coriolis flow sensor is based on a simple principle of the vibration of a tube. When a fluid passes through a Coriolis flow sensor, it will cause a change in the tube vibration due to the momentum of the mass flow. The phase shift of the tube can be measured and the output is proportional to the flow through the sensor.

The Ultrasound flow sensor used in this research is a transient time flow sensor. It measures the time difference of the ultrasonic signal transmitted from the first transducer to the second transducer, which is located on the other side of the pipe. If there is fluid moving in the pipe, the sound moves faster in the direction of the flow and slower in the other direction. By calculating the transient time, the volumetric flow rate can be determined.

It has been verified for the Coriolis flow sensor that it is able to capture pulsatile waveforms [41]. In this research an oscillatory flow is used. The backward flow is not shown by the software from Bronkhorst, as the specified accuracy can not be guaranteed by the Coriolis flow sensor. However, the backward flow data is saved and can be extracted. This is used in the experiments to see if the Bronkhorst flow sensor is able to capture the oscillatory waveform produced by the Vivitro pump. The Ultrasound flow sensor has not been used before, and will be discussed in Section 3.5.

### 3.2.5 Entrance length

As described in Equation 2.3, the entrance length depends on the Reynolds number and the diameter of the phantom. The diameter of the phantom is fixed, however the Reynolds number varies in the experiments. The peak Reynolds number of 2000 leads to a required entrance length of 1.45m to ensure fully developed flow. The length of the entrance pipe for the forward and backward flow is 0.75m, which would not lead to a fully developed flow at the higher Reynolds numbers. Therefore, it would not be possible to perform the experiments in the current setup without modifying the entrance pipes. A modified version of the entrance length is displayed in Equation 2.4. The volumetric flow rate is the only variable that can be changed, as the properties of the fluid are constant. To modify the flow rate, the concept of several smaller diameter pipes in a holder has been introduced. This has been realized by inserting a number of straws in a custom-built holder. By creating several small pipes with a lower volumetric flow rate, a fully developed flow is created within the straws over a short distance. The idea is that this merges just after the straws into a fully developed flow.

| Type | Length [mm] | Diameter [mm] | Number of straws | Shape | $L_e$ [mm] |
|---|---|---|---|---|---|
| **Short** | 120.4 | 2 | 84 | D | 18 |
| **Long** | 200.5 | 3 | 46 | Circular | 32 |

TABLE 3.3: Overview of the specifications of the long and short straws that are used to reduce the required entrance length.

Two different versions have been built, with straws of a different diameter and length. The specifications of both versions are listed in Table 3.3. The increase in number of tubes leads to a decrease in volumetric flow rate per tube. In this calculation it is assumed that all the fluid passes through the straws, while in reality some of the fluid flows in between straws in the straw holder. By using Equations 2.3 and 2.4 the theoretically expected entrance length for the short straws is 18 mm and for the long straws 32mm. As this is shorter than the length of the straws, a fully developed flow is expected within the straws itself. Two different models are built to see if this idea works, compare the results of both versions and to determine which one performs better. The straw holders are shown in Figure 3.7, the left straw holder contains the shorter, black straws and the right model contains the longer, coloured straws. The two straws do not only differ in diameter and length, but also in their shape. The long straws are perfectly circular while the short straws look like two D-shaped profiles attached to each other. These models are clamped in the entrance pipe of the forward flow, as displayed in Figure 3.2. There is no straw holder placed downstream of the flow phantom, to act as a control, thus differences might be noticeable in the results of the forward and backward flow. In the following sections the experiments with the short and long straws holders will simply be denoted by long and short straws to indicate the different setups.

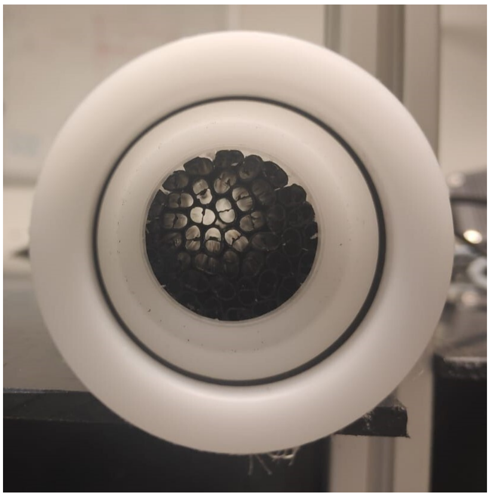

(A) Short straws

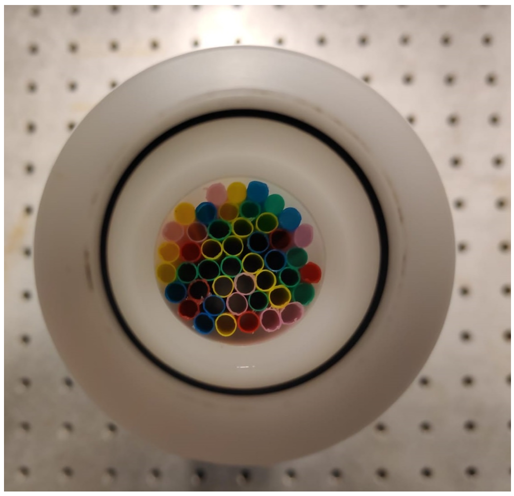

(B) Long straws

FIGURE 3.7: Overview of the straw holders for the short and long straws

## 3.3 Method

### 3.3.1 PIV Method

To analyze the recorded images, PIVlab and MATLAB were used (see section 2.3.4). This software includes all the necessary steps for pre-processing, the PIV analysis and post processing. Afterwards, the obtained data is further analyzed using MATLAB and Tecplot.

#### PIVlab

The camera was positioned such that the whole flow field and both walls of the phantom are visible and to make maximal use of the camera FOV. As this is a straight pipe phantom, a simple mask could be drawn by hand to distinguish the flow field and the walls of the phantom in the entire FOV. In Figure 3.8 the FOV including the mask of one of the measurements is shown. The blue lines denote the mask and the regions outside this mask were discarded from the PIV analysis. The distance between the center of the phantom and the upstream/downstream location is 13mm.

The pre-processing step that was used is the CLAHE filter, which is described in Section 2.3.4. The camera recorded 10 cycles with 2000 fps which leads to 20.000 frames for the PIV analysis. The size of the IAs is selected to have a good spatial resolution and still satisfy the one-quarter rule (see Section 2.3.4). As the velocities differ in each experiment, the IAs were adjusted for some measurements to still satisfy the one-quarter rule. The settings of 2000 fps were based on the expected velocities (Section 3.2.4) and this was converted from m/s to pixels/frame to determine the minimum fps that were needed to accurately capture the particles.

The IAs used in this section of the research are as follows, unless stated otherwise. Four passes are used of 128 $\times$ 128, 64$\times$ 64, 32 $\times$ 32 and 16 $\times$ 16 pixels with an overlap of 50%. The size of the FOV was approximately 27.5 mm $\times$ 27.5 mm, and combined with the final IA size this leads to a spatial resolution of 0.22 mm $\times$ 0.22 mm.

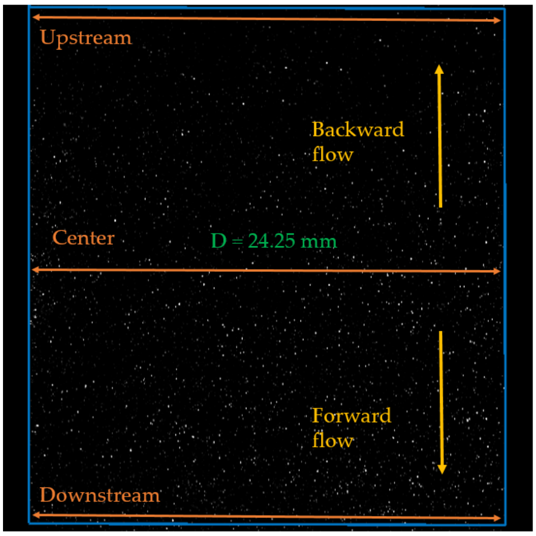


FIGURE 3.8: Recorded frame that is used for the PIV analysis. The mask is displayed by the blue lines and this region is discarded in the PIV analysis.

Once the PIV analysis was finished, the post processing steps as described in Section 2.3.4 were performed. PIVlab has an in built function for two different filters, the standard deviation filter and the local median filter. By applying both filters, the incorrect velocity vectors were detected and removed. The used settings for the filters were n = 7 for the standard deviation filter and $\epsilon$ = 0.1 and $\sigma$ = 2 for the local median filter. The last step that is implemented in PIVlab is the option to replace the removed data with interpolated data, as described in Section 2.3.4.

As the obtained velocity data is based on the recorded images, this leads to velocity in pixels/frame. A conversion from pixels to mm can be made by using the real diameter of the phantom and the FPS can be used to translate the frame to a time interval.

The velocity profiles of these measurements were obtained by averaging the velocity fields over ten cycles. The temporal locations at which the velocity profiles are analyzed correspond to Figure 3.6. The volumetric flow rate based on the PIV data is calculated using the velocity profile and the cross section of the pipe. The v-component of the flow, thus the velocity in the direction of the flow, is used to compute Q = v · A. The cross-sectional area in this equation can be determined as the radius of the phantom is known. The volumetric flow rate is determined over the different cross sections and then averaged to obtain the volumetric flow rate in the phantom. By averaging over ten cycles, the volumetric flow rates from the flow sensor and the PIV data were obtained. By applying an error bar of two times the standard deviation, 95% of the data is included in this region. This method is used for both the PIV data and the flow sensor results. To compare the volumetric flow profiles from the flow sensor and the PIV data, a root mean square analysis is performed by applying the following formula:

$$\text{RMSE} = \sqrt{\frac{\sum_{i=1}^{N} (x_1 - x_2)^2}{N}} \tag{3.6}$$

Here $x_1$ and $x_2$ denote the data of the different data sets and N is the total number of values. The unit of the RMSE is the same as the investigated data, thus in this case ml/s. To compare the different measurements, an absolute and relative error has been determined. The absolute error has been scaled by the peak volumetric flow rate to obtain the relative RMSE.

### 3.3.2 Analysis methods

**Definition of Reynolds number**

The computation of the Reynolds number is complicated in pulsatile flows, as there is no constant velocity value. Therefore, the Reynolds number changes along the location of the implemented sine waveform. Therefore, different definitions of the Reynolds number are used which are introduced below.

1. $Re_{max}$: The Reynolds number based on the maximum velocity obtained by the velocity profile in the center of the phantom.
2. $Re_{peak}$: The Reynolds based on the maximum velocity of the sinusoidal profile. This is the theoretical inlet velocity.
3. $Re_{avg}$: The average Reynolds number calculated by using $u_c$, the half-cycle averaged centerline velocity.

These definitions will be used in the next chapters to refer to certain measurements.

**Deformation of phantom**

To determine the deformation of the walls of the phantom, the following equation is used.

$$\text{Deformation} = \frac{Y_{max} - Y_{min}}{Y_{min}} \tag{3.7}$$

In which $Y_{min}$ denotes the minimum diameter in pixels of the phantom and $Y_{max}$ the maximum diameter in pixels. The diameter is determined by analyzing the raw PIV images and calculating the difference in the location of the phantom walls. The deformation is presented in pixels and in the percentage of the diameter of the phantom.

## 3.4 Results

The results are divided into several sections. The first experiments were performed, after which it became clear that modifications to the setup were favorable. The initial results, adjustments to the setup and final results of the experiments are explained in the upcoming sections.

The flow rates as described in Table 3.2 were implemented in the experiments to obtain the desired Reynolds numbers. An overview of the Reynolds numbers derived from the experimental data is given in Table 3.4. Figure 3.9a depicts the velocity profile of the experiment that was performed at the lowest flow rate. The data of the highest flow rate is presented in Figure 3.9b. The volumetric flow rates based on the PIV data and the Bronkhorst Coriolis flow sensor are shown in Figure 3.10. To compare the obtained results, a perfect sine waveform is plotted in black.

| $Q_{max}$ [ml/s] | $v_{max}$ [m/s] | $Re_{max}$ | $v_{peak}$ | $Re_{peak}$ | $v_c$ | $Re_{avg}$ |
|---|---|---|---|---|---|---|
| 17.5 | 0.051 | 350 | 0.039 | 250 | 0.029 | 200 |
| 35 | 0.097 | 650 | 0.078 | 500 | 0.058 | 400 |
| 52 | 0.142 | 950 | 0.125 | 750 | 0.081 | 550 |
| 70 | - | - | - | - | - | - |

TABLE 3.4: Overview of flow rates, velocities and different Reynolds numbers from the experiments. $Re_{max}$ is based on the maximum velocity obtained by the velocity profile, $Re_{peak}$ is based on the theoretical inlet velocity of the sine waveform and $Re_{avg}$ is the average Reynolds number based on the half-cycle averaged centerline velocity.

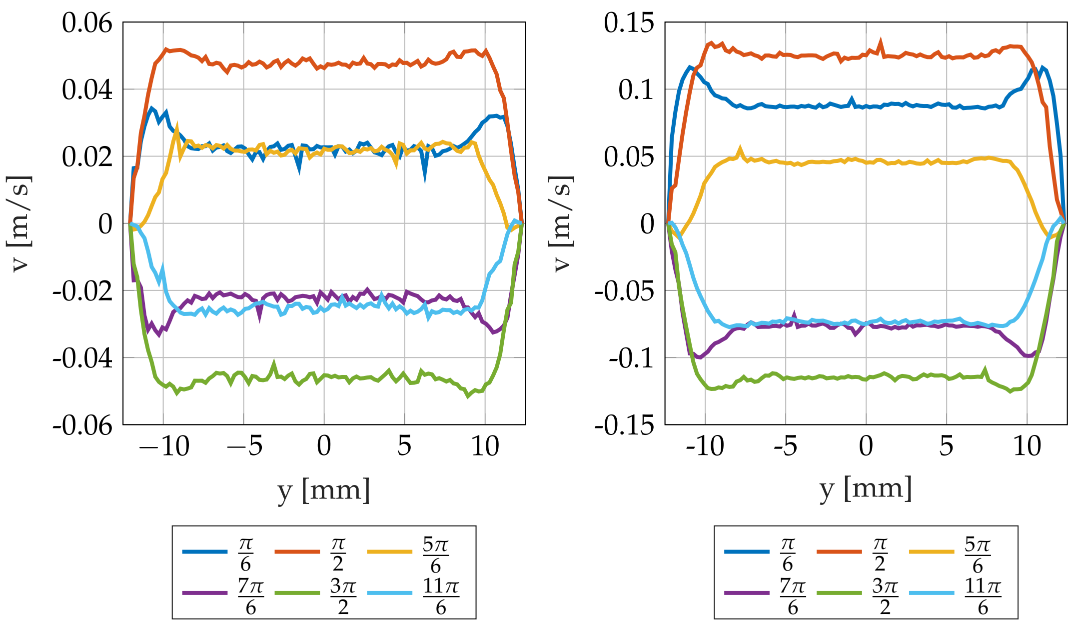


(A) $Re_{max} \approx 350$

(B) $Re_{max} \approx 950$

FIGURE 3.9: Velocity profile in the center of the ROI at six points along the sine wave. The v-component is plotted for the lowest and highest $Re_{max}$.

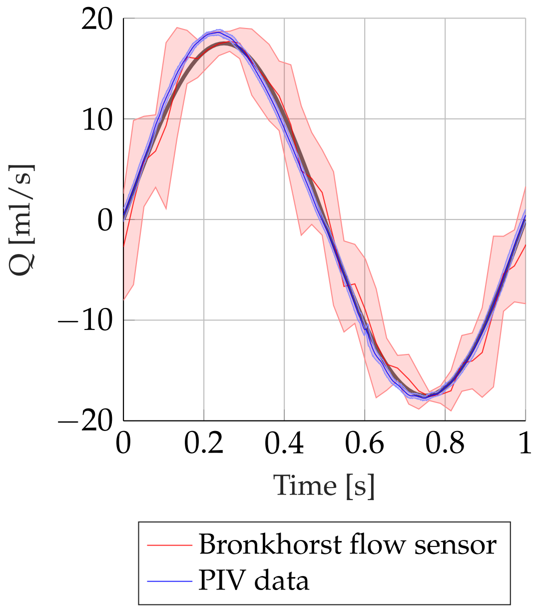


(A) $Re_{max} \approx 350$

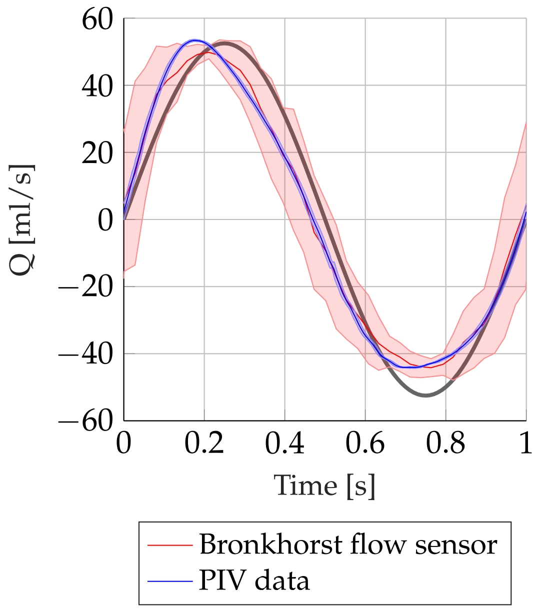


(B) $Re_{max} \approx 950$

FIGURE 3.10: Comparison of the volumetric profile obtained by the flow sensor and the PIV data. A sine waveform is displayed in grey.

The results depicted in Figure 3.9 and Figure 3.10 show that the Vivitro pump is able to create an oscillating flow, that the Bronkhorst Coriolis flow sensor is able to measure a bidirectional flow and that it is feasible to extract the velocity and volumetric profiles from the PIV data.

The actual Reynolds numbers based on the PIV data are considerably lower than estimated in Section 3.2.4. The assumption of $v_{max} = 2 \times v_{avg}$ is no longer valid as the peak velocity is lower, which is displayed in Figure 3.9. The data of the flow sensor and PIV data match very well and seem to be accurate. Especially for the lower volumetric flow rate (Figure 3.10a) the PIV data follows the theoretical sine waveform accurately. However, in Figure 3.10b there is a bigger deviation between the obtained volumetric flow rate from the PIV data and flow sensor and the sine waveform. The deviation between the volumetric profiles is quantified in Table 3.5. During the measurement at 70 ml/s the Vivitro pump was not able to create the waveform at the desired flow rate, the results of this experiment are presented in Appendix A. There was a large pressure build-up in the system, which distorted the wave form. The maximum Reynolds number that is obtained during the experiments is far from the expected transitional regime (as described in Section 2.2). Therefore, the setup had to be adjusted such that it can handle higher flow rates, create a better sine waveform and obtain higher Reynolds numbers.

| $\mathbf{Re}_{max}$ | **RMS error between the PIV and flow sensor** | | **RMS error between PIV and sine waveform** | |
|---|---|---|---|---|
| | Absolute | Relative | Absolute | Relative |
| 350 | 1.44 [ml/s] | 8.2% | 0.79 [ml/s] | 4.5% |
| 650 | 5.71 [ml/s] | 16.3% | 3.00 [ml/s] | 8.6% |
| 950 | 4.97 [ml/s] | 9.6% | 7.87 [ml/s] | 15.1% |

TABLE 3.5: Overview of the RMS error between volumetric flow profiles. The relative error is determined by comparing the absolute error to the peak volumetric flow rate.

## 3.5 Flow sensors

The internal tube diameter of the Bronkhorst MX55 Coriolis flow sensor is 4mm, which is a significant reduction compared to the tubing of 12mm and the phantom of 24mm. This leads to a resistance in the flow, especially at higher volumetric flow rates hindering the Vivitro pump to reach the set amplitudes. As shown in the Figures in Section 3.4 and Appendix A, this leads to a distortion of the sine waveform. To overcome this problem, another type of flow sensor has been tested. By using a Ultrasound flow sensor, no reduction in tube diameter is necessary as it is clamped around a tube. The Sonotec CO.55/260H V2.0 flow sensor has a calibration tube with an outer diameter of 25.2 mm and inner diameter of 20.4 mm. As a result, the flow sensor will no longer be the limiting factor in terms of tube diameter.
The Coriolis sensor has been verified that it is able to capture the oscillatory flow profile. Therefore, a comparison between the Ultrasound and Coriolis flow sensor is needed to measure its performance and see if it is a good replacement for the Coriolis sensor. The Coriolis sensor is considered the gold standard. The technical specifications of the Ultrasound and Coriolis flow sensor are displayed in Table 3.6 [85].

| **Sensor** | **Upper range value** | **Accuracy** | | **Sample time** |
|---|---|---|---|---|
| **CO.55/260H V2.0** | 70.000 ml/min | 0 … 7.000 ml/min: ± 140 ml/min | 7.000 ... 70.000 ml/min: ± 2% | up to 10 ms |
| **Coriolis MX55** | 6.000 ml/min | 2% of reading | | 35ms |

TABLE 3.6: Specifications of the Sonotec CO.55/260H V2.0 and Bronkhorst Coriolis MX55 flow sensors. The accuracy for the Sonotec sensor is for water, adjusted at 23 °C ± 2 °C and 1 bar on specified tube

To test the performance of the Ultrasound flow sensor, a simple setup has been built. A gear pump is used to create a circulating flow of water and both the Coriolis and Ultrasound flow sensor are connected in series to measure the volumetric flow rate. A sketch and picture of this setup are shown in Figure 3.11.

As the Ultrasound flow sensor has not been used before, the optimal settings to capture the volumetric flow rate are unknown. As displayed in Table 3.6, this flow sensor is suitable for very large flow rates. This introduces an inaccuracy which is relatively large at lower flow rates. To increase the accuracy of the measurements, the amount of flow samples which are used for the flow averaging can be increased. This leads to a high accuracy for a steady flow, but it cannot respond adequately to fluctuations in the oscillatory flow. Therefore a tradeoff has to be made between accuracy and a fast response time.

In Figure 3.12 the results of the test with a continuous flow are presented. The Coriolis flow sensor shows consistent flow rates and reacts swiftly to the fluctuations in the flow. These fluctuations were created by adjusting the current of the gear pump and thus changing the velocity of the fluid. When using a high number of data points to average the flow rate, the Ultrasound flow sensor is able to accurately capture the flow, but the response time is very high (Figure 3.12a). Since an oscillating flow is used in the study, it is important that the sensor can respond well to fluctuations. Therefore, a lower number of data points to average over had been chosen. By selecting averaging over 32 data points, the flow sensor is able to perform reasonably well compared to the reference of the Coriolis flow sensor.

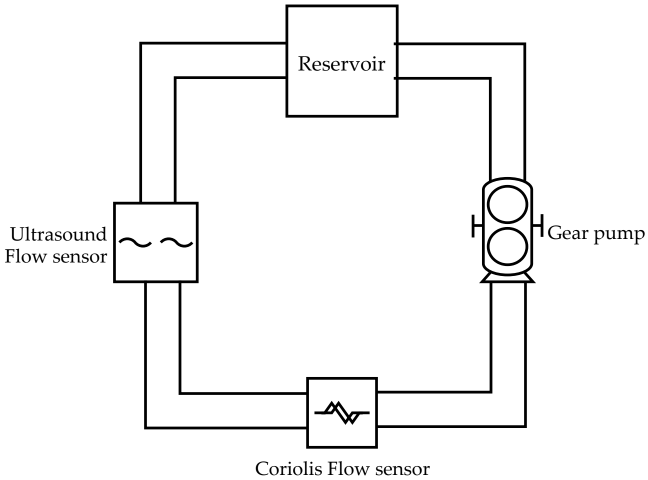


(A) Schematic of the experimental setup to investigate the flow sensors

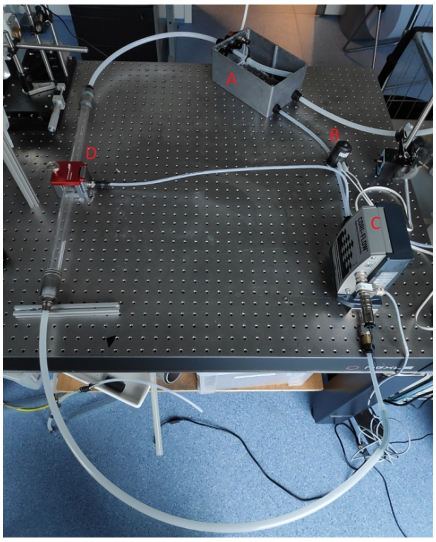


(B) Overview of the experimental setup to investigate the flow sensors. A) Reservoir, B) Gear pump C) Coriolis flow sensor, D) Ultrasound flow sensor.

FIGURE 3.11: Overview of the setup to test the Bronkhorst Coriolis and Sonotec Ultrasound flow sensors.

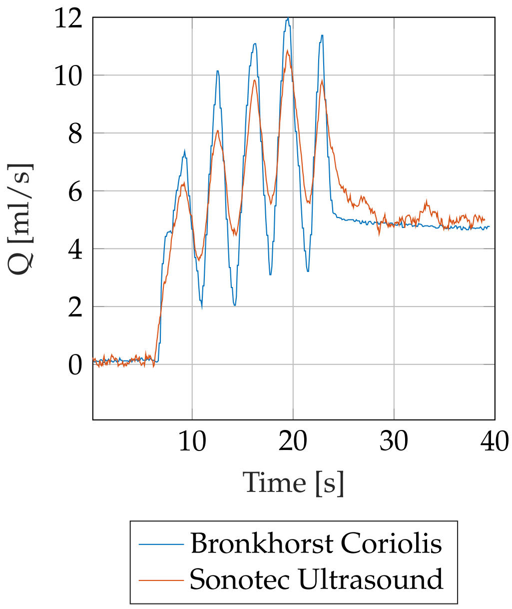


(A) Averaging over 125 samples

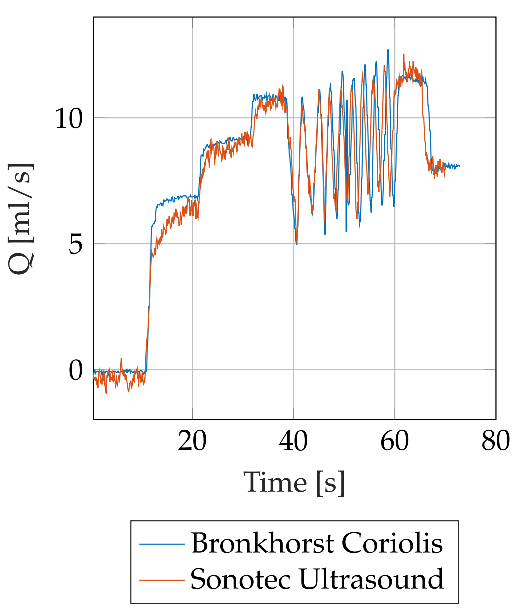


(B) Averaging over 32 samples

FIGURE 3.12: Comparison of the Coriolis and Ultrasound flow sensor. The flow is generated by the gear pump.

## 3.6 Results of the updated setup

The only adjustment to the setup used in Section 3.4, is the use of the Sonotec Ultrasound flow sensor instead of the Bronkhorst Coriolis flow sensor. This should lead to a lower resistance and thus a better sine waveform. The following sections provide detailed information about the long and short straws, the sine waveform, and the Reynolds numbers during these experiments.

The experiments were performed with the long and the short straws, to see if any differences in the velocity field could be noticed. The velocity profiles of the v-component including the error bars are shown in Figure 3.13 and 3.14. The Womersley number in the phantom, and thus the location of the experiments, is 15.9. This leads to a plug-shaped profile, as discussed in Section 3.2.4. The straw holders were introduced to decrease the required entrance length, but as the diameter changes, the value of the Womersley number changes. The value of the Womersley number for the short and long straws is 1.3 and 2.0 respectively, which indicates a parabolic velocity profile. After the straw holders the Womersley number will increase and the profile will be plug shaped. The results in Figure 3.13 and 3.14 show that the velocity profile of the long straws is smoother and the error bars are significantly lower.

The straws only affect the forward phase of the flow, but there is no noticeable difference between the forward and backward flow. An explanation may be that the backward flow is already able to fully develop without the added straw holder as the Reynolds number is not too high. Based on the theory the length of the entrance pipe would not suffice above Reynolds numbers of 1000, while in these measurements the $Re_{max} \approx 1300$.

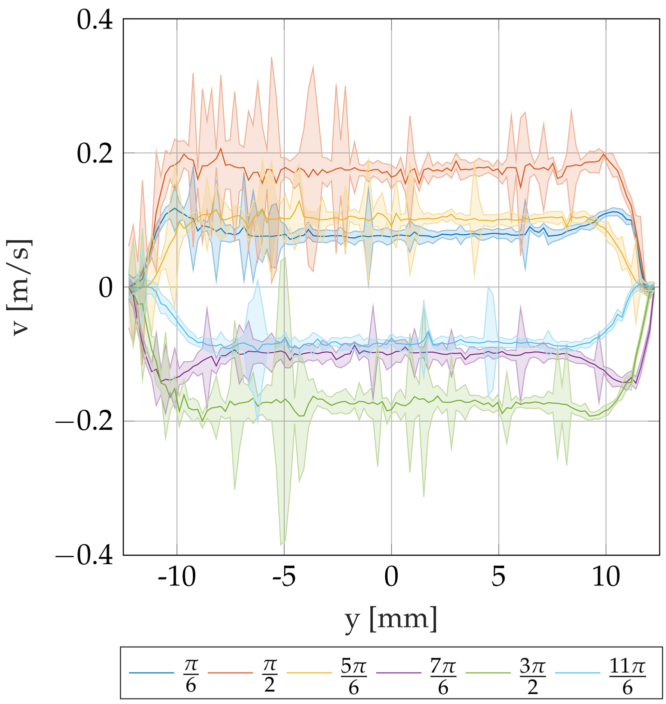


FIGURE 3.13: Velocity profiles in the center of the ROI depicted with their errors bars. Setup with the short straws and $Re_{max} = 1300$

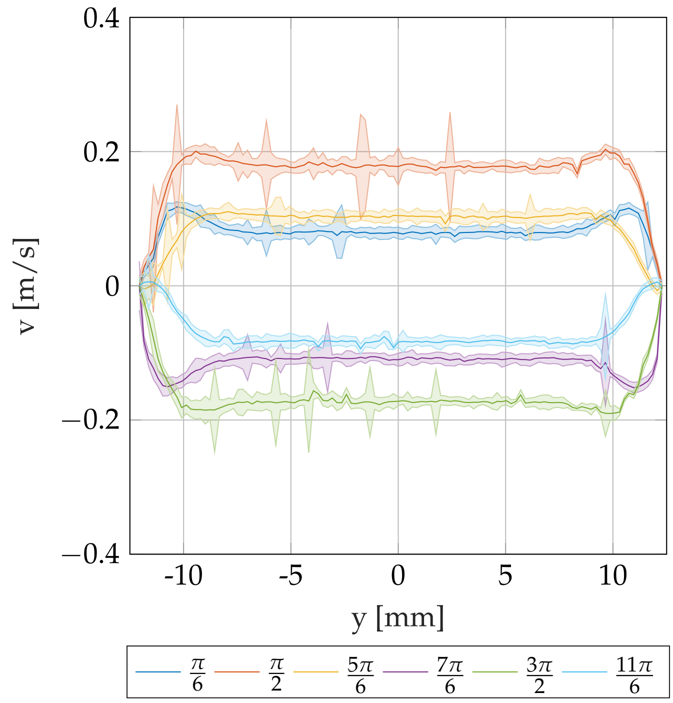


FIGURE 3.14: Velocity profiles in the center of the ROI depicted with their errors bars. Setup with the long straws and $Re_{max}$ = 1350.

When the velocity profile for different locations in the phantom are observed, clear differences between the center, upstream and downstream are visible. The distance between the center and upstream/downstream location is 13mm. The velocity profiles at peak forward flow rate of the long straw setup are shown in Figure 3.16, the blue line represents the velocity profile in the center, the red line the velocity profile downstream and the yellow line the upstream location. The upstream locations shows a large deviation from the smooth velocity profile, but the Womersley velocity profile is still visible. In the center the velocity profile is smooth in the long straw case, and further downstream, thus further away from the straw holders, it is even smoother. There is however a big difference between the center and the upstream location, thus closer to the straw holders. Here the velocity profile is not smooth yet but irregular.

The velocity profile of the short straw setup is demonstrated in Figure 3.15, the blue line represents the velocity profile in the center, the red line the velocity profile downstream and the yellow line the upstream location. A similar pattern to the long straw setup is visible, the velocity profile in the center and downstream overlap at most spatial locations, but the yellow velocity profile differs significantly. The shape of the Womersley profile is still visible, but upstream of the center there are large deviations and many peaks in the velocity profile. The velocity profile downstream of the center is relatively smooth and comparable to the velocity profile in the center.

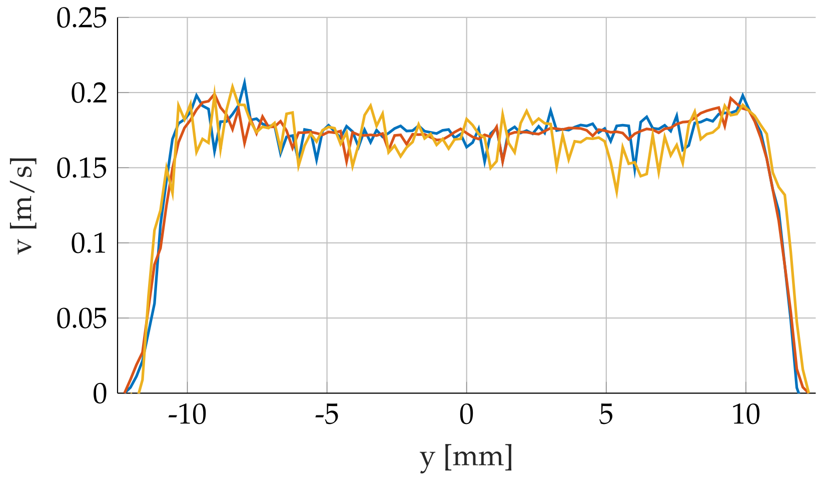


FIGURE 3.15: Velocity profiles in the center, up- and downstream. Setup with the short straws and $Re_{max}$ = 1300 during peak forward phase, $\frac{\pi}{2}$. The blue line represents the center of the ROI, the red line the location downstream and the yellow line the upstream location.

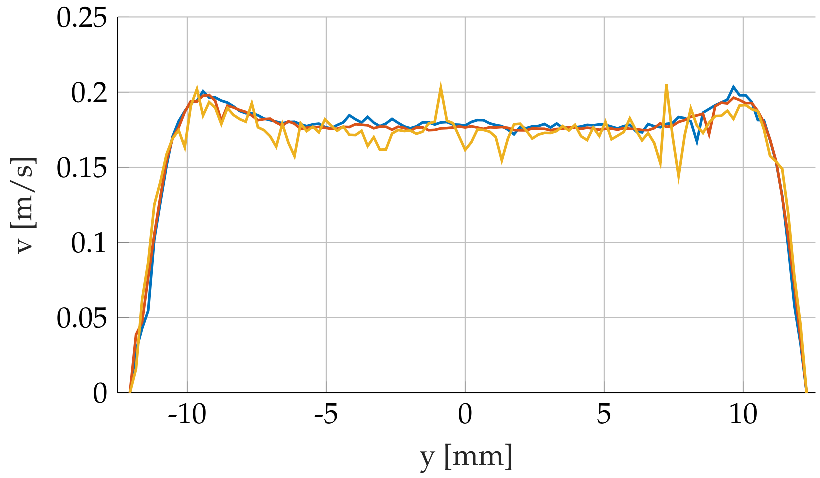


FIGURE 3.16: Velocity profiles in the center, up- and downstream. Setup with the long straws and $Re_{max}$ = 1300 during peak forward phase, $\frac{\pi}{2}$. The blue line represents the center of the ROI, the red line the location downstream and the yellow line the upstream location.

The volumetric velocity profiles are presented in Figure 3.17. There is no clear difference between the volumetric profile of the short or long straw setup. The shape of the sine waveform will be discussed in the next section.

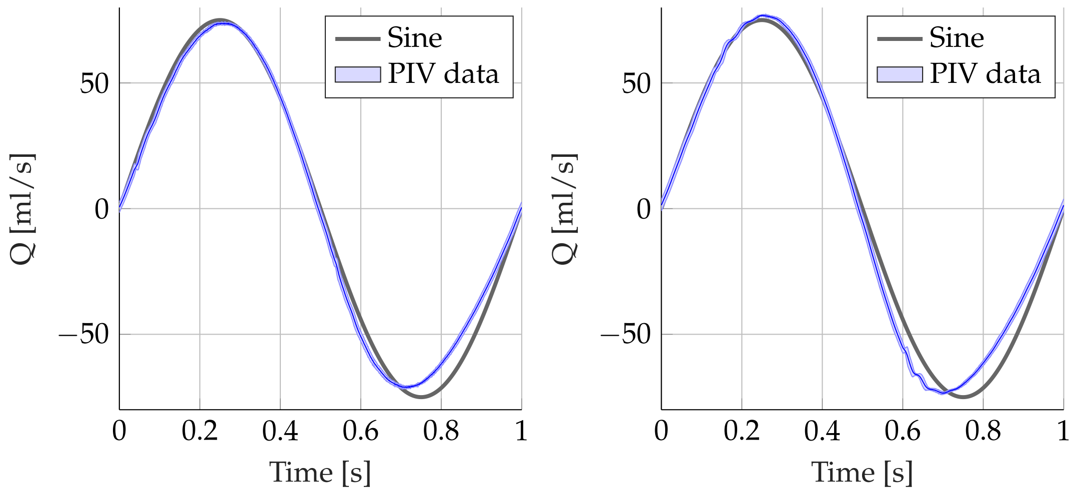


(A) $Re_{max}$ = 1300 short (B) $Re_{max}$ = 1350 long

FIGURE 3.17: Comparison of the volumetric profile obtained by the PIV data including error bars of two standard deviation and a perfect sine waveform.

### Highest Reynolds number

During the first experiment it was not feasible to reach higher flow rates than 50 mL/s. The setup could not handle these flow rates and the pressure build was too high, which led to a distortion of the sine waveform. As displayed in Figure 3.17, in the updated setup it was feasible to measure peak volumetric flow rates of 75 mL/s, while the sine waveform still retained its shape. An overview of the data from the experiments is presented in Table 3.7. The experiments were performed at increasing volumetric rate, to test the ability of the setup and investigate the flow phenomena at different Reynolds numbers.

| $Q_{max}$ [ml/s] | Straws | $v_{max}$ [m/s] | $Re_{max}$ | $v_{peak}$ | $Re_{peak}$ | $v_c$ | $Re_{avg}$ |
|---|---|---|---|---|---|---|---|
| 35 | Long | 0.098 | 650 | 0.076 | 500 | 0.055 | 350 |
| 75 | Long | 0.205 | 1350 | 0.160 | 1050 | 0.115 | 750 |
| 73 | Short | 0.20 | 1300 | 0.158 | 1050 | 0.112 | 750 |
| 125 | Short | 0.33 | 2200 | 0.27 | 1800 | 0.188 | 1250 |

TABLE 3.7: Overview of the flow properties of the experiments with the updated setup. $Re_{max}$ is based on the maximum velocity obtained by the velocity profile, $Re_{peak}$ is based on the theoretical inlet velocity and $Re_{avg}$ is the average Reynolds number based on the half-cycle averaged centerline velocity.

The velocity profile of the measurement with the highest Reynolds number is shown in Figure 3.18. These results actually correspond to a flow with a $Re_{max}$ of approximately 2200. The volumetric flow rate is displayed in Figure 3.19, in which the peak value is 125 ml/s. The sine waveform shows a bigger deviation of a perfect sine than at the lower flow rates displayed in Figure 3.17, but the deviation has decreased compared to the first experiments. To quantify the waveform, the RMSE has been calculated, of which the results are shown in Table 3.8. As the relative error is significantly lower than during the measurements with the Coriolis flow sensor, the replacement of the flow sensor seemed to lower the resistance and improve the performance. Now it is feasible to go up to a $Re_{max}$ of 2200, while during the first experiments the highest obtained $Re_{max}$ was 950.

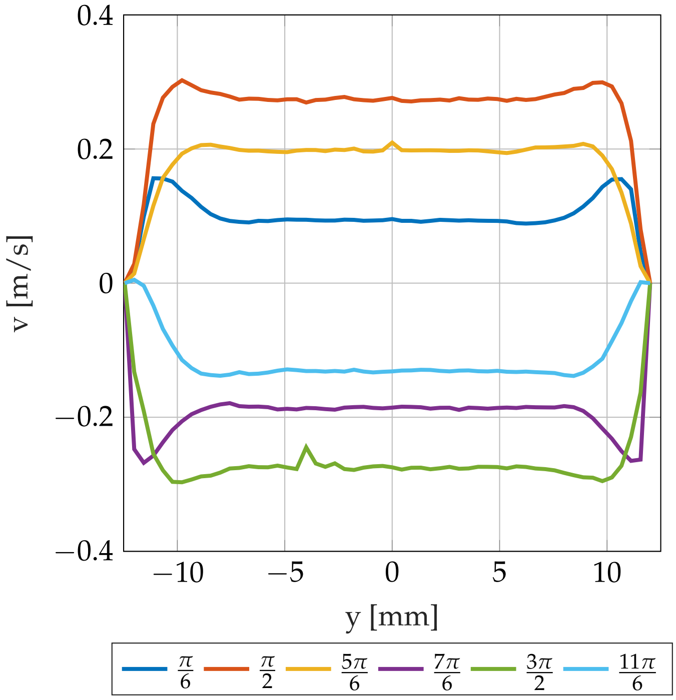


FIGURE 3.18: Velocity profile in the center of the ROI at six points along the sine wave at $Re_{max}$ = 2200 with short straws

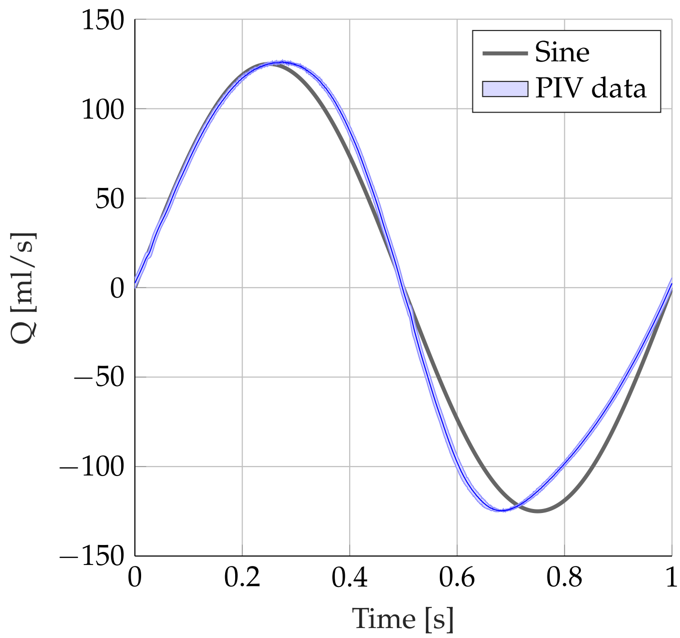


FIGURE 3.19: Volumetric profile of $Re_{max}$ = 2200 with short straws

| **Re$_{max}$** | **Flow sensor** | **Straws** | **RMS error between PIV and sine waveform** | |
|---|---|---|---|---|
| | | | Absolute | Relative |
| 350 | Coriolis | Short | 0.79 [ml/s] | 4.5% |
| 650 | Coriolis | Short | 3.00 [ml/s] | 8.6% |
| 650 | Ultrasound | Long | 1.61 [ml/s] | 4.6% |
| 950 | Coriolis | Short | 7.87 [ml/s] | 15.1% |
| 1300 | Ultrasound | Short | 4.64 [ml/s] | 6.6% |
| 1350 | Ultrasound | Long | 5.03 [ml/s] | 7.2% |
| 2200 | Ultrasound | Short | 12.52 [ml/s] | 10.0% |

TABLE 3.8: RMS error between the obtained PIV volumetric flow rate and the sine waveform. The results of the experiments with the Coriolis flow sensor are included to compare the results.

During the measurements it was observed that the phantom deformed due to the flow. Especially at the higher Reynolds numbers, the deformation was clearly visible by eye. An example of the deformation of the phantom walls is demonstrated in Figure 3.20. The red lines show the phantom walls at the moment of minimum deformation and the blue lines during maximum deformation. The deformation of the phantom at the different Reynolds numbers has been quantified by analyzing the raw data as explained in Equation 3.7 and the results are presented in Table 3.9. The snapshot in Figure 3.20 is at Re$_{max}$ = 2200, the experiment at which the deformation of the phantom walls was at its maximum, as the volumetric flow rates were the highest. The exact deformation differs during every cycle, thus it can even exceed the values shown in Table 3.9 during some cycles. There was no noticeable difference between the long and short straw setup, thus there is no distinction made between these setups in Table 3.9. Both sides of the phantom seemed to expand equally, however it would require an additional method to investigate it more thoroughly and verify this result.

| **Re$_{max}$** | **Original diameter in px** | **Deformation in px** | **Deformation in %** |
|---|---|---|---|
| 650 | 872 | 12 | 1.4% |
| 1350 | 872 | 30 | 3.4% |
| 2200 | 872 | 52 | 6.0% |

TABLE 3.9: The deformation of the phantom during the experiments.

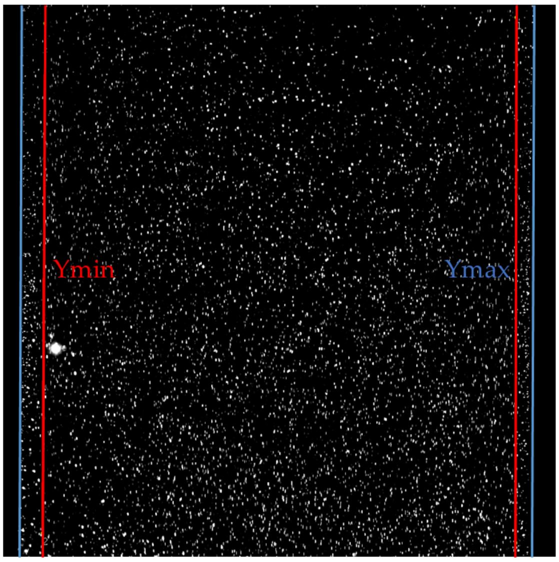


FIGURE 3.20: Deformation of the phantom walls indicated by the minimum and maximum deformation of the phantom walls at $Re_{max}$ = 2200. The red lines represent the walls of the phantom at the minimum deformation and the blue lines at the maximum deformation.

### Centerline velocities

The centerline velocities of the measurements are shown in Figures 3.21 and 3.22. Several values for $Re_{max}$ are shown, to investigate the influence of the Reynolds number and see if there are signs of turbulence at the different stages.

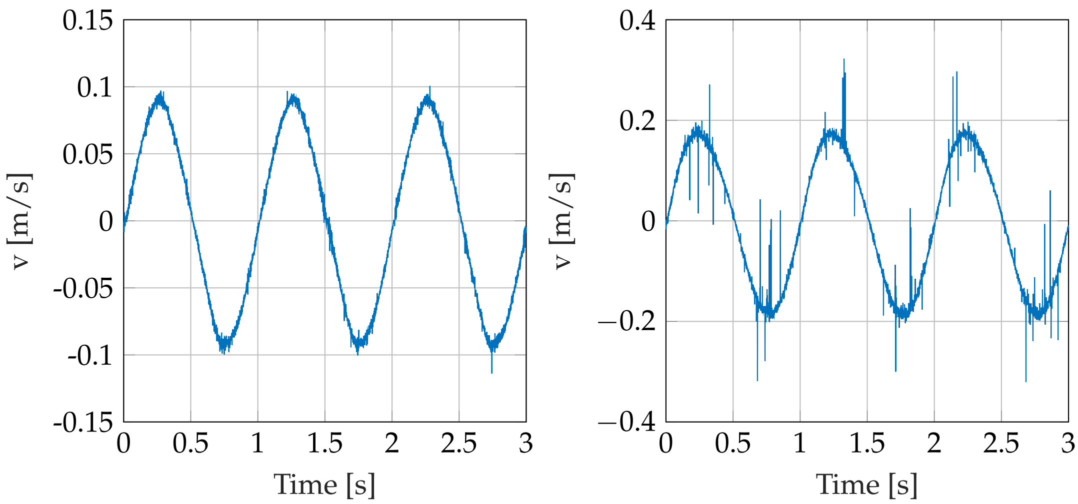


(A) Velocity in the center of the phantom during the first 3 cycles. Re ≈ 650 and long straws

(B) Velocity in the center of the phantom during the first 3 cycles. Re ≈ 1300 and short straws

FIGURE 3.21: Centerline velocity of the experiments at $Re_{max}$ = 650 and $Re_{max}$ = 1300

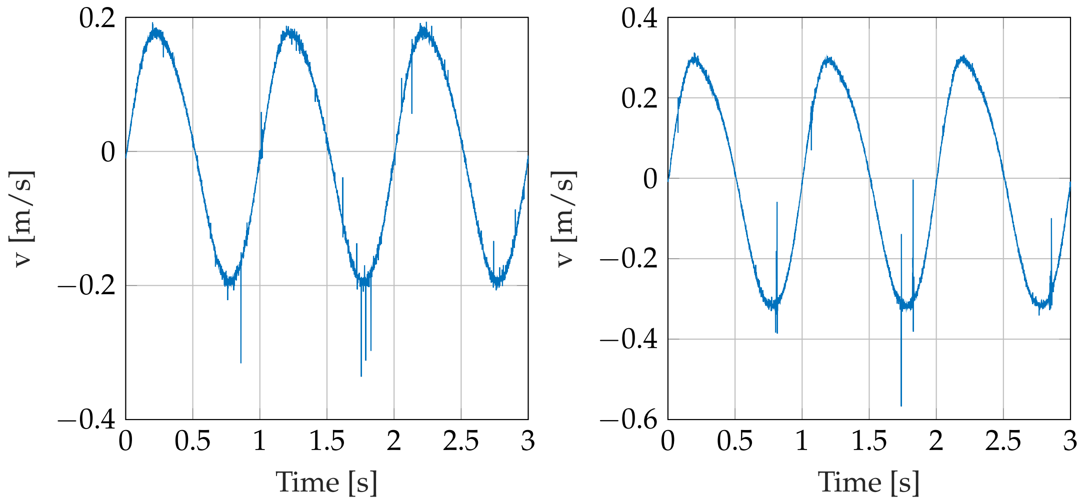


(A) Velocity in the center of the phantom during the first 3 cycles. Re $\approx$ 1350 and long straws

(B) Velocity in the center of the phantom during the first 3 cycles. $Re_{max}$ = 2200 and short straws

FIGURE 3.22: Centerline velocity of the experiments at $Re_{max}$ = 1350 and $Re_{max}$ = 2200

There are no clear differences between the different Reynolds numbers and the different straw setups. There are very small perturbations in the peak, but no clear signs of weak turbulence are visible, when compared to the results of Hino et al. [45]. There is no increased velocity or distorted profile in the deceleration phase, thus the conditionally turbulent phase, as discussed in Section 2.2.3, is not relevant here. The Reynolds numbers seem to be too low, or the amount of distortions in either the geometry or waveform too insignificant, that a transition to turbulence is not triggered yet. These centerline velocities can be compared to the results obtained in Chapter 4, to investigate the influence of a distortion of the geometry on the centerline velocities and a possible transition.

### Flow sensor

A comparison of the volumetric flow rate from the Sonotec Ultrasound flow sensor and the PIV data is demonstrated in Figure 3.23. The peak volumetric of the PIV data is approximately twice as high and is not consistent with the measured flow sensor data. During the first experiment (see Section 3.4) the PIV data and the flow sensor data from the Coriolis sensor were consistent and the flow sensor was able to accurately capture the sine waveform.

As the results from the PIV analysis and the Ultrasound flow sensor did not match, a second experiment was conducted to verify the performance of the Ultrasound flow sensor. During the first experiment when the performance of the Ultrasound en Coriolis flow sensors were compared, the flow was created by a gear pump. This time the Vivitro pump was used to create an oscillatory waveform, to create the same flow conditions as during the PIV experiments. The results are shown in Figure 3.24a, in which the Ultrasound flow sensor data is averaged over 32 data points. When using large volumetric rates, the flow sensor is not able to respond quickly enough to fluctuations in the flow. By adjusting the settings and averaging over 8 data points, the flow sensor responds quickly to fluctuations in the flow. The results of the experiment with the adjusted settings is shown in Figure 3.24b. The Ultrasound flow sensor is able to capture the oscillatory flow, but

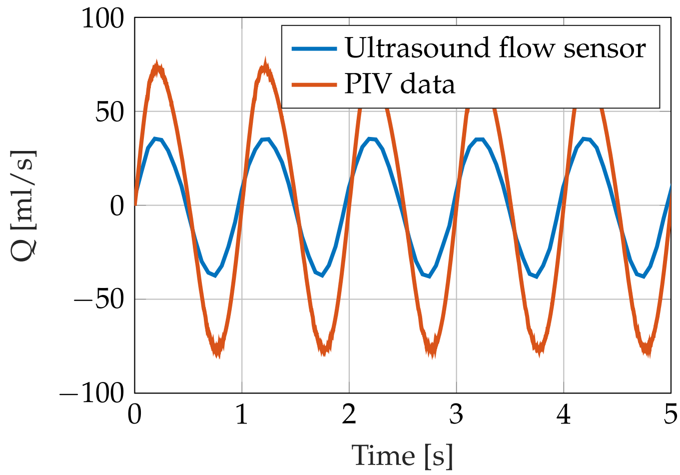


FIGURE 3.23: Comparison of the volumetric profile of the PIV data and the Ultrasound flow sensor of $\mathrm{Re}_{max}$ = 1350 long

the settings which are used are essential to accurately measure the rapidly changing waveform.

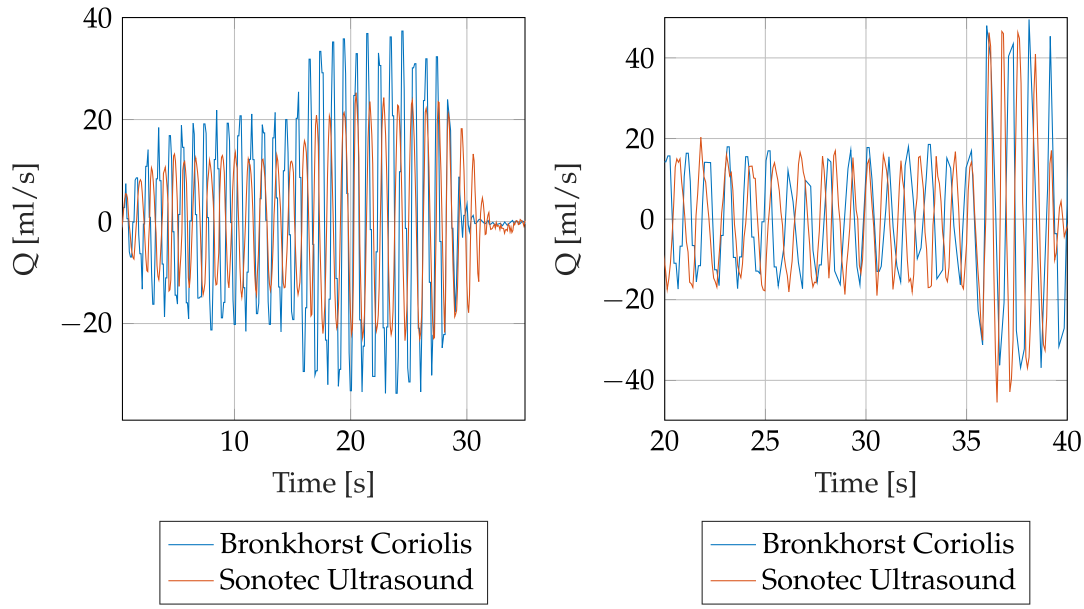


(A) Averaging over 32 samples

(B) Averaging over 8 samples

FIGURE 3.24: Comparison of the Coriolis and Ultrasound flow sensor. The flow is generated by the Vivitro pump

## 3.7 Discussion

### 3.7.1 Summary of the results

- The Vivitro pump was used to create a sine waveform, which could be accurately measured by the Coriolis MX55 flow sensor.
- By using Laser PIV it was possible to extract the velocity data from the experiments. The velocity and volumetric profiles are plotted and compared for the different Reynolds numbers. The results of the flow sensor match very closely with the volumetric PIV data, and thus the MX55 flow sensor can be used to extract the backward component in oscillatory flows.
- To optimize the setup and create a better sine waveform, the Coriolis flow sensor was replaced with an Ultrasound flow sensor. This lead to a lower resistance and therefore a better sine waveform. If the correct settings are used for the Ultrasound flow sensor, the performance is almost equivalent to the Coriolis flow sensor.
- A straw setup is designed to create fully developed flow within the straws and thus decrease the overall entrance length of the tube. The idea seems to work and the long straws seem to create a smoother flow, but future research is needed to quantify the influence of the different setups.
- After the introduction of the Ultrasound flow sensor the highest obtained $Re_{max}$ was 2200 with a sine waveform with a RMS of 10.0%. This $Re_{max}$ is in the range of a transition to turbulence, however no clear signs are noticeable in the centerline velocity plots. The $Re_{max}$ is too low or the lack of a disturbance, which can be a distorted waveform or geometry, does not trigger turbulence.
- During the analysis of the data it is assumed that the phantom is rigid. However, during the measurements the phantom deformed, due to the flow. At the highest $Re_{max}$ this deformation was more than 6% of the original diameter.

### 3.7.2 Discussion of the results

The results of the experiments are discussed and recommendations for future research are given in the following sections.

#### Flow setup

The implemented sine waveform is not perfect and there are some distortions, especially in the backward phase. The claimed accuracy of the Vivitro is $\pm$ 4-5% of the stroke volume [86], but at some instances there is a deviation of 10%. As far as is known the Vivitro pump has not been used for this type of experiments before, in which only one in/output is utilized to create a sine waveform. Therefore it could be that the performance of the Vivitro pump is less accurate in the backward flow direction, as such flows do not frequently occur in cardiovascular flows, which is the main application of the Vivitro pump. More research into the exact performance of the Vivitro pump during the forward and backward phase of the waveform is recommended, if a perfect sine waveform is desired.

The used working fluid, BMF, has a relatively high viscosity. By using a working fluid with a lower viscosity, such as water, the required velocity to obtain the desired

Reynolds numbers decreases. As the RMS error between the PIV data and the perfect sine waveform decreases at lower volumetric flow rates, this could improve the shape of the produced sine waveform.

The objective was to create an oscillatory flow which has a net displacement of zero. When a pure sine waveform is created this is obtained. However, when analyzing the volumetric flow rates in the different experiments, there seems to be a net positive displacement as the forward component is larger than the backward component. If the forward and backward component are not of equal size, this can influence the flow phenomena as described in Section 2.2.

Based on the obtained results in Section 3.6 the exact influence of the straws cannot be determined. The profile in the long straw setup is smoother at all locations in the phantom (upstream, center and downstream), than in the short straw setup. The velocity profile changes along the axial location of the phantom and seems smoother further downstream of the straws. This can indicate that the flow is (more) fully developed further downstream. The velocity profile of the long straw setup in Figure 3.16 shows peaks at the upstream location, while the center and downstream location show a smooth velocity profile. The short straw setup in Figure 3.15 shows similar results, the velocity profile upstream is full of peaks, while the location further downstream shows a smoother velocity profile. The length of the pipe after the straw holder, to combine the fully developed flows in the straws into one fully developed flow in the phantom, is chosen randomly, as there is no literature on this topic. It could be that the required length after the straw holder to ensure fully developed flow is exactly the length that has been chosen, and the flow is precisely fully developed in the long straw setup, while the short straw setup needs a longer piece of pipe to fully develop.

However, this cannot be said conclusively. It is unknown what the differences are between a fully developed and a not fully developed Womersley flow, thus this cannot be easily compared. Furthermore the increased noise upstream of the center could be due to a misalignment of the laser sheet, which can decrease the accuracy of the PIV data upstream of the center. When analyzing the raw data it appears that the quality of the data upstream is lower than in the rest of the FOV, as demonstrated in Figure 3.25. This may indicate that the laser sheet was not of the same thickness across the entire width, or that it was slightly tilted. The accuracy of the PIV algorithm can be decreased due to the lower amount of detected tracer particles, which can introduce the noise in the data upstream of the center.

Based on the results it might not be necessary to use straws to shorten the entrance length, as there is no clear difference between the forward and backward flow. Based on the theory of the entrance length a difference would be expected above $\mathrm{Re}_{max} \approx 1000$. As presented in Section 3.6, there is no clear difference noticeable in the forward and backward flow at $\mathrm{Re}_{max}$ of 1300 and 2200.

The required entrance length to ensure fully developed flow is not mentioned in most studies, even though it is relevant in studies on the transition to turbulence in (stenosed) pipe flow. In this type of research the obtained Reynolds numbers are above in 1000-2000, which makes the entrance length an important factor. Some researchers, such as Ahmed & Giddens [54] and Gomez et al. [52] guarantee fully developed flow by using an entrance tube of 2-4m. However, most researchers do not seem to include the entrance length in their setup design, or they just assume to have fully developed flow in their model. Hino et al. [45] [46] took the entrance length into account and used an entrance pipe for the forward and backward flow,

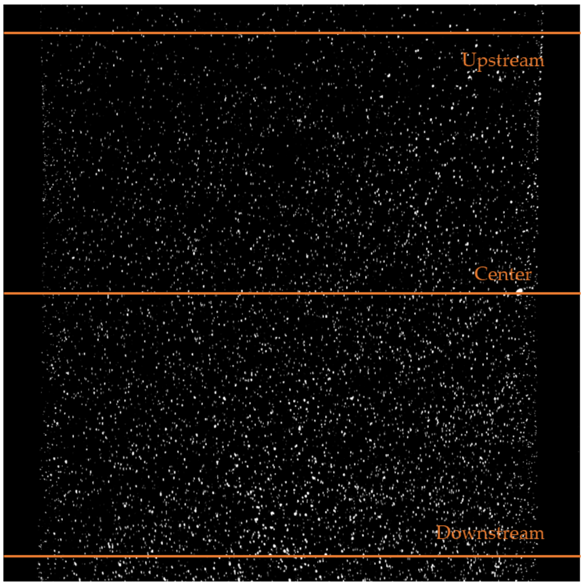


FIGURE 3.25: Raw image of the particle distribution.

as they studied a purely oscillatory flow with zero mean. Some studies in pulsatile or oscillatory flow that do include a long entrance tube to achieve fully developed flow, do not use this tube downstream of the model to ensure fully developed flow in the backward flow.

There is not much literature available on fully developed Womersley, and specifically oscillatory flow, and this raises many questions regarding the importance of the entrance length and why it is neglected in some research. Most research that is performed on pulsatile flows concerns cardiovascular flows, which do not have such a large backward flow component and operate at considerably lower Reynolds numbers, which usually do not exceed 1000. This can explain why the issue of a sufficiently long entrance length is not commonly addressed in studies.

To further verify the required entrance length to obtain fully developed flow and the use of straws to shorten the required entrance length, more research is needed. First experiments with a straight tube and steady, pulsating and oscillatory flow should be performed, to check the required entrance length in these three types of flow. It is expected that they differ, and that oscillatory flow has a slightly shorter entrance length [43] [44]. Analytical Womersley profiles could be plotted to verify the experimentally obtained velocity profiles and to note any differences. When the exact relationship between the Reynolds number, the type of flow and the entrance length is known, methods can be introduced to decrease the required entrance length.

The straw holders were introduced to decrease the required entrance length, but further research can better describe and quantify their effect. The straws can first be tested with a steady flow, as there is more knowledge on fully developed steady flow than on pulsatile flows. The phantom to capture the velocity field can be placed at several locations downstream of the straw holder to determine the exact location where the flow becomes fully developed. The velocity profile can be compared to the velocity profile without the straw holder and differences are expected above a certain Reynolds number. In the current setup this was expected above $\mathrm{Re}_{max} \approx 1000$.

For the oscillatory flow it is of interest to investigate any differences between the forward and backward flow, as in the current setup the straw holder was only placed in the forward flow. Since a fully developed flow is desired in both directions, the absence of the straw holder and the influence of the addition of a second straw holder downstream of the phantom could be investigated. Based on the results of these experiments, the straw holders can be omitted, a second one could be added downstream or even a completely new solution regarding the entrance length can be proposed.

When analyzing Figure 3.13, the error bars show an increased deviation on the left side of the phantom (thus negative values of y) in the short straw setup. This phenomena is not observed in the long straw setup in Figure 3.14. When comparing the geometry of the two types of straw holders, a difference can be noticed in the placement of the straws in the straw holders, as presented in Figure 3.7. The long straws have a circular shape and thus the straws are mainly evenly distributed in the tube. However, the short straws have more of an elliptical shape, and are thus more randomly distributed. As not all the fluid flows through the straws, but also in the space in between the straws, this can influence the flow. If the use of straws to shorten the entrance length is further investigated, the placement and orientation of the straws should be taken into account.

### PIV

Even though a presumably rigid pipe phantom is used, the walls of the phantom start to deform at high volumetric flow rates. The mask that is used in the PIV analysis is rigid and based on only one frame and this mask is used for the whole image sequence. However, due to the flow the walls of the phantom started to pulsate, this phenomena intensified with increasing Reynolds number as displayed in Table 3.9. Therefore it might be beneficial to use dynamic masking to extract the correct data at every frame [87].

A problem that can occur when air bubbles enter the flow circuit is that they can be visible in the images. When the air bubble blocks the view of the tracer particles in the FOV, this leads to data loss or incorrect data. Therefore it is important to create an air tight flow system. As air bubbles entered near the connection with the phantom, this connection will be optimized for the phantom in Chapter 4.

In this research 2D-2C PIV is used, and thus only the u- and v-component of the velocity can be extracted. In this part of the research this does not severely limit the possibilities as the flow is clearly in the laminar regime and the velocity profile is axisymmetric. However, a more advanced setup offers more possibilities to extract all the velocity data and better reconstruct the flow phenomena in the phantom. The drawback of the 2D method is that is not able to capture the z-component and this can also introduce an interference in the u- and v-component. By using multiple cameras, as mentioned by Ayegba [62], more components of the velocity tensor can be determined [63]. This increases the accuracy of the data and more information of the physical flow phenomena can be obtained. Techniques which can be used include Stereoscopic PIV and Tomographic PIV, of which Raffel et al. [63] give an extensive description.

### Flow sensor

In the research from Mirgolbabaee [41] the author suggested to control the Bronkhorst MX55 Coriolis flow sensor directly, to optimize its functionality. During the first phase of the experiments, research was conducted into this control function in Python. However, as the Sonotec Ultrasound flow sensor was introduced and preferred, it was not continued. It is still recommended to control the sampling time and other options directly by the Python script [88], as it will improve the performance of the flow sensor.

The benefit of the Sonotec Ultrasound flow sensor is the large diameter of the calibration tube, which did not lead to a resistance in the flow system. However, as this flow sensor is designed for very large flow rates (see Section 3.5), the accuracy at low flow rates is lower than desired. Especially when using the settings discussed in Section 3.6, the accuracy decreases due to the tradeoff that has to be made between accuracy and response time.

The used software for the Sonotec flow sensor is the FS02M software from Sonotec. This software offers limited capabilities for exporting data and especially the temporal resolution is low and not constant. By using the analogue outputs and sending these to an analogue recorder, the data can be analyzed and stored in a more convenient way. The sample time of the Ultrasound flow sensor was not constant, and the claimed sample time of 10ms was not achieved. On average there were approximately 15 data points each second. It should be further investigated how the temporal resolution can be improved.

During some of the experiments air bubbles were able to enter the flow circuit. This can lead to several problems during the experiment itself and the analysis of the data. The performance of ultrasound flow sensors can be influenced by air bubbles, as the ultrasound gets scattered and absorbed by the bubbles. When the bubble volume fraction exceeds 1%, the transient time method, which the Sonotec ultrasound flow sensor uses, is nearly useless [89].

### Phantom

As described in Section 3.2.2 the current flow model is made from PDMS and the RI of PDMS matches with the RI of BMF. Water represents the physical properties of CSF but BMF has a slightly higher density and it is 4 times more viscous than water. The initial idea was to use water as a working fluid as this seemed more convenient. One of the requirements is that the RI of the working fluid and the material of the phantom have to match. The RI of water is 1.33 and PDMS 1.41, thus it does not satisfy the set requirement. There are two options: Increase the RI of water by adding additives, or decrease the RI of the phantom by changing the material. Both options proved to be more difficult than expected. In the BMF solution that is used, urea is added to increase the RI [83]. This also leads to a higher viscosity and density, which is not desired in this case.

Choosing a material for the phantom with a RI around 1.33 is difficult, as shown in Figure 3.26. Most materials, especially the silicone elastomers which can be poured in a mould, have a higher RI. FEP has optical properties that are favourable to use, however the physical properties do not match the requirements. It cannot be easily poured into a mold to produce a phantom.

Yazdi et al. provide an extensive overview of phantom and their fabrication techniques [82]. However, most models focus on RI matching with blood. There are methods and materials that do match the RI of a material and water. These include using hydrogels [91], or matching of the RI in microfluidics [92] [93]. These methods are not useful in this study, as a phantom has to be constructed through which the fluid flows.

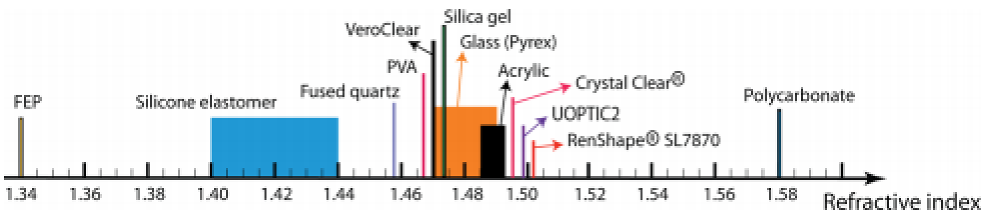


FIGURE 3.26: Refractive index of different solids. Image from Bai et al. [90]

## 3.8 Conclusion

The main focus of this chapter was to characterize and build a PIV setup that is able to create and visualize oscillatory flow. The Vivitro pump was used to create a sine waveform, which has a maximum RMS of 10%, and by using laser PIV it was possible to extract the velocity data from the experiments. The velocity and volumetric profiles have been plotted and compared for the different Reynolds numbers. The results of the flow sensors match very closely with the volumetric PIV data, and thus the Coriolis and Ultrasound flow sensors can be used to extract the backwards component in oscillatory flows. To decrease the required entrance length to ensure fully developed flow, a straw holder has been designed.

The highest obtained $Re_{max}$ of 2200 is in the range of a transition to turbulence, however no clear signs are noticeable in the centerline velocity plots. The $Re_{max}$ is too low or there is lack of a disturbance, which can be a distorted waveform or geometry, and thus turbulence is not yet triggered in the flow.

During the analysis of the data it is assumed that the phantom is rigid. However, during the measurements the phantom deformed up to 6%. In addition to providing a good basis for the research in Chapter 4, the results in this chapter also offer many new possibilities for research in the directions of fully developed flow and the transition to turbulence in a straight pipe flow.

# Chapter 4

# Fluid mechanics in a stenosis under oscillatory flow conditions

## 4.1 Introduction

A broad range of neurological conditions, such as ALS and Alzheimer's, have been linked to an impaired flow of CSF [3] [4]. However, there are still a number of unclarities about the flow of CSF in the human body. An overview of the related background theory on CSF is discussed in Section 2.1. Researchers have found evidence that due to the very complex geometry of the SAS, the flow of CSF can locally transition to the turbulent regime [9]. If the flow actually transitions from the laminar to the turbulent regime, this can indeed change the flow dynamics of CSF. Conditions such as Chiari I malformation can obstruct the flow of CSF in the SAS, which further alters the dynamics of the flow. Research by Jain et al. [6] showed that even though the Reynolds numbers are low, the flow seems to transition to the turbulent regime. It is important to understand the influence of an obstruction on the physics of flow. As this can lead to novel insights in several medical conditions and drug delivery [35].

In order to study the flow dynamics of CSF in an obstruction, a simple, but anatomically relevant stenosis is introduced as geometry. This model with a stenosis of 75% has been used before in other research [54] [55]. The goal of the research by Jain [8] is similar to this thesis. The physics of oscillatory flow in a stenosis of 75% are investigated and the possible transition to turbulence is discussed. As there is no experimental data yet that covers this research area, this is the main goal of this chapter.

The models that Jain studied were both an eccentric and an axisymmetric model with a 75% stenosis. The eccentric model already transitions at a Re = 1800 while the axisymmetric model steps into the transitional regime around Re = 2100 [8]. He investigated the onset of turbulence for oscillatory and pulsatile flows and found that the critical Reynolds number is three times higher in a purely oscillating flow compared to pulsatile flow. This is due to the reversal of the flow and the accompanying relaminarization (see Section 2.2.3).

In this part of the thesis oscillatory flow experiments through an axisymmetric stenosis of 75% are described, to investigate the influence of an obstruction on the fluid dynamics of CSF. As the onset of turbulence is physiologically relevant and of interest in this thesis, the experiments are performed at increasing Reynolds numbers. The setup that has been described in Chapter 3 is used to visualize the oscillatory flow through the stenosis. In Section 4.2 the geometry and production of the phantom is discussed, including an overview of the method of the experiments. The results of the experiments are discussed and a first comparison to the simulations of Jain [8] is made.

## 4.2 Method

In this section a brief overview of the method is discussed. As most of the setup is the same as in Chapter 3, the reader is referred to this chapter for an extensive description of the used methods and setup. The new stenosed phantom is the main focus of this section and will be discussed below.

### Phantom with stenosis

The geometry that was selected for the stenosis has previously been used by Jain [5] and Varghese et al. [55] and can be found in Figure 4.1. In this figure two different configurations of the stenosis are displayed, the axisymmetric and eccentric. For this research only the axisymmetric configuration has been used, which is displayed by the solid line in Figure 4.1. The reader is referred to Jain [5] and Varghese et al. [55] for more information regarding the eccentric configuration.
Function S, which is dependent on the axial coordinate, was used to define the shape of the stenosis. Both cross-stream coordinates $y$ and $z$ are computed by using:

$$\left.\begin{array}{l} S(x) = \frac{1}{2}D\left[1 - s_0\left(1 + \cos\left(2\pi\left(x - x_0\right)/L\right)\right)\right] \\ y = S(x)\cos\theta, \quad z = S(x)\sin\theta \end{array}\right\} \tag{4.1}$$

The cosine function is used to generate the geometry presented in Figure 4.1a. In Equation 4.1 D is the diameter of the non-stenosed pipe, L is the length of the stenosis, which is 2D as shown in Figure 4.1a. The value for $s_0$ is 0.25 and the centre of the stenosis is denoted as $x_0$. The stenosis of interest for this thesis is an axisymmetric stenosis of 75%. A reduction of 75% in area leads to a diameter of 0.5D in the centre of the stenosis. The diameter of the pipe is the same as the phantom in Chapter 3, thus D = 24.25mm.

To produce the phantom, the following procedure was followed:

1. The above mentioned geometry was modelled in Solidworks software.
2. A 3D printer was used to print the model from Acrylonitrile Butadine Styrene (ABS), see Figure 4.2a.
3. The printed model was placed in a reservoir, and silicone PDMS Sylgard 184 was poured over the printed model to create the phantom.
4. The reservoir was placed in an oven for 1.5 hour to fully cure the PDMS.
5. The model was taken out of the reservoir after the PDMS was fully cured, see Figure 4.2b.
6. Acetone was used to flush the phantom to remove the ABS on the inside. The final model is presented in Figure 4.2c.

The total length of the phantom is 242mm, which corresponds to 5D downstream and 5D upstream of the stenosis throat. Two connection parts, where the entrance tubes can be connected, of 30mm are located on both sides. As the phantom pulsated and therefore deformed heavily during the experiments in Chapter 3, the wall thickness has been increased. The wall thickness of the phantom in Chapter 3 was not constant and ranged from 5 to 15mm. In the newly designed phantom the wall thickness was increased to 23mm on all sides, to ensure a rigid phantom.

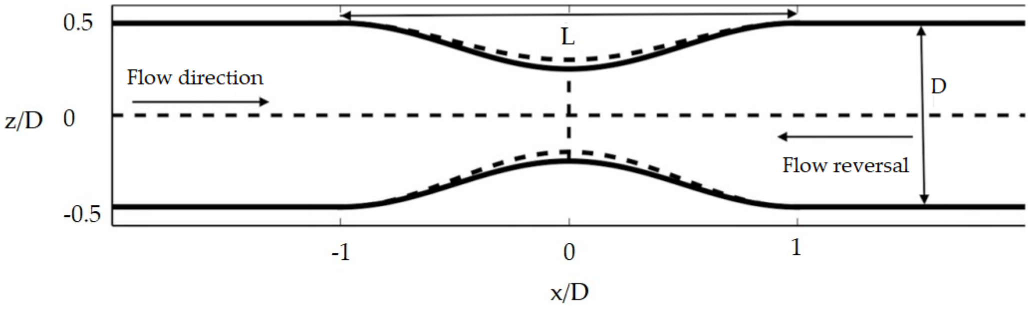


(A) Front view

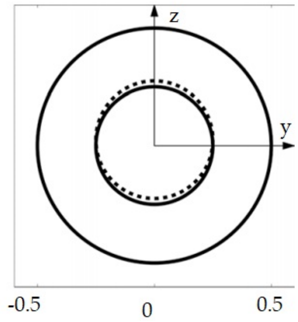


(B) Side view

FIGURE 4.1: Schematic of the front and side view of the stenosis geometry. The flow direction is denoted by x, cross-stream directions are y and z. The solid line shows the axisymmetric geometry and the dashed line to eccentric geometry. Image modified from Jain [8] and Varghese et al. [55]

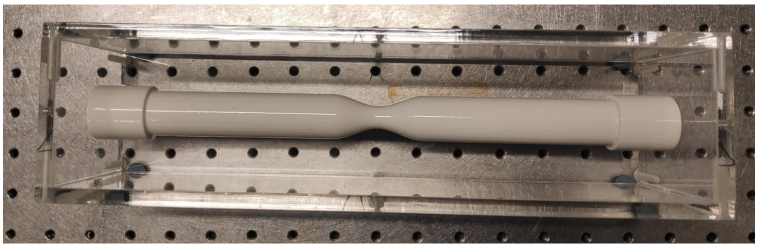

(A)

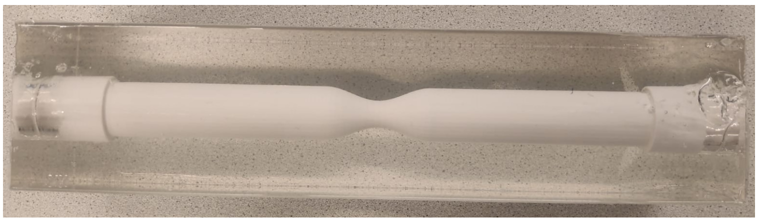

(B)

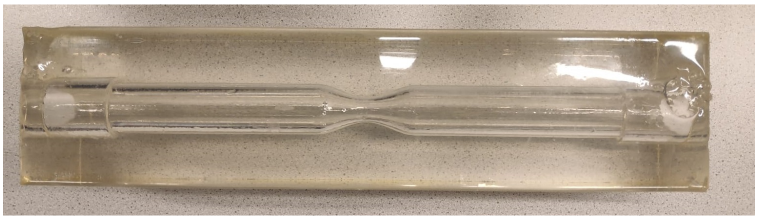

(C)

FIGURE 4.2: A) The 3D printed mold and reservoir. B) The phantom after pouring the PDMS and removing the reservoir. C) The final phantom after removing the ABS mold by flushing with aceton.

### PIV analysis

The obtained data is analyzed in the same way as in Chapter 3. As the FOV of the used camera and lens is limited, only a certain region of the phantom can be captured in the FOV. As the flow usually transitions at a certain distance downstream of the stenosis, the FOV is directed here. Based on the simulations of Jain [8], the transition is expected in between 2D and 4D downstream . Two different locations have been selected such that the information of 1D, 2D and 3D downstream can be captured.

The same temporal locations as in Chapter 3 are analyzed, these are shown in Figure 3.6. As the velocities in these experiments are higher than in the previous chapter, the images are recorded at 3000 fps to still satisfy the one quarter rule (Section 2.3.4). 10 cycles have been captured, however only 5 cycles have been analyzed due to the computational effort. The IA size of the first pass is 128×128 and three more passes of 64×64, 32×32 and 32×32 are used. The overlap of the IAs was 50%. The FOV was approximately 35 × 35mm, which leads to a spatial resolution of 0.55 × 0.55 mm.

The two recorded FOV are depicted in Figure 4.3. The location of 1D downstream is known, as this is located at the end of the stenosis throat (see Figure 4.1 for a schematic picture). By creating an overlap of 25/30% of the FOV, the location of 2D could be determined in the second FOV. The location of the FOV was marked on the phantom itself, such that it could be checked and verified after the experiments. The location 3D is then determined as 1D (thus 24.25 mm) further downstream. In this way the data from 1D, 2D and 3D downstream could be extracted from the obtained images. The centerline is displayed in Figure 4.3, as in the results the velocity along this line is extracted.

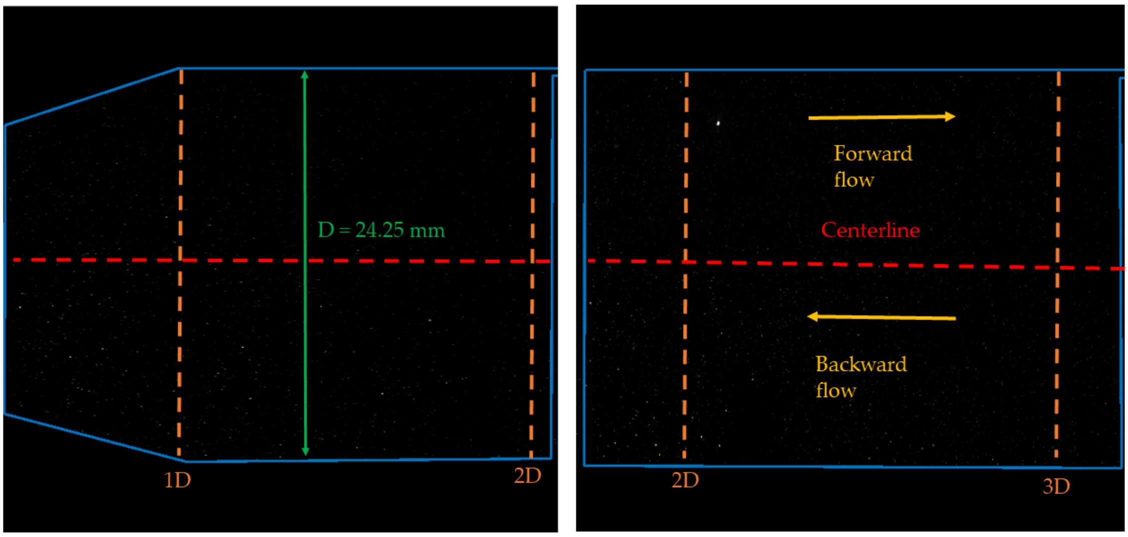


FIGURE 4.3: Overview of the FOV of the stenosed phantom experiments. The mask is displayed in blue and the locations downstream the stenosis throat are marked.

### Reynolds number

In Chapter 3, three different ways to compute Reynolds number were introduced (see Table 3.4). The same methods are used in this chapter to compute the Reynolds number for the different experiments. The value for D, the diameter, is based on the phantom without the stenosis. Thus the main diameter of the phantom is used, and not the local decreased diameter due to the stenosis. The local Reynolds number is different due to the 75% stenosis. The working fluid and tube diameter are the same as in Chapter 3 and the same sine waveform with a frequency of 1 Hz is implemented. Therefore the Womersley number is equal to the value in the previous chapter and is approximately 15.9.

### Power spectral density

Turbulent flow consists of eddies, which are swirling motions of a fluid in a turbulent flow regime. These eddies have different sizes and their size changes in the flow. The large eddies are unstable and break up, transferring their energy to smaller eddies. This process, called energy cascade, repeats itself multiple times until the Reynolds number is sufficiently small that the eddy motion is stable. At these very small scales, the viscosity is effective and the kinetic energy of the turbulence is converted into heat [94].

To investigate if there is turbulence in the flow, the power spectrum of the turbulent kinetic energy is plotted. By studying these plots, the flow phenomena and corresponding (turbulent) energy can be analyzed. As the energy is transferred from the large to the small eddies, the energy spectrum in the inertial subrange can be described by Kolmogorov's theory [94]. If the decay in the experimental data shows similarities to the $\frac{-5}{3}$ decay of Kolmogorov, this would imply that turbulent phenomena occur in the flow. The centerline velocity profiles are used as an input and Welch's periodogram is used to estimate the spectral density. This method reduces the noise in the data, which is caused by imperfect and finite data.

## 4.3 Results

In this section the results of the experiments in a stenosed pipe are presented. First a cycle to cycle comparison is made, and the differences with the velocity profiles in the previous chapter are explained. The velocity and volumetric profiles of all the experiments are presented, together with an analysis of the obtained Reynolds numbers. As the jet breakdown location and the possible transition to turbulence are important to answer the research questions, the axial centerline velocity and the centerline velocity over time are plotted.

To get more insight into the transition from laminar to turbulent flow, the velocity data is used to plot the power spectral density (PSD) of all the different Reynolds numbers.

### Overview of experiments

An overview of the performed experiments and their corresponding Reynolds numbers is presented in Table 4.1. The results of the experiments with the $\mathrm{Re}_{max}$ = 1200, 2000, 2100 and 2300 are discussed below. As the flow phenomena of the measurement of $\mathrm{Re}_{max}$ = 500 are completely different, these results will be discussed separately. As the Reynolds numbers are based on the (processed) data, it is not realistic to define them as a specific number with $\delta\mathrm{Re} = 1$. Therefore they are rounded to a nearest number and give more of an indication or range than a specific number.

| $Q_{max}$ [ml/s] | $v_{max}$ [m/s] | $\mathrm{Re}_{max}$ | $v_{peak}$ | $\mathrm{Re}_{peak}$ | $v_c$ | $\mathrm{Re}_{avg}$ |
|---|---|---|---|---|---|---|
| 22 | 0.08 | 500 | 0.048 | 300 | 0.022 | 150 |
| 57 | 0.18 | 1200 | 0.123 | 800 | 0.085 | 550 |
| 105 | 0.30 | 2000 | 0.23 | 1500 | 0.17 | 1250 |
| 104 | 0.32 | 2100 | 0.225 | 1500 | 0.22 | 1455 |
| 110 | 0.35 | 2300 | 0.238 | 1600 | 0.275 | 1800 |

TABLE 4.1: Table with flow rates, velocities and different Reynolds numbers from the experiment. $\mathrm{Re}_{max}$ is based on the maximum velocity obtained by the velocity profile, $\mathrm{Re}_{peak}$ is based on the theoretical inlet velocity of the sine waveform and $\mathrm{Re}_{avg}$ is the average Reynolds number based on the half-cycle averaged centerline velocity. The data is based on the backward flow, as the forward flow shows locally increased Reynolds numbers due to the stenosis.

In Chapter 3 every cycle is approximately the same and thus the averaged velocity profile does not differ much from a single cycle. However, in the results of the stenosed experiments, the velocity profile differs in every cycle. The results of $\mathrm{Re}_{max}$ = 2000 are demonstrated in this section. The results of 1D downstream of the stenosis throat are shown in Figure 4.4. Just downstream of the stenosis throat there is only a minor difference between the two cycles. At 2D downstream of the stenosis, the velocity profile already looks different and especially at 3D downstream of the stenosis, the shape of the velocity profile is no longer constant. These results are demonstrated in Figure 4.5 and 4.6 respectively. This is likely due to the breakdown location of the jet, which will be discussed later in this chapter.

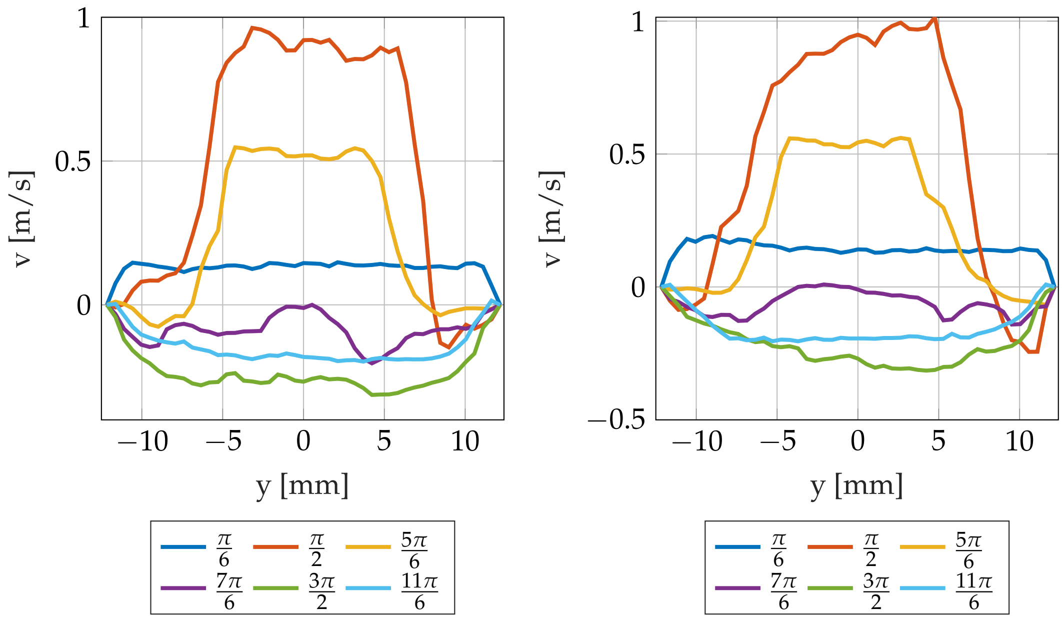


(A) $\mathrm{Re}_{max} = 2000$ at 1D downstream, cycle 1 (B) $\mathrm{Re}_{max} = 2000$ at 1D downstream, cycle 2

FIGURE 4.4: Velocity profile of $\mathrm{Re}_{max} = 2000$ at 1D downstream of the stenosis during two consecutive cycles.

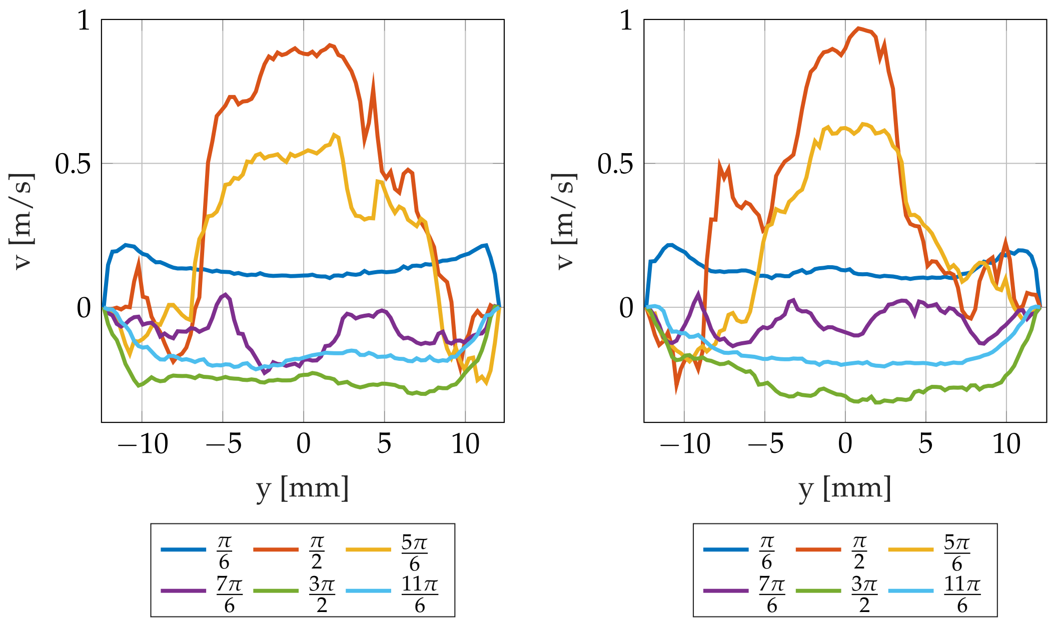


(A) $\mathrm{Re}_{max} = 2000$ at 2D downstream, cycle 1 (B) $\mathrm{Re}_{max} = 2000$ at 2D downstream, cycle 2

FIGURE 4.5: Velocity profile of $\mathrm{Re}_{max} = 2000$ at 2D downstream of the stenosis during two consecutive cycles.

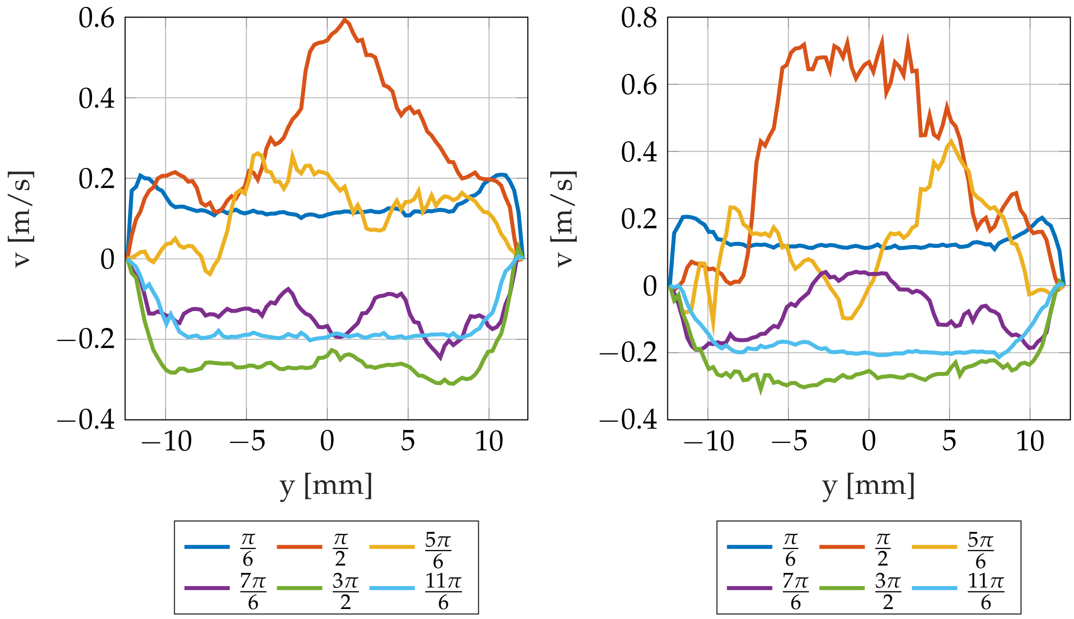


(A) $Re_{max}$ = 2000 at 3D downstream, cycle 1 (B) $Re_{max}$ = 2000 at 3D downstream, cycle 2

FIGURE 4.6: Velocity profile of $Re_{max}$ = 2000 at 3D downstream of the stenosis during two consecutive cycles.

### 4.3.1 Averaged velocity profiles

The velocity profiles of $Re_{max}$ = 2000 that are averaged over 5 cycles are presented in Figure 4.7. In Figure 4.7a the velocity profile at 1D downstream of the stenosis is displayed, where a clear plug profile is visible. In Figure 4.8b the velocity profile of $Re_{max}$ = 2000 at 2D downstream is shown, where the peak velocity has slightly decreased but is still considerably higher than the inlet velocity. The velocity profile of 3D downstream is presented in Figure 4.7b. The peak velocity has significantly decreased and there is no clear jet structure visible, in contrast to the locations closer to the stenosis throat.

The axial velocity profiles of four different Reynolds numbers are presented in Figure 4.8 and 4.9. The data is shown 2D downstream of the stenosis and is averaged over five cycles. At all four Reynolds numbers a jet structure is still visible and the peak velocity is at $\frac{\pi}{2}$, which is the peak forward volumetric flow rate. The velocity at $\frac{\pi}{6}$ is low, but during the peak volumetric rate ($\frac{\pi}{2}$) and the deceleration phase ($\frac{5\pi}{6}$) a sudden increase occurs in the velocity. In the backward phase the velocities are not locally increased as there is no stenosis in the direction of the flow. The increased velocity profiles will occur at x = -2D, on the other side of the stenosis throat, which is not visible in this data.

The volumetric profiles obtained by the PIV analysis are demonstrated in Figure 4.10 and Figure 4.11. The data of the lowest Reynolds number, $Re_{max}$ = 1200 is presented in Figure 4.10a and the forward and backward phase are approximately the same. However, the volumetric profiles of the higher Reynolds numbers show inconsistent values at the peak forward flow rate. The peak value is heavily increased and shows large distortions of the implemented sine waveform. This is due to the fact that the volumetric flow rate is obtained just downstream of the stenosis, where the local velocities are heavily increased due to the reduced diameter of the stenosis. During the forward phase of the cycle, the flow downstream of the stenosis experiences distortions, which are stabilised during the reversal of the flow. Thus, $Q_{max}$, $v_{peak}$ and

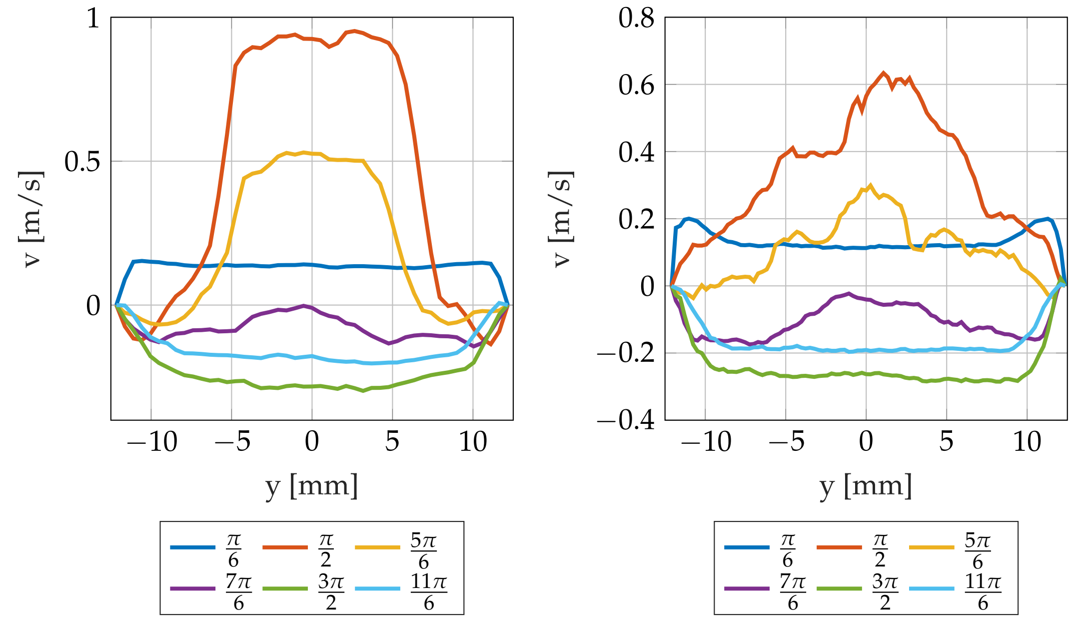


(A) $Re_{max}$ = 2000 at 1D downstream

(B) $Re_{max}$ = 2000 at 3D downstream

FIGURE 4.7: The averaged velocity profile of $Re_{max}$ = 2000 averaged over 5 cycles at 1D and 3D downstream.

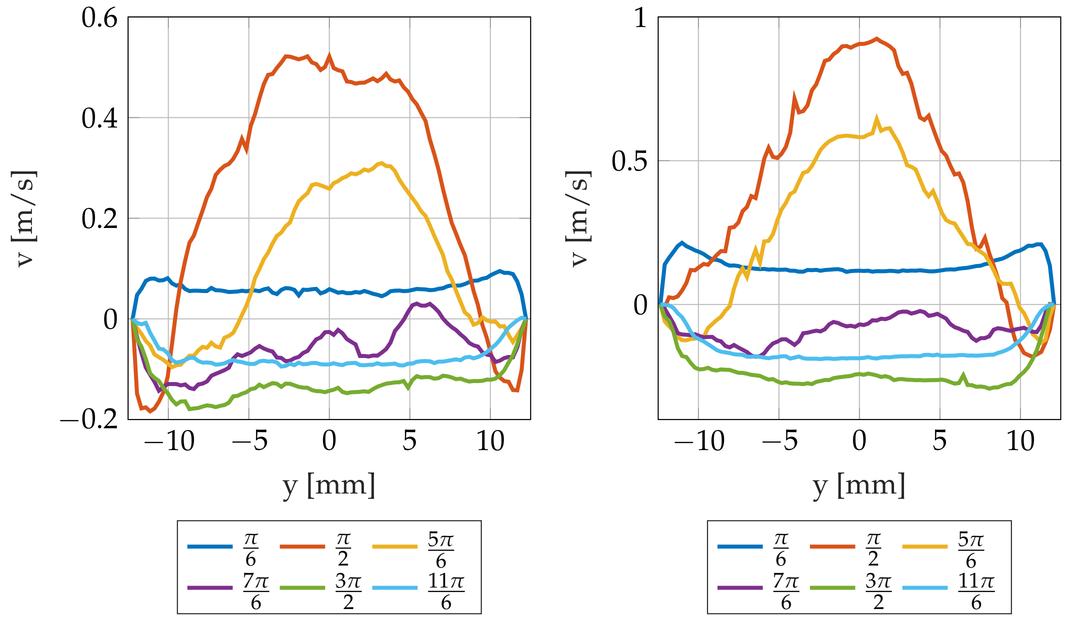


(A) $Re_{max}$ = 1200 at 2D downstream

(B) $Re_{max}$ = 2000 at 2D downstream

FIGURE 4.8: The averaged velocity profile of $Re_{max}$ = 1200 and $Re_{max}$ = 2000 averaged over 5 cycles at 2D downstream.

$Re_{peak}$ were analyzed during the reverse phase of the flow, as displayed in Table 4.1. As the peak volumetric rate in the backward flow only slightly increased during the last 3 measurements ($Q_{max}$ = 105, 104 and 110 ml/s), there is only a minor difference in the $Re_{peak}$. However, when comparing the $v_{max}$, which is obtained from the maximum velocity of the averaged velocity profile as presented in Figures 4.8 and 4.9, a difference in the maximum velocities is visible which leads to an increasing $Re_{max}$.

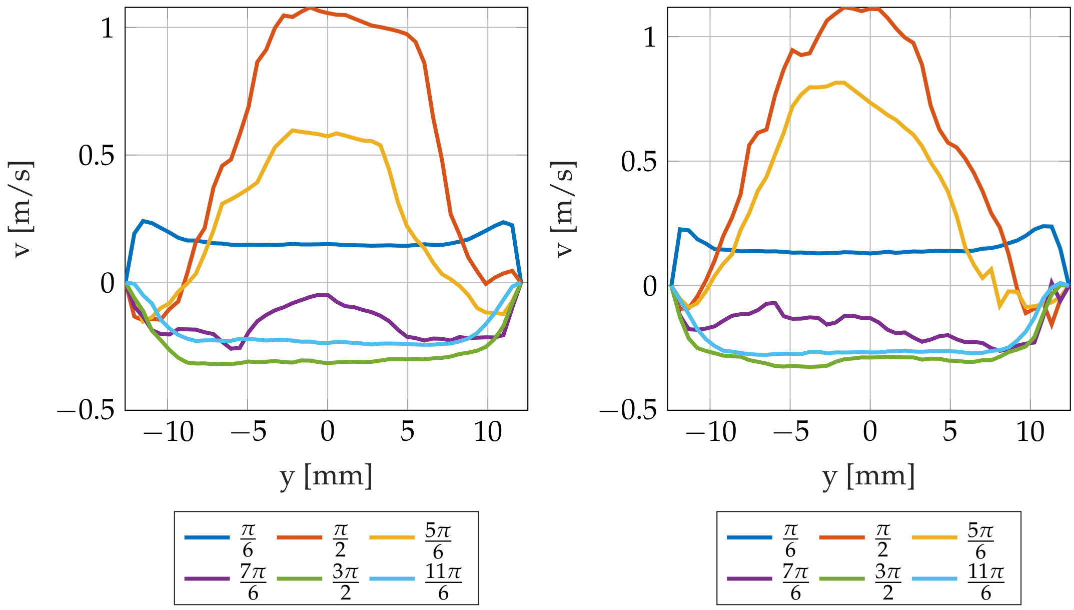


(A) $Re_{max}$ = 2100 at 2D downstream

(B) $Re_{max}$ = 2300 at 2D downstream

FIGURE 4.9: The averaged velocity profile of $Re_{max}$ = 2100 and $Re_{max}$ = 2300 averaged over 5 cycles at 2D downstream.

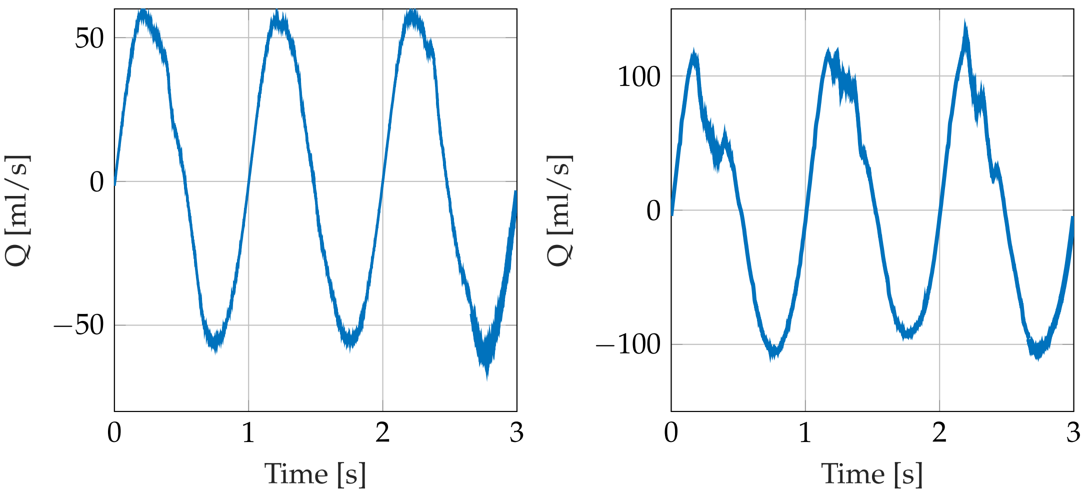


(A) $Re_{max}$ = 1200

(B) $Re_{max}$ = 2000 Volumetric flow rate

FIGURE 4.10: The volumetric profile of $Re_{max}$ = 1200 and $Re_{max}$ = 2000.

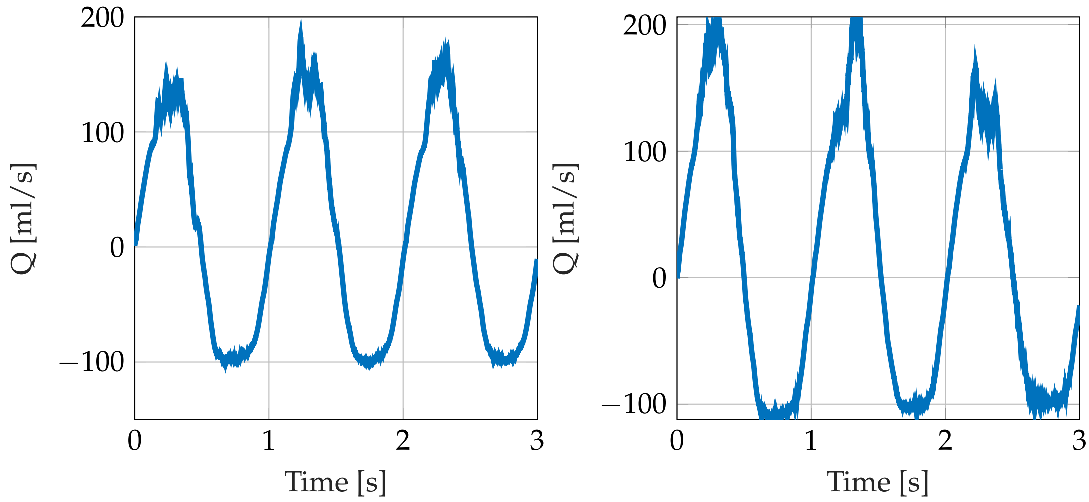


FIGURE 4.11: The volumetric profile of Re$_{max}$ = 2100 and Re$_{max}$ = 2300.

### 4.3.2 Centerline velocities

#### Spatial

In the axial velocity profiles of different locations downstream of the stenosis throat, see Figures 4.7a, 4.7b and 4.8b, a jet structure was visible which seemed to break down in between 2D and 3D downstream of the stenosis throat. To determine the jet breakdown location more precisely, the centerline velocity has been plotted over the axial distance of the phantom (x-coordinate).

When the jet breaks down, a point of inflection is formed at the breakdown location which creates a vortex ring. At this point the velocity of the incoming jet drops down considerably. Thus, the spatial location along the centerline where the velocity shows a dramatic decrease can give a surrogate indication of the jet breakdown location [95]. The velocity is plotted at the spatial locations in between 2D and 3D downstream of the stenosis and the results are presented in Figure 4.12 and 4.13. The temporal location that is used to plot the axial centerline velocity is $\frac{5\pi}{6}$ , which is in the deceleration phase. This is the most likely temporal location where a transition to turbulence could occur, and is therefore analyzed to discover drops in the velocity. In the Re$_{max}$ = 1200 a significant drop in the centerline velocity is observed around 2.5D downstream of the stenosis throat. For the increasing Re$_{max}$ the drop down location shifts closer to the stenosis throat, however it is more difficult to specify a location as the drop in velocity is more gradually.

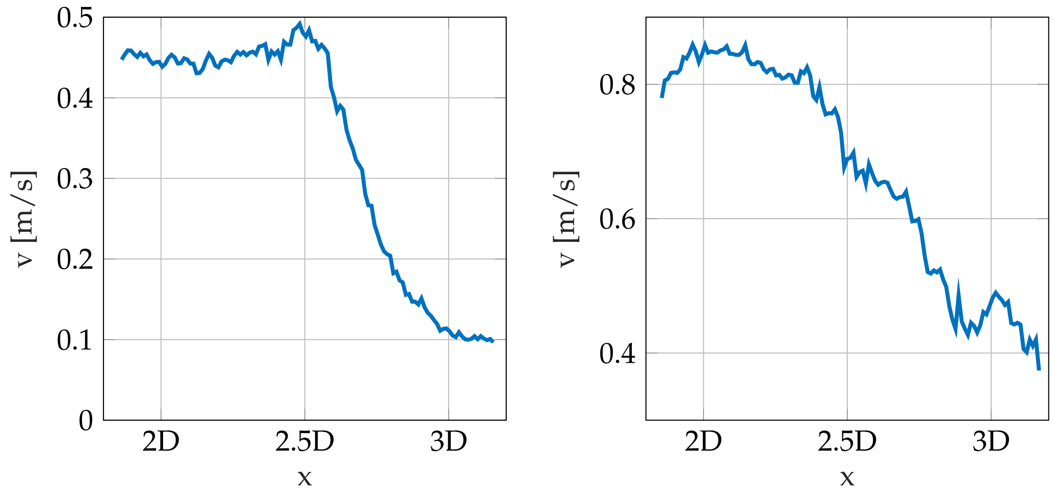


(A) Axial centerline velocity $Re_{max}$ = 1200. (B) Axial centerline velocity $Re_{max}$ = 2000.

FIGURE 4.12: The axial centerline velocity of $Re_{max}$ = 1200 and $Re_{max}$ = 2000 averaged over 5 cycles.

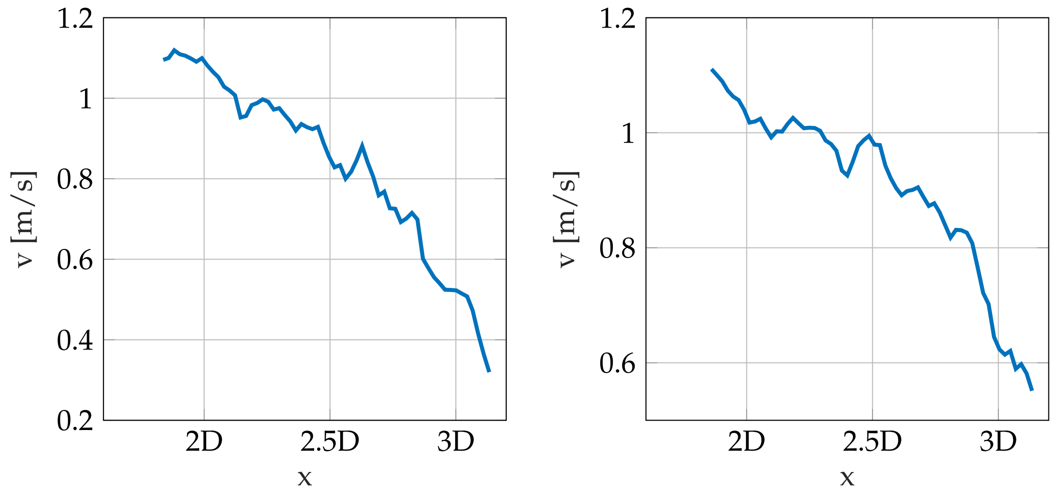


(A) Axial centerline velocity $Re_{max}$ = 2100. (B) Axial centerline velocity $Re_{max}$ = 2300.

FIGURE 4.13: The axial centerline velocity of $Re_{max}$ = 2100 and $Re_{max}$ = 2300 averaged over 5 cycles.

**Temporal**

The centerline velocity over time is shown in Figures 4.14 and 4.15. The spatial location of these plots are at the location which corresponds with the jet breakdown locations in Figures 4.12 and 4.13. At $Re_{max}$ = 1200 the centerline velocity shows a sudden increase at $\frac{\pi}{2}$, where the peak velocity is approximately 3 times higher. In between $\frac{\pi}{2}$ and $\frac{5\pi}{6}$ the velocity decreases, and thus the peak with heavily increased velocities is relatively small. As the Reynolds number increases, the width of the peak increases significantly. The peak starts earlier than $\frac{\pi}{2}$ in Figure 4.14b and lasts until $\frac{5\pi}{6}$. At the experiments with $Re_{max}$ = 2100 and $Re_{max}$ = 2300, demonstrated in Figures 4.15a and 4.15b respectively, the increased centerline velocity peaks over a longer period of time. In the backward flow, there is no peak value visible as the reversal of the flow leads to relaminarization of the flow. A clear difference is visible between the centerline velocities in this chapter, and the centerline velocities in Chapter 3 which are presented in Figure 3.21 and 3.22. The introduction of the stenosis leads to increased velocities, especially during the peak forward phase and the subsequent deceleration of the flow. The flow seems to transition at $\approx 2.5D$ downstream of the stenosis throat at $Re_{max} = 1200$ and the location of transition shifts closer to the stenosis throat at increasing $Re_{max}$. There was no noticeable difference in the jet breakdown location of the measurements at $Re_{max} = 2000$, 2100 and 2300, they seem to break down in between 2D and 2.5 downstream. Therefore it is unknown whether the breakdown location shifts even closer to the stenosis throat with $Re_{max} \geq 2000$.

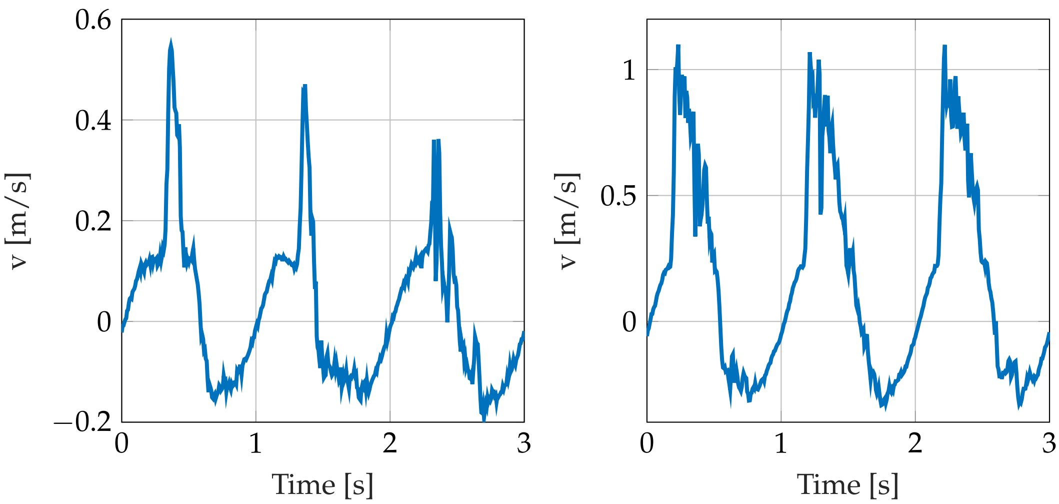


(A) Centerline velocity $Re_{max} = 1200$ at 2.5D

(B) Centerline velocity $Re_{max} = 2000$ at 2D

FIGURE 4.14: The centerline velocity of $Re_{max} = 1200$ and $Re_{max} = 2000$ during the first three cycles.

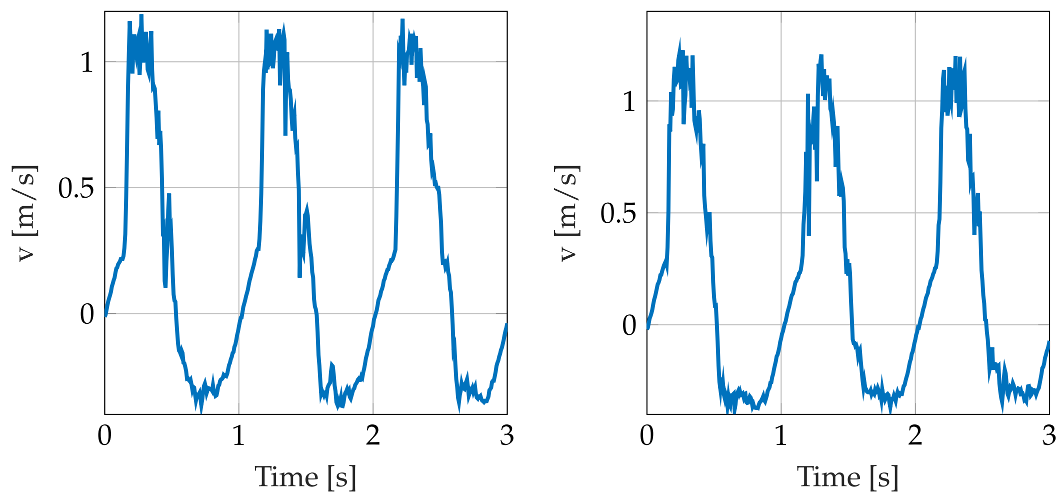


(A) Centerline velocity $Re_{max} = 2100$ at 2D.

(B) Centerline velocity $Re_{max} = 2300$ at 2D.

FIGURE 4.15: Centerline velocity of $Re_{max} = 2100$ and $Re_{max} = 2300$ during the first three cycles.

### 4.3.3 Highest Reynolds number

To get more insight in the physics of flow, the contour plots of the velocity magnitude are presented in Figure 4.16 and Figure 4.17. Two FOV are displayed, such that the data between 1D and 3D downstream can be analyzed. The solid line corresponds to 1D downstream and the dotted line corresponds to 2D downstream in Figure 4.16. The second FOV is located in between approximately 2D (dotted line) and 3D (dashed line), this is shown in Figure 4.17. The y-axis ranges from approximately -5mm to -29mm, which corresponds to the diameter of the tube. The data of $Re_{max}$ = 2300 is displayed, which is the highest obtained Reynolds number. Two temporal locations are presented, the peak value at $\frac{\pi}{2}$ and the deceleration phase at $\frac{5\pi}{6}$, which are marked on the sine waveform. In Figure 4.16a the jet formed in the stenosis is clearly visible, while further downstream in Figure 4.17a the velocity magnitude decreases. The velocity magnitude in the deceleration phase is presented in Figure 4.16b. The velocity magnitude decreases, but the jet is still visible. Near the wall the fluid starts to move backwards, while the central core keeps moving forward. The contour plot in Figure 4.17 shows the decreased velocity magnitude and the recirculation zones that occur during the deceleration phase.

The same FOV are used to display the vorticity in Figure 4.18 and Figure 4.19. The jet is visible just downstream of the stenosis at $\frac{\pi}{2}$ and $\frac{5\pi}{6}$. These are the temporal locations of the cycle with the highest vorticity. The jet weakens at $\frac{5\pi}{6}$ and the vortices seem to spread further downstream of the stenosis. During the deceleration phase recirculation zones appear around 2D downstream of the stenosis. These are not observed close to the stenosis throat. During the reversal of the flow, the flow relaminarizes due to the rest and acceleration of the fluid.

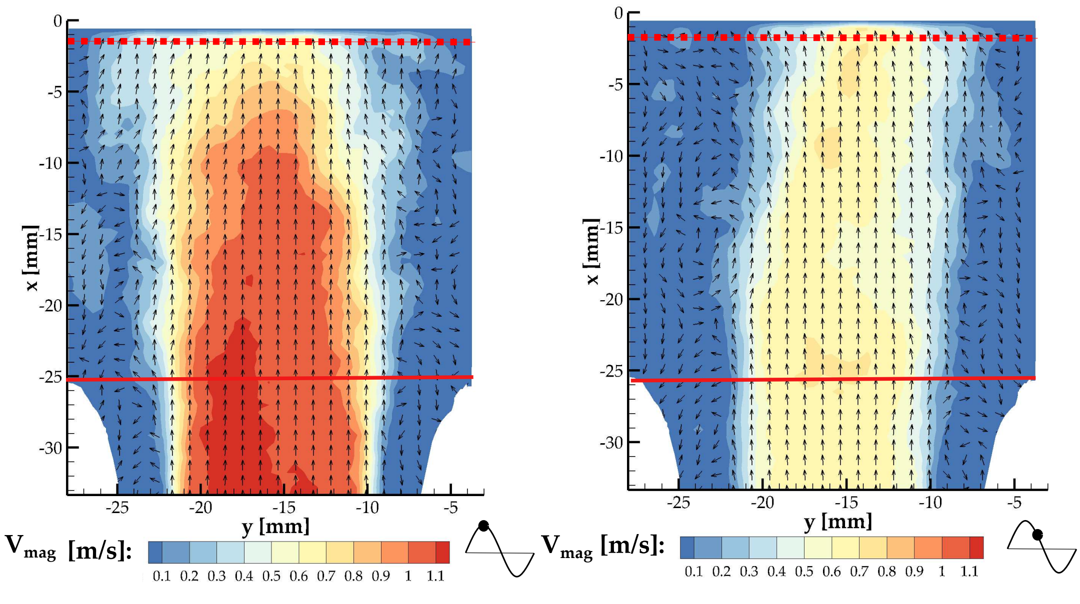


(A) Velocity magnitude of $Re_{max}$ = 2300 at $\frac{\pi}{2}$

(B) Velocity magnitude of $Re_{max}$ = 2300 at $\frac{5\pi}{6}$

FIGURE 4.16: Velocity Magnitude of $Re_{max}$ = 2300 at $\frac{\pi}{2}$ and $\frac{5\pi}{6}$ in between 1D and 2D downstream of the stenosis. The solid line corresponds to 1D downstream and the dotted line to 2D downstream.

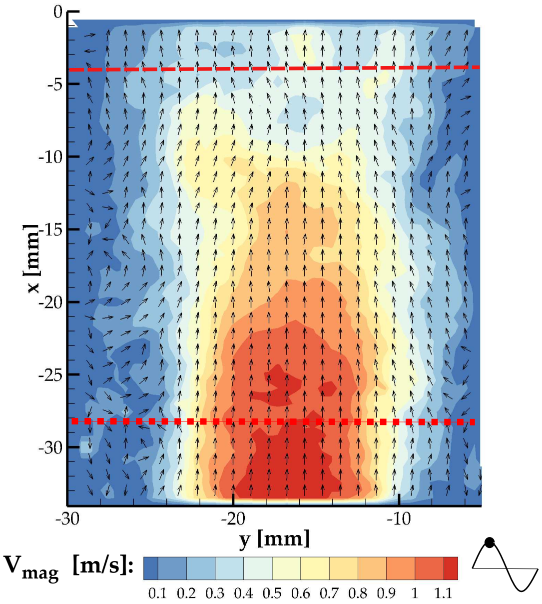


(A) Velocity magnitude of $Re_{max}$ = 2300 at $\frac{\pi}{2}$

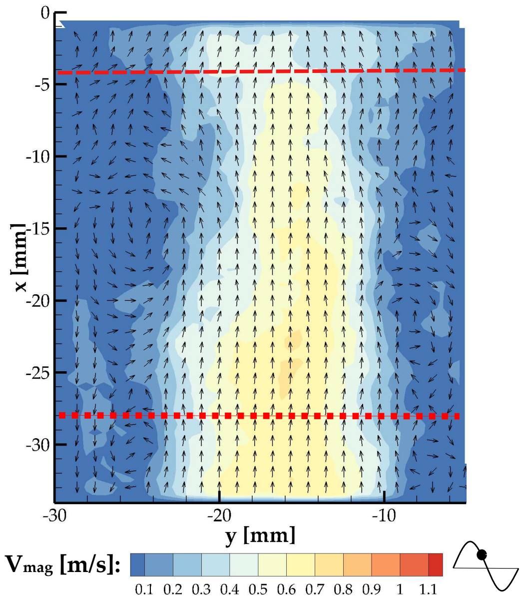


(B) Velocity magnitude of $Re_{max}$ = 2300 at $\frac{5\pi}{6}$

FIGURE 4.17: Velocity Magnitude of $Re_{max}$ = 2300 at $\frac{\pi}{2}$ and $\frac{5\pi}{6}$ in between 2D and 3D downstream. The dotted line corresponds to 2D downstream and the dashed line to 3D downstream.

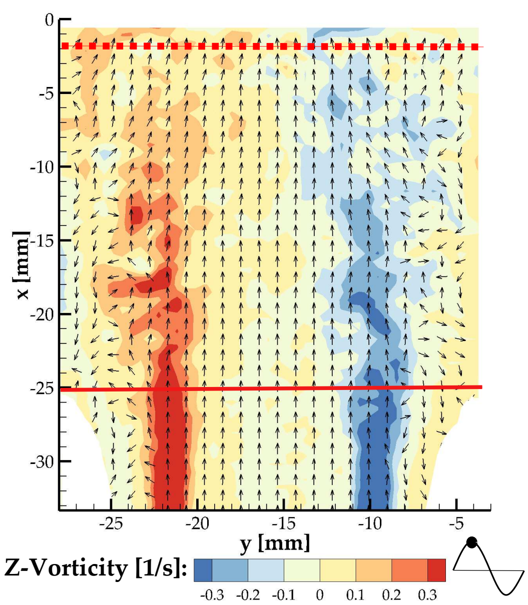


(A) Vorticity of $Re_{max}$ = 2300 at $\frac{\pi}{2}$

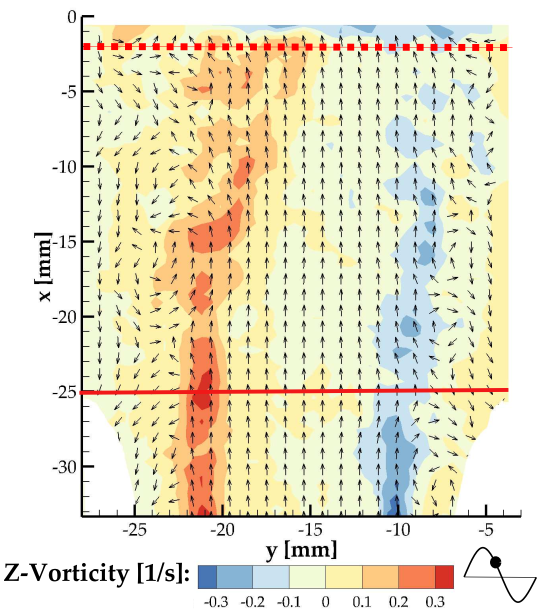


(B) Vorticity of $Re_{max}$ = 2300 at $\frac{5\pi}{6}$

FIGURE 4.18: Vorticity of $Re_{max}$ = 2300 at $\frac{\pi}{2}$ and $\frac{5\pi}{6}$ in between 1D and 2D downstream of the stenosis. The solid line corresponds to 1D downstream and the dotted line to 2D downstream.

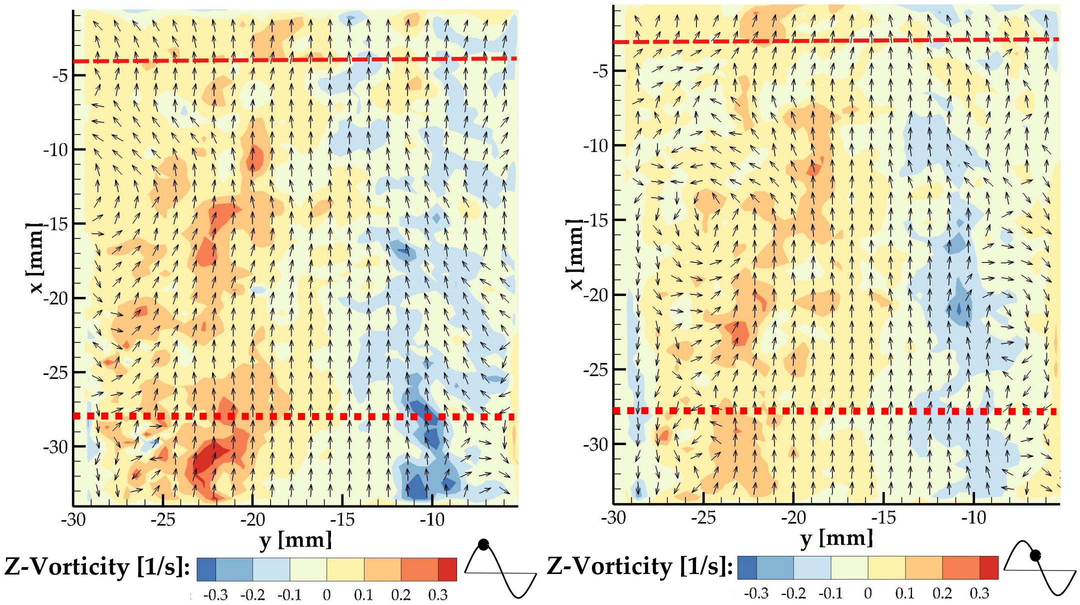


(A) Vorticity of $Re_{max}$ = 2300 at $\frac{\pi}{2}$ (B) Vorticity of $Re_{max}$ = 2300 at $\frac{5\pi}{6}$.

FIGURE 4.19: Vorticity of $Re_{max}$ = 2300 at $\frac{5\pi}{6}$ in between 2D and 3D downstream. The dotted line corresponds to 2D downstream and the dashed line to 3D downstream.

### 4.3.4 Lowest Reynolds number

The physics of flow of one of the measurements, $Re_{max}$ = 500 in Table 4.1, were considerably different and are therefore discussed separately. In the other measurements the Reynolds number was higher, as the transition to the turbulent regime is one of the research topics. However, in this experiment at a lower Reynolds number there is no jet structure visible through the stenosis and the physical phenomena are different.

The velocity profile is shown in Figure 4.20. Just downstream of the stenosis throat, which corresponds to 1D downstream, the velocity in the middle of the phantom is positive, at every temporal location. In the core the fluid keeps moving forward, while near the walls the direction reverses in the backward flow. The velocity profile at 2D downstream is presented in Figure 4.20b, where it is clearly visible that the fluid moves forwards during the first half-cycle of the sine waveform, but moves in negative direction during the reversal phase.

The volumetric flow rate is displayed in Figure 4.21. The shape of the sine waveform is clearly visible in this measurement, as there is no jet formed downstream of the stenosis throat. This is in contrast to the other stenosed pipe experiments, which were discussed before. The forward and backward values for the volumetric rate are therefore approximately the same, as expected in this type of flow.

The axial centerline is plotted in Figure 4.22a for two different temporal locations, as there are big differences between those. In the deceleration phase of the forward flow, $\frac{5\pi}{6}$, the centerline velocity is positive at every x-location downstream of the stenosis. It accelerates just downstream of the stenosis, then it quickly decelerates after which the velocity remains constant along the x-location of the phantom. At $\frac{3\pi}{2}$, which is the peak backward flow, the velocity is positive in between 1D and approximately 1.6D. Further downstream the velocity decreases and the velocity component is negative. The centerline velocity over the first three cycles is plotted

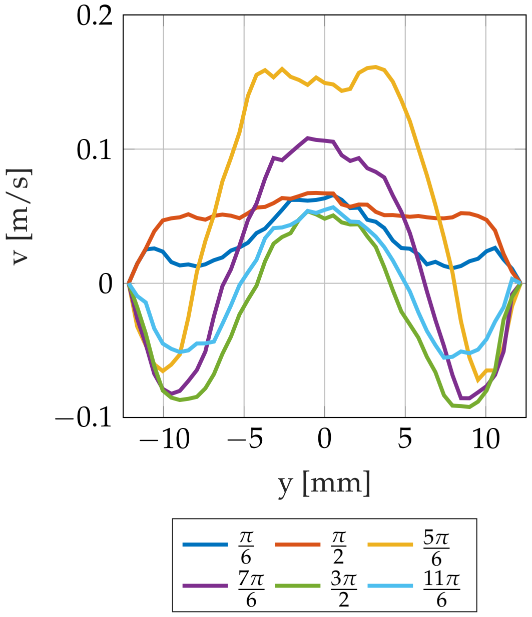


(A) Averaged velocity profile of $Re_{max}$ = 500 at 1D downstream

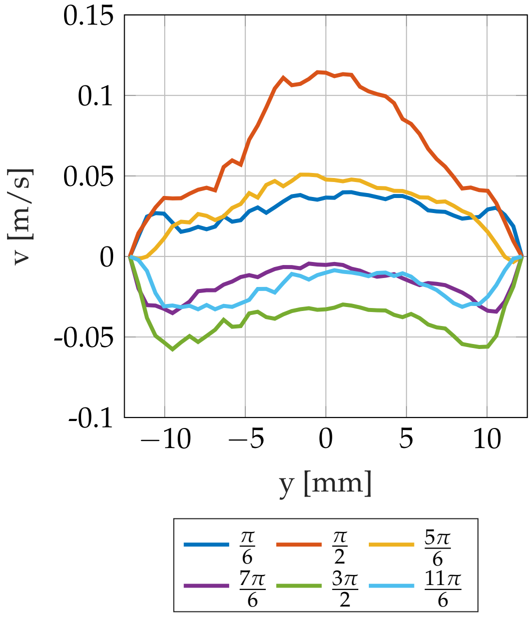


(B) Averaged velocity profile of $Re_{max}$ = 500 at 2D downstream

FIGURE 4.20: The averaged velocity profile of $Re_{max}$ = 500 averaged over 5 cycles at 1D and 2D downstream.

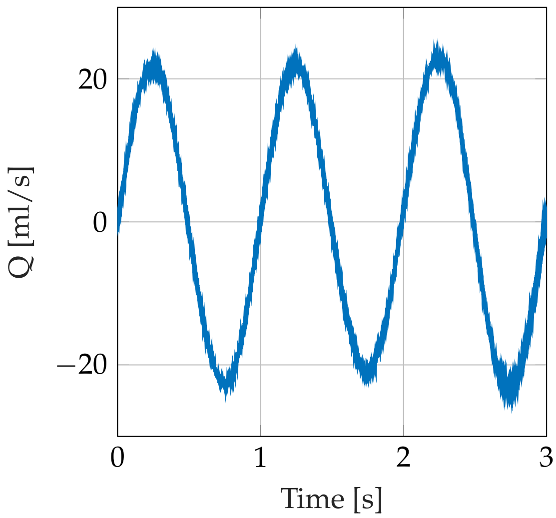


FIGURE 4.21: Volumetric flow rate of $Re_{max}$ = 500

in Figure 4.22b. The data is displayed for 1D and 2D downstream. Just downstream of the stenosis throat the velocity is positive at every instant of the cycle, as the fluid seems to be captured in a kind of "mushroom shape". At 2D downstream of the stenosis the velocity is negative in the backward phase of the fluid flow.

The contour plots of this experiment are displayed below, which include the velocity magnitude at four temporal locations of sine waveform and the vorticity. The velocity magnitude at $\frac{\pi}{2}$ is displayed in Figure 4.23a and the fluid moves forwards at every location in the phantom. At $\frac{5\pi}{6}$ a central core can be observed that moves forwards with some circulation near the walls of the phantom. At $\frac{7\pi}{6}$ and $\frac{3\pi}{2}$ the central core keeps moving forward, even though the rest of the fluid has reversed in direction and flows backwards. This phenomena is demonstrated in Figure 4.24.

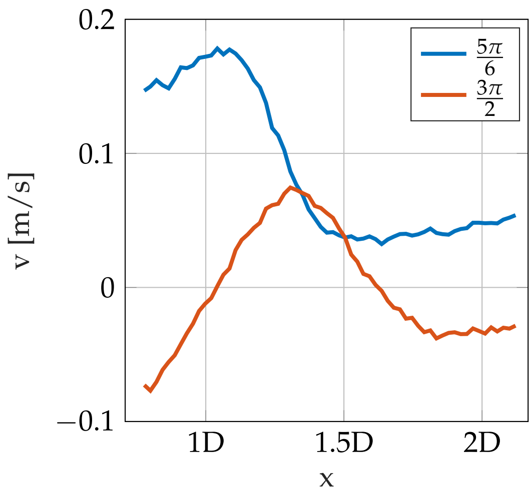


(A) Axial centerline velocity $Re_{max}$ = 500

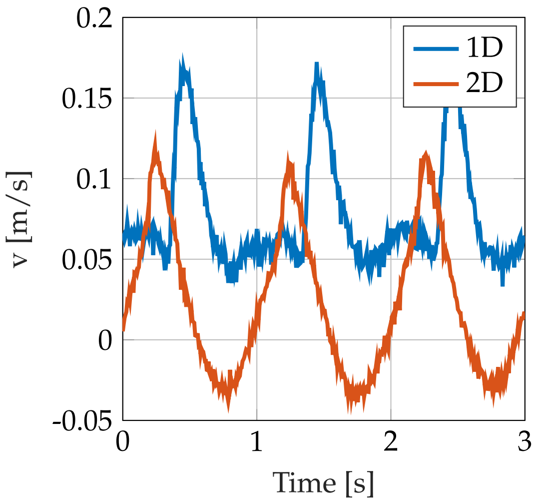


(B) Centerline velocity $Re_{max}$ = 500

FIGURE 4.22: Axial centerline velocity profile and centerline velocity profile of $Re_{max}$ = 500.

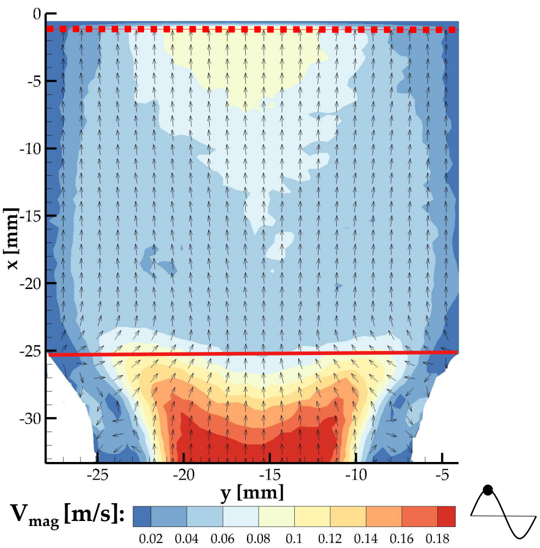


(A) Velocity magnitude of $Re_{max}$ = 500 at $\frac{\pi}{2}$

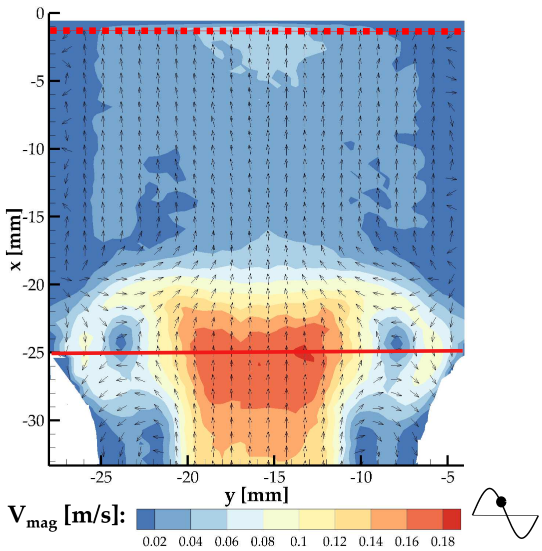


(B) Velocity magnitude of $Re_{max}$ = 500 at $\frac{5\pi}{6}$

FIGURE 4.23: Velocity magnitude of $Re_{max}$ = 500 at $\frac{\pi}{2}$ and $\frac{5\pi}{6}$ in between 1D and 2D downstream of the stenosis. The solid line corresponds to 1D downstream and the dotted line to 2D downstream.

The vorticity at $\frac{\pi}{2}$ and $\frac{5\pi}{6}$ is displayed in Figure 4.25. Here the vortex ring that is captured can be clearly recognized due to the vortices.

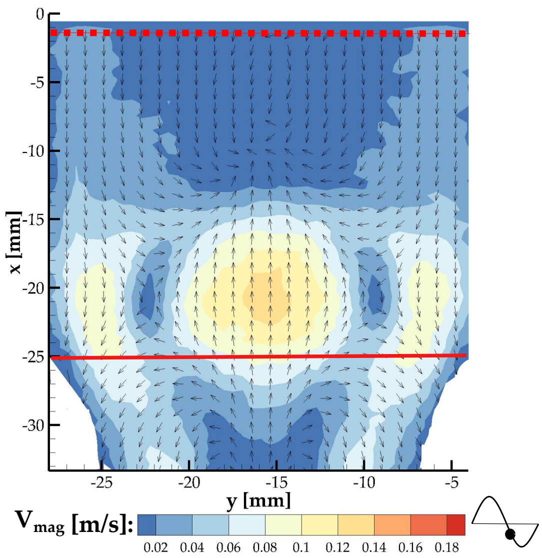


(A) Velocity magnitude of $Re_{max}$ = 500 at $\frac{7\pi}{6}$

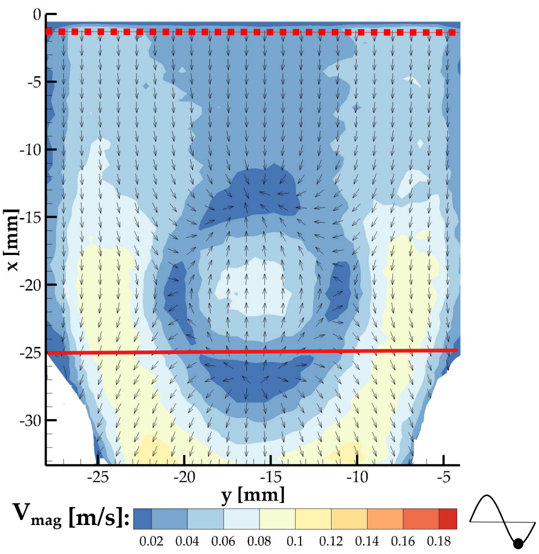


(B) Velocity magnitude of $Re_{max}$ = 500 at $\frac{3\pi}{2}$

FIGURE 4.24: Velocity magnitude of $Re_{max}$ = 500 at $\frac{7\pi}{6}$ and $\frac{3\pi}{2}$ in between 1D and 2D downstream of the stenosis. The solid line corresponds to 1D downstream and the dotted line to 2D downstream.

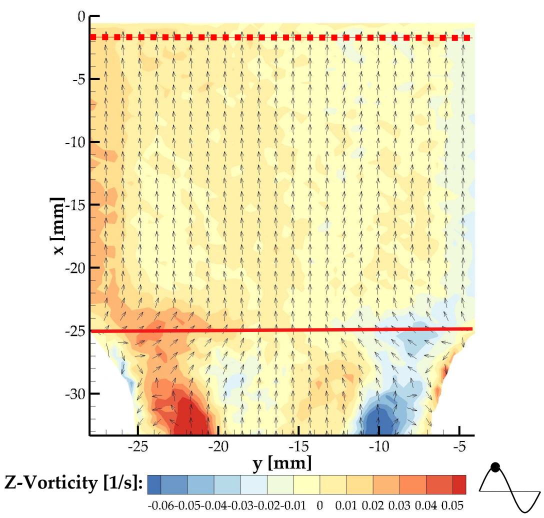


(A) Vorticity of $Re_{max}$ = 500 at $\frac{\pi}{2}$

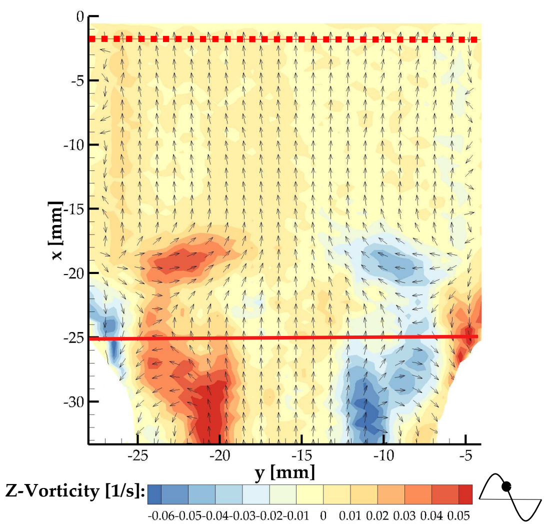


(B) Vorticity of $Re_{max}$ = 500 at $\frac{5\pi}{6}$

FIGURE 4.25: Vorticity of $Re_{max}$ = 500 at $\frac{\pi}{2}$ and $\frac{5\pi}{6}$ in between 1D and 2D downstream of the stenosis. The solid line corresponds to 1D downstream and the dotted line to 2D downstream.

### 4.3.5 Transition to turbulence

To further investigate if the flow phenomena seen are indeed signatures of the onset of turbulence or simply disturbances in a laminar flow regime, the power spectrum of the turbulent kinetic energy is plotted in Figure 4.26. The five different Reynolds numbers are displayed and the grey line represents the Kolmogorov $\frac{-5}{3}$ energy decay. If the decay of the plotted lines exhibited a slope parallel to $\frac{-5}{3}$ line then there would be more frequencies in the inertial subrange implying finite amount of turbulence in the flow. The transition is expected in the deceleration phase, $\frac{5\pi}{6}$, as mentioned in the previous sections.

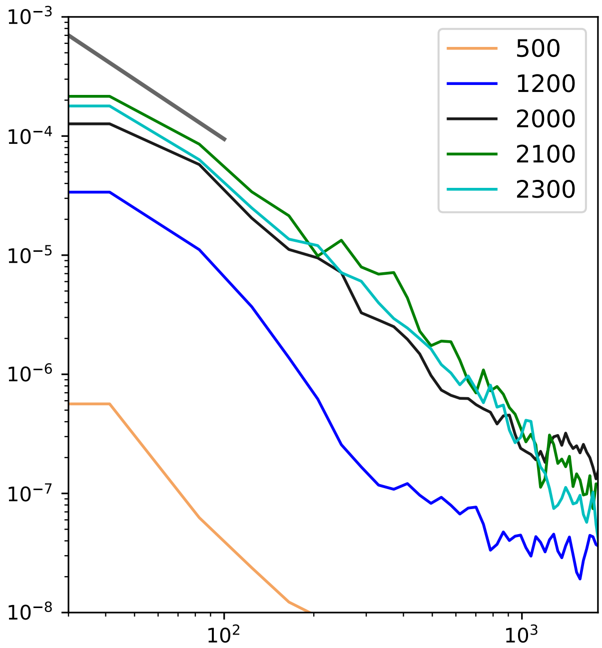


FIGURE 4.26: Power spectral density of the different Reynolds numbers. The -5/3 Kolmogorov decay line is represented by the grey line.

A clear difference can be noticed between the experiment with $Re_{max}$ = 500, which is expected to be fully laminar, and the higher Reynolds numbers, which show similarities to the Kolmogorov line. From the presented data it cannot be concluded whether the flow is transitional or not. There is no consensus on when to call a flow transitional, thus the terms non-laminar or transitional can be used. The frequency components, due to relatively small number of data points, cannot provide a conclusive insight into the regime of the flow. It is however clear that the flow at $Re_{max}$ = 2000 has left the laminar regime as the spectrum would have otherwise fallen immediately like the case of $Re_{max}$ = 500. Based on these observations, the flows at $Re_{max}$ > 2000 can be referred to as non-laminar.

## 4.4 Discussion

### 4.4.1 Summary of the results

- When analyzing the axial velocity profiles, it is clear that there are cycle to cycle variations. When plotting two different cycles, the velocity profile differs, especially further downstream the stenosis.

- The breakdown location of the jet has been analyzed by plotting the axial centerline velocity. The breakdown location depends on the Reynolds number and is in between 2D and 3D downstream. It shifts closer to the stenosis throat with increasing Reynolds number.
- The centerline velocity is plotted near the jet breakdown location and the velocity increases heavily around $\frac{\pi}{2}$ and $\frac{5\pi}{6}$. The width and peak value of the centerline velocity is larger with increasing $\mathrm{Re}_{max}$. During the deceleration phase, where the jet breaks down, there seems to be a transition to turbulence. The flow relaminarizes during the reversal and acceleration phase.
- The velocity magnitude and vorticity plots show a clear jet just downstream of the stenosis and recirculation zones around the jet breakdown location.
- Experiments at a $\mathrm{Re}_{max} = 500$ show completely different physical phenomena. A central core keeps slowly moving forward during the forward and backward phase of the cycle. A vortex ring is visible just downstream of the stenosis. Near the walls the direction of the fluid reverses during the backward phase, and it flows in the negative direction.
- Based on the power spectral density and above mentioned plots it is clear the flow has left the laminar regime, however it cannot be said conclusively if the flow is transitional or not due to the low amount of temporal data points. The experiments with $\mathrm{Re}_{max} > 2000$ can be referred to as non-laminar.

### 4.4.2 Comparison to previous research

Previously research has been conducted into oscillatory flow in a stenosed pipe, as discussed in Section 2.2. Jain [8] computationally investigated the onset of turbulence in oscillatory flow in a pipe with the same geometry. The results from this thesis are compared to his results and other previous studies into oscillatory flow and the transitional regime.

In this report different definitions of the Reynolds number have been used. Jain used $\mathrm{Re}_{avg}$ as definition of the Reynolds number, which is also displayed in Table 4.1 in this report.

The obtained axial velocity profiles in this research are slightly different than the obtained velocity profiles by Jain. One of the factors that differs in this research is the Womersley number. The value of $\alpha$ is 7.5 in research by Jain and 15.9 in this research. Thus leading to a flatter, more plug-like velocity profile in the results of this thesis. The flattened velocity profile is mostly visible during $\frac{5\pi}{6}$ in the forward phase and all the locations in the backward phase. The results from Jain show a steeper velocity profile [8], as expected at such a Womersley number (see Figure 2.5 for a comparison of the velocity profile at different Womersley numbers).

Jain used two different configurations, an axisymmetric and an eccentric stenosis geometry. Only the axisymmetric geometry was studied in this research. However, the axial velocity profiles in this research show similarities to the eccentric simulations from Jain. In the results of the eccentric geometry from Jain, the velocity profiles seem to be shifted closer to the stenosis throat than in his axisymmetric stenosis and a distortion is introduced in the axisymmetric velocity profile due to the offset in the stenosis. This is comparable with the velocity profiles in Figures 4.8a and 4.9. In these figures a deviation from the symmetric velocity profile is visible, which corresponds to the eccentric simulations from Jain. At 2D downstream in his axisymmetric geometry, the results show a symmetric velocity profile, which is not visible

in the results in this thesis. Even though a perfect axisymmetric geometry was used in the digital domain, slight inaccuracies were introduced while making the phantom and during the experiments. This will be further described in Section 4.4.3. In this thesis the data is averaged over five cycles, while the results from Jain are averaged over approximately 20 cycles. This can be an explanation of the difference in velocity profiles.
The obtained centerline velocities in this research seem to correspond with the eccentric centerline velocities by Jain. The flow seems to transition at $\pm$ 2D downstream in the axisymmetric geometry in this thesis for most Reynolds numbers. In the simulations from Jain the flow seemed to transition at 2D downstream for the eccentric case and 3D downstream for the axisymmetric case. In this research, only a frequency of 1 Hz has been used, thus the influence of the varying frequency is not investigated and cannot be compared.

As described in the theory section, Samuelsson et al. [56] confirmed that the introduction of a slight eccentricity (0.3% of the pipe diameter) can strongly decrease the Reynolds number at which the flow becomes unstable. This is an important finding as slight inaccuracies in experimental models are inevitable, while numerical models can be perfectly symmetrical. Thus, it is more likely to observe a transition to turbulence in experiments, as the critical Reynolds number is lowered due to asymmetries in the model. This can explain why the results of the experiments are similar to those of the simulations, while the Reynolds number is lower. The highest obtained $Re_{avg}$ is approximately 1800 in the experiments, while Jain described a transition in the axisymmetric geometry around $Re_{avg} = 2100$ and the eccentric geometry around $Re_{avg} = 1800$ [8]. Hino et al [45] concluded that the transition to weakly turbulent flow occurs at a lower Reynolds number as the Womersley number increases. As the Womersley number in this project is higher than in the simulations of Jain [8], this can influence the critical Reynolds number.

The different stages in the cycle are as described by Jain [8], Ahmed & Giddens [54] and Varghese et al.[55]. The transition seems to occur during the deceleration phase, while during the reversal and acceleration phase the flow relaminarizes. These results are confirmed by this study, as the same phenomena are observed.

The finding by Samuelsson et al. and the results in this thesis can explain why in the research of Helgeland et al. [9] and Jain et al. [6] a transition to turbulence was observed. The complex geometry of the SAS can lead to locally higher Reynolds numbers and the critical threshold can be lowered due to the constrictions. Even though the generally accepted threshold is higher, the imperfect conditions, as displayed in these experiments, lead to different results and flow phenomena than expected.

### 4.4.3 Limitations of experiments

There are several limitations to the performed experiments. They are discussed below and require further attention in future experiments:

- An axisymmetric velocity profile is assumed while calculating the volumetric profile. This is valid for purely laminar flow in Chapter 3, however in this chapter this is no longer valid due to the locally increased velocities due to the jet and the possible transition to turbulence. There is a cycle to cycle variation of the velocity profile and thus another method should be applied to calculate the volumetric flow rate. Either 3D PIV could be used, to obtain a 3D velocity profile and then compute the volumetric flow rate, or measure the velocity profile further downstream the stenosis throat, where the flow has relaminarized and the method is valid.

- Another method to accurately determine the axial location downstream of the stenosis should be introduced. As the ROI was too large to capture in a single image, two different FOV are used. An overlap of 25% is introduced, to fully capture the desired data. This leads to an inaccuracy as the locations further downstream cannot be determined precisely and the overlap of 25% might slightly differ. Currently the locations are marked on the phantom with a pencil, based on the view of the camera. The locations 1D and 2D are very precise, as they are based on the end of the stenosis throat, but the location 3D downstream is approximate and can be slightly different in reality. By using another lens, or zooming out, a larger part of the phantom can be captured, and thus more locations up- and - downstream of the stenosis can be accurately captured. However, zooming out will cause a loss of resolution. Therefore, a tradeoff has to be made between spatial resolution of the obtained data, and the ROI of the stenosed phantom.

- As described in Chapter 3, the walls of the straight phantom seemed to pulsate heavily (see Table 3.9), therefore the stenosed phantom was designed with phantom walls that are approximately twice as thick. However, during the measurements with the stenosed phantom, the pulsating motion of the phantom was clearly visible, especially at higher Reynolds numbers. Therefore a second analysis of the deformation of phantom was performed. The quantified deformation of the phantom is presented in Table 4.2. At the lowest Reynolds number, $Re_{max}$ = 500 there is no deformation noticeable in the raw data. At increasing Reynolds number, the deformation of the phantom walls increases. Furthermore, the deformation of the phantom seems to increase further downstream of the stenosis. At 1D downstream of the stenosis, there is a jet structure which leads to a lower deformation, while the deformation is the highest in between 2D and 3D downstream, where the jet breaks down. The vortices can lead to an increase of the forces exerted on the walls of the phantom. This can explain the increase in the deformation compared to the results in the straight phantom, where no vortices were visible and the flow seemed laminar.

  During the analysis of the deformation it was not possible to accurately determine any differences between both sides of the phantom, therefore it was assumed that the deformation at $y/D$ = -0.5 and $y/D$ = 0.5 are equal. Only the deformation along the y-axis was visible and not the z-axis, as a 2D PIV method is used.

  The FOV of the recorded data was placed downstream of the stenosis throat, to capture the locations with the most interesting flow phenomena. Therefore the deformation at the stenosis throat could not be analyzed. Any deformations here can lead to the introduction of an eccentricity in the stenosis geometry. As described in the previous section and in the studies from Samuelsson et al. [56], a 0.3% offset of the pipe diameter can already strongly decrease the critical Reynolds number and influence the physics of flow. This could explain the similarities to the eccentric stenosis simulations by Jain [8].

- The temporal resolution of the PIV data was not sufficient to draw any conclusions from the power spectral density. Therefore it is not fully clear whether the flow is in the transitional phase. However, based on the results it is clear that it is no longer in the laminar regime. By using other experimental techniques, such as Laser Doppler Anemometry (LDA), a higher temporal resolution can be obtained. This can provide more insights in the flow characteristics and the exact (turbulent) flow regime. For more information regarding other experimental techniques, the reader is referred to Tropea et al. [59].

| **Re**$_{max}$ | **Location [x/D]** | **Original diameter [px]** | **Deformation [px]** | **Deformation [%]** |
|---|---|---|---|---|
| 1200 | 1 | 725 | 8 | 1.1 |
| | 2 | 725 | 8 | 1.1 |
| | 3 | 725 | 12 | 1.7 |
| 2000 | 1 | 725 | 20 | 2.8 |
| | 2 | 725 | 32 | 4.4 |
| | 3 | 725 | 48 | 6.6 |
| 2300 | 1 | 725 | 32 | 4.4 |
| | 2 | 725 | 60 | 8.3 |
| | 3 | 725 | 68 | 9.4 |

TABLE 4.2: Overview of the deformation of the stenosed phantom

### 4.4.4 Physiological aspects for improvements of the experiments

This research was conducted to better understand the oscillatory flow through a stenosis, which is relevant for the flow of CSF. As the flow conditions of CSF are very complicated, it has been simplified to a sine waveform and an axisymmetric stenosis of 75%. In this section several points of discussion will be presented which will make the experiments more realistic.

- The CSF in the body moves through the SAS in the brain and down the spinal cord. The movement of the fluid in these locations is different due to the different anatomical conditions [34] [96]. In the cranial subdural space, in the brain, the dura is attached to the bone and can therefore not expand or contract. While the spinal dura is separated from the bone and located near soft tissue and the volume can change. Thus, depending on the desired location in the body, a more rigid or flexible phantom should be used to perform the experiments. Furthermore, Oreskovic et al. investigated that the position of the body is of influence of the CSF flow. [34]. More research into the flexibility and positioning of the phantom can improve the results.

- The flow of CSF is driven by several factors, of which the arterial pulsation is the main factor. Respiration rate also influences the flow, as described in Section 2.1, and pathological conditions can strongly affect the CSF movement. In this research the inlet waveform is a pure sine waveform, which is a simplified version of the real life movement of CSF. Thomas [15] described that the wall wave movement, which is the main driver of CSF, is not sinusoidal, but a fast expansion followed by a slow contraction. This will lead to different fluid speeds and different flow phenomena. Furthermore, the frequency will not be constant and other distortions might occur during the cycle. Distortions of the inlet waveform can introduce instabilities and influence the flow phenomena and the moment of transition. Mestre et al. [32] investigated the flow of CSF through the PVS and the influence of different mechanisms, such as arterial pulsations and the pathological conditions. By modelling a more realistic waveform, including distortions and no constant pulsation frequency, the conditions are more similar to the actual physiological conditions in the body.

- Currently an axisymmetric stenosis of 75% is used as a model, as this is a relevant geometry for constricted locations in the body. However, the SAS has a very complex geometry, including varying diameters, narrow passages and a tortuous geometry. The introduction of the stenosis, and the eccentricity of it, have an influence on the flow phenomena and the moment of transition. Helgeland et al. [9] found the onset of turbulence at a considerably lower Reynolds number, which was based on the real geometry of the SAS of a patient with CMI. Therefore it is interesting to also include the eccentric stenosis and even other, more complicated geometries that are more realistic given the shape of the SAS.

These modifications to either the phantom or the performed experiments will have an influence on the flow characteristics and the moment of transition. Although, the exact influence of these factors is unknown, it is expected that a more complex geometry and varying waveform will lower the Reynolds number at which the flow transitions to turbulence. However, more research in this area is required before any conclusions can be drawn, as the current research purely focused on the in vitro experiments with a sine waveform and an axisymmetric stenosis.

## 4.5 Conclusion

A phantom with an axisymmetric stenosis of 75% has been produced and experiments at different Reynolds numbers performed. The breakdown location of the jet formed downstream of the stenosis is in between 2D and 3D downstream and it shifts closer to the stenosis throat with increasing Reynolds number. During the deceleration phase, where the jet breaks down, there seems to be a transition to turbulence. The flow relaminarizes during the reversal and acceleration phase. Experiments at a $Re_{max}$ = 500 show completely different physical phenomena. A central core keeps slowly moving forward during the forward and backward phase of the cycle and a vortex ring is visible just downstream of the stenosis. Based on the power spectral density it is clear the flow at $Re_{max}$ > 2000 has left the laminar regime, however it cannot be said conclusively if the flow is transitional due to the low amount of temporal data points.

The introduction of slight inaccuracies in the geometry of the stenosis shifts the breakdown location closer to the stenosis throat than expected based on numerical simulations of an axisymmetric stenosis. These inaccuracies were introduced during the production of the phantom and due to the pulsating motion of the phantom walls during the experiments. Several improvements were suggested which include modifications to the PIV setup and including other physiological effects of CSF. Although this research is in an initial stage, the results are promising and show perspective for future experiments.

# Chapter 5

# General conclusion and recommendations

The final goal of this thesis was to experimentally study the fluid dynamics of CSF in a stenosis. Chapter 3 provided the foundation to perform these experiments, by creating a setup that is representative for the flow of CSF. Chapter 4 describes how this setup has been used to study the flow characteristics and the transition to the turbulent regime in an axisymmetric stenosis of 75%. In this chapter the results of the thesis are discussed and perspectives for future research are presented

### Flow setup

The Vivitro pump is able to generate a sine waveform and it has been verified that the Bronkhorst Coriolis flow sensor can measure bidirectional flows. The introduction of the Sonotec Ultrasound flow sensor reduced the resistance in the flow circuit, but the accuracy is decreased at low flow rates. Further research into the performance of the Sonotec Ultrasound flow sensor is recommended, to gain better control over the measurements. Furthermore, the backward flow of the Vivitro pump seems to be less accurate than the forward flow. It is not likely that it is due to the momentum of the fluid, as the peak value of the backwards phase is shifted to the left. This topic can be addressed in future research by investigating different waveform types, velocities and fluids to investigate which variables influence the performance of the Vivitro.

As the experiments are performed at high Reynolds numbers the required entrance length to ensure fully developed flow is significantly increased. As the required entrance length exceeds the practical limits of the lab, straw holders were designed to reduce the entrance length. Two different straws, which vary in shape and length, have been used and the results were compared. The long straws seem to perform better, however there are too many uncertainties to draw any definitive conclusions. There is a knowledge gap on fully developed flows, especially in pulsatile and oscillatory flows, as this issue is not regularly addressed in research. By conducting further research, the entrance length for different types of flow can be determined and the influence of the straws quantified. Based on these results the straws can be improved, omitted or replaced in future experiments.

In the optimized setup it is feasible to generate flows in a straight pipe phantom with a sine waveform and a $Re_{max}$ of approximately 2200. No signs of turbulence are observed at this $Re_{max}$ or during the experiments at lower Reynolds numbers. The $Re_{max}$ is too low or there is lack of a disturbance, which can be a distorted waveform or geometry, and thus turbulence is not yet triggered in the flow.

### PIV setup

Laser PIV techniques are used to obtain the velocity profiles. Even though the results seem accurate and correspond well with the obtained profiles of the flow sensors, certain improvements can be made. During the analysis of the PIV data of the straw experiment, it was observed that the quality of the PIV data was not consistent. There are two main sources of error in PIV that determine the quality of a measurement, the bias error and the random error[59]. By using synthetic particle images, these two errors can be quantified. These results give an estimation of the accuracy of the PIV method. More details regarding these techniques are described by Thielicke [67]. As the phantom deforms during the measurements due to the motion of the flow, dynamic masking can be used to apply the correct mask and calibration at every frame.

In the current setup it is not possible to capture the whole stenosed phantom in the FOV. By zooming out or using another lens a larger part of the phantom can be captured in the FOV. This will lead to a more accurate result of the spatial locations and more information up- and downstream of the stenosis but a decrease in spatial resolution.

By using other PIV techniques all of the components of the velocity gradient tensor can be determined, which decreases the error in the u- and v-component and provides information on the z-component. This would be optimal to fully capture the (turbulent) velocity field and offers more insights into the flow dynamics. Options to capture more velocity data are Stereoscopic PIV, Tomographic PIV and scanning PIV. Stereoscopic PIV uses two cameras at different angles to to extract the z-component and Tomographic PIV needs at four cameras to reconstruct the 3D velocity field. Scanning PIV uses a rotating mirror and by illuminating different planes in the flow, the properties of the flow can be interpolated over the different levels. If scanning PIV is combined with stereoscopic PIV, it can approximate the 3D analysis with 2D techniques [63]. This would be a more feasible option than Tomographic PIV, which would require an even more advanced setup.

### Stenosed experiments

A phantom with an axisymmetric stenosis of 75% was designed and produced to study the fluid dynamics of oscillatory flow in a stenosis. The designed flow setup is used to generate a sine waveform and the flow characteristics are analyzed. A jet is formed downstream of the stenosis throat, which seems to break down in between 2D and 3D downstream of the stenosis throat. The centerline velocities show increased values during the deceleration phase and the flow relaminarizes during the reversal and acceleration phase. The breakdown location shifts closer to the stenosis throat and the width and peak values of the centerline velocity are higher with increasing $Re_{max}$. Unexpected results appeared at the experiments performed at a $Re_{max}$ of 500, where there is a vortex ring just downstream of the stenosis throat instead of a jet that breaks down. As there is no literature on this phenomena in this specific geometry or flow conditions, it is recommended to study the flow dynamics through this stenosis at lower Reynolds numbers. This research direction seems underexposed, while the flow dynamics can be physiologically relevant.

Based on the power spectral density it cannot be said conclusively if the flows are transitional, due to the low temporal resolution. However, based on the results it is clear that the flows at $Re_{max} > 2000$ are non-laminar.

The results have been compared to numerical studies from Jain [8], where he investigated oscillatory flow in the same geometry. He observed jet breakdown locations and increased centerline velocities further downstream of the stenosis. The differences could be explained by non-perfect conditions in the experiments, due to inevitably introduced imperfections in the geometry of the phantom. The phantom pulsated heavily during the experiments which can distort the perfect axisymmetrical geometry and thus lower the critical Reynolds number.

The current experiments have been performed to represent a simplified version of the flow of CSF. A sine waveform has been implemented in this research, but in reality a more complicated waveform, due to arterial pulsation and respiration, is the main driver of CSF movement. The geometry is a simple, but anatomically relevant, model to study the flow of CSF. However, the geometry of the SAS and accompanying anatomical conditions further complicate the flow phenomena. More complex geometries that are tortuous, eccentric or flexible phantoms can be studied to approach the real conditions of CSF in the body. These modified conditions will further alter the critical Reynolds number. Although the exact influence is unknown and should be investigated, it is expected that the Reynolds number at which a transition is observed will be decreased.

This thesis lays the groundwork for further research into oscillatory flows and in the future these types of experiments can be used to verify computational methods. Studies into CSF flow in the human body observed physical phenomena that are still poorly understood, but experiments can provide more insights. The theoretically low Reynolds numbers at which Helgeland et al. [9] and Jain et al. [6] observed transition to turbulence in CSF flow do not seem illogical based on the achieved results in this thesis.

In addition to the studies into oscillatory flow in stenosed pipes, the setup built in this thesis opens doors for future research into fully developed (oscillatory) flow and the transition to turbulence in straight pipe flows. Advancements in these research areas can further increase the understanding of oscillatory flow in stenosed pipes and its transition to turbulence. When the flow dynamics of CSF are better understood, its influence on neurological conditions can be studied and improved treatment methods can be developed.

# Bibliography


[1] R. Spector et al. "A balanced view of the cerebrospinal fluid composition and functions: Focus on adult humans". In: *Experimental Neurology* 273 (2015), pp. 57–68. ISSN: 10902430. DOI: 10.1016/j.expneurol.2015.07.027. URL: http://dx.doi.org/10.1016/j.expneurol.2015.07.027.

[2] J. Iliff et al. "A paravascular pathway facilitates CSF flow through the brain parenchyma and the clearance of interstitial solutes, including amyloid $\beta$". In: *Science Translational Medicine* 4.147 (2012). ISSN: 19466234. DOI: 10.1126/scitranslmed.3003748.

[3] D. Selkoe. "The amyloid hypothesis of Alzheimer's disease at 25 years". In: 8.(eds.), Berlin, Fed. Rep. Germany, Springer-Verlag, 1982, Session 2, p.41-52. (ISBN 3-540-12156-0) (2006), pp. 595–608.

[4] N.K. Kwong et al. "Defining novel functions for cerebrospinal fluid in ALS pathophysiology". In: *Acta Neuropathologica Communications* 8.1 (2020), pp. 1–18. ISSN: 20515960. DOI: 10.1186/s40478-020-01018-0. URL: https://doi.org/10.1186/s40478-020-01018-0.

[5] K. Jain. *Transition to Turbulence in Physiological Flows: Direct Numerical Simulation of Hemodynamics in Intracranial Aneurysms and Cerebrospinal Fluid Hydrodynamics in the Spinal Canal*. 2016. ISBN: 9783936533835. DOI: 10.1007/springerreference_67856.

[6] K. Jain et al. "Direct numerical simulation of transitional hydrodynamics of the cerebrospinal fluid in Chiari I malformation: The role of cranio-vertebral junction". In: *International Journal for Numerical Methods in Biomedical Engineering* 33.9 (2017), pp. 1–15. ISSN: 20407947. DOI: 10.1002/cnm.2853.

[7] T.H. Milhorat et al. "Chiari I malformation redefined: Clinical and radiographic findings for 364 symptomatic patients". In: *Neurosurgery* 44.5 (1999), pp. 1005–1017. ISSN: 0148396X. DOI: 10.1097/00006123-199905000-00042.

[8] K. Jain. "Transition to turbulence in an oscillatory flow through stenosis". In: *Biomechanics and Modeling in Mechanobiology* 19.1 (2020), pp. 113–131. ISSN: 16177940. DOI: 10.1007/s10237-019-01199-1.

[9] A. Helgeland et al. "Numerical simulations of the pulsating flow of cerebrospinal fluid flow in the cervical spinal canal of a Chiari patient". In: *Journal of Biomechanics* 47.5 (2014), pp. 1082–1090. ISSN: 18732380. DOI: 10.1016/j.jbiomech.2013.12.023.

[10] A. Orts-Del'Immagine and C. Wyart. "Cerebrospinal-fluid-contacting neurons". In: *Current Biology* 27.22 (2017), R1198–R1200. ISSN: 09609822. DOI: 10.1016/j.cub.2017.09.017. URL: http://dx.doi.org/10.1016/j.cub.2017.09.017.

[11] *Anatomy and Physiology, OpenStax*. Accessed: 29-09-2020. 2020. URL: https://openstax.org/books/anatomy-and-physiology/pages/13-3-circulation-and-the-central-nervous-system.

[12] *Meninges.* Accessed: 14-10-2020. 2011. URL: `https://biology-forums.com/index.php?action=gallery;sa=view;id=1142`.

[13] W.F. Boron and E.L. Boulpaep. *Medical Physiology 2nd Edition Updated Edition*. 2011.

[14] B. Wright et al. "Cerebrospinal fluid and lumbar puncture: A practical review". In: *Journal of Neurology* 259.8 (2012), pp. 1530–1545. ISSN: 03405354. DOI: `10.1007/s00415-012-6413-x`.

[15] J. H. Thomas. "Fluid dynamics of cerebrospinal fluid flow in perivascular spaces". In: *Journal of the Royal Society Interface* 16.159 (2019). ISSN: 17425662. DOI: `10.1098/rsif.2019.0572`.

[16] L. Sakka et al. "Anatomy and physiology of cerebrospinal fluid". In: *European Annals of Otorhinolaryngology, Head and Neck Diseases* 128.6 (2011), pp. 309–316. ISSN: 1879730X. DOI: `10.1016/j.anorl.2011.03.002`. URL: `http://dx.doi.org/10.1016/j.anorl.2011.03.002`.

[17] R. Di Terlizzi and S. Platt. "The function, composition and analysis of cerebrospinal fluid in companion animals: Part I - Function and composition". In: *Veterinary Journal* 172.3 (2006), pp. 422–431. ISSN: 10900233. DOI: `10.1016/j.tvjl.2005.07.021`.

[18] H. Cushing. "Studies in Intracranial Physiology & Surgery: The Third Circulation, the Hypophysics, the Gliomaso Title". In: *H. Milford, Oxford University Press* (1926).

[19] S. Friese et al. "The Influence of Pulse and Respiration on Spinal Cerebrospinal Fluid Pulsation". In: *Investigative Radiology* 39.2 (2004), pp. 120–130. ISSN: 00209996. DOI: `10.1097/01.rli.0000112089.66448.bd`.

[20] B. Williams. "On the pathogenesis of syringomyelia: a review". In: *Journal of the Royal Society of Medicine* 73.11 (1980), pp. 798–806. ISSN: 01410768. DOI: `10.1177/014107688007301109`.

[21] W. J. Gardner. "Hydrodynamic factors in Dandy Walker and Arnold Chiari malformations". In: *Child's Brain* (1977). ISSN: 03022803. DOI: `10.1159/000119669`.

[22] S. G. McClugage and J.W. Oakes. "The Chiari I malformation". In: *Journal of Neurosurgery: Pediatrics* 24.3 (2019), pp. 217–226. ISSN: 19330715. DOI: `10.3171/2019.5.PEDS18382`.

[23] CNS Neurosurgery. *Dr Khurana – Chiari Malformation image*. Accessed: 14-10-2020. 2020. URL: `https://www.cnsneurosurgery.com.au/arnold-chiari-type-i-malformation/dr-khurana-chiari-malformation-image/`.

[24] A. Thompson et al. "The Cervical spinal canal tapers differently in patients with Chiari i with and without syringomyelia". In: *American Journal of Neuroradiology* 37.4 (2016), pp. 755–758. ISSN: 1936959X. DOI: `10.3174/ajnr.A4597`.

[25] B. A. Martin et al. "Spinal subarachnoid space pressure measurements in an in vitro spinal stenosis model: Implications on syringomyelia theories". In: *Journal of Biomechanical Engineering* 132.11 (2010). ISSN: 01480731. DOI: `10.1115/1.4000089`.

[26] A. Linninger et al. "Pulsatile cerebrospinal fluid dynamics in the human brain". In: *IEEE Transactions on Biomedical Engineering* 52.4 (2005), pp. 557–565. ISSN: 00189294. DOI: `10.1109/TBME.2005.844021`.

[27] T. Brinker et al. “A new look at cerebrospinal fluid circulation”. In: *Fluids and Barriers of the CNS* 11.1 (2014), pp. 1–16. ISSN: 20458118. DOI: 10.1186/2045-8118-11-10.

[28] G. Mantovani et al. “Controversies and Misconceptions Related to Cerebrospinal Fluid Circulation: A Review of the Literature from the Historical Pioneers’ Theories to Current Models”. In: *BioMed Research International* 2018.Figure 1 (2018). ISSN: 23146141. DOI: 10.1155/2018/2928378.

[29] D. Orešković and M. Klarica. “The formation of cerebrospinal fluid: Nearly a hundred years of interpretations and misinterpretations”. In: *Brain Research Reviews* 64.2 (2010), pp. 241–262. ISSN: 01650173. DOI: 10.1016/j.brainresrev.2010.04.006.

[30] D. Orešković and M. Klarica. “A new look at cerebrospinal fluid movement”. In: *Fluids and Barriers of the CNS* 11.1 (2014), pp. 1–16. ISSN: 20458118. DOI: 10.1186/2045-8118-11-16.

[31] P. Hadaczek et al. “The "Perivascular Pump" Driven by Arterial Pulsation Is a Powerful Mechanism for the Distribution of Therapeutic Molecules within the Brain”. In: *Molecular Therapy* 14.1 (2006), pp. 69–78. ISSN: 15250016. DOI: 10.1016/j.ymthe.2006.02.018. URL: http://dx.doi.org/10.1016/j.ymthe.2006.02.018.

[32] H. Mestre et al. “Flow of cerebrospinal fluid is driven by arterial pulsations and is reduced in hypertension”. In: *Nature Communications* 9.1 (2018). ISSN: 20411723. DOI: 10.1038/s41467-018-07318-3. URL: http://dx.doi.org/10.1038/s41467-018-07318-3.

[33] A. Ladrón-de Guevara et al. “Perivascular pumping in the mouse brain: Realistic boundary conditions reconcile theory, simulation, and experiment”. In: arXiv:1707.Xx (2017). ISSN: 0027-8424. DOI: 10.1073/pnas.XXXXXXXXXX. arXiv: 1712.09707. URL: http://arxiv.org/abs/1712.09707.

[34] M. Klarica et al. “The influence of body position on cerebrospinal fluid pressure gradient and movement in cats with normal and impaired craniospinal communication”. In: *PLoS ONE* 9.4 (2014), pp. 1–11. ISSN: 19326203. DOI: 10.1371/journal.pone.0095229.

[35] G.N. Kouzehgarani et al. “Harnessing cerebrospinal fluid circulation for drug delivery to brain tissues”. In: *Advanced Drug Delivery Reviews* (2021). ISSN: 0169409X. DOI: 10.1016/j.addr.2021.03.002. URL: https://doi.org/10.1016/j.addr.2021.03.002.

[36] T. Khachatryan and J.S Robinson. “The possible impact of cervical stenosis on cephalad neuronal dysfunction”. In: *Medical Hypotheses* 118.June (2018), pp. 13–18. ISSN: 15322777. DOI: 10.1016/j.mehy.2018.06.008. URL: https://doi.org/10.1016/j.mehy.2018.06.008.

[37] S. El Sankari et al. “Cerebrospinal fluid and blood flow in mild cognitive impairment and Alzheimer’s disease: A differential diagnosis from idiopathic normal pressure hydrocephalus”. In: *Fluids and Barriers of the CNS* 8.1 (2011). ISSN: 20458118. DOI: 10.1186/2045-8118-8-12.

[38] L R. Sass et al. “Non-invasive MRI quantification of cerebrospinal fluid dynamics in amyotrophic lateral sclerosis patients”. In: *Fluids and Barriers of the CNS* 17.1 (2020), pp. 1–14. ISSN: 20458118. DOI: 10.1186/s12987-019-0164-3. URL: https://doi.org/10.1186/s12987-019-0164-3.

[39] K. Sato et al. "CSF flow dynamics in motor neuron disease". In: *Neurological Research* 34.5 (2012), pp. 512–517. ISSN: 01616412. DOI: 10.1179/1743132812Y.0000000043.

[40] J. R. Womersley. "Method for the calculation of velocity, rate of flow and viscous drag in arteries when the pressure gradient is known". In: *The Journal of Physiology* 127.3 (1955), pp. 553–563. ISSN: 14697793. DOI: 10.1113/jphysiol.1955.sp005276.

[41] H. Mirgolbabaee. "In-vitro studies on Womersley flow and microsphere ( Holmium-166 ) distribution in the liver vasculature using Laser PIV". In: (2019).

[42] F.N. van de Vosse. "Cardiovascular Fluid Mechanics lecture notes 8W090". In: (2009).

[43] O. Çarpinlioğlu and M. Gündoğdu. "A critical review on pulsatile pipe flow studies directing towards future research topics". In: *Flow Measurement and Instrumentation* 12.3 (2001), pp. 163–174. ISSN: 09555986. DOI: 10.1016/S0955-5986(01)00020-6.

[44] J. H. Gerrard and M. D. Hughes. "The flow due to an oscillating piston in a cylindrical tube: A comparison between experiment and a simple entrance flow theory". In: *Journal of Fluid Mechanics* 50.1 (1971), pp. 97–106. ISSN: 14697645. DOI: 10.1017/S0022112071002477.

[45] M. Hino et al. "Experiments on transition to turbulence in an oscillatory pipe flow". In: *Journal of Fluid Mechanics* 75.2 (1976), pp. 193–207. ISSN: 14697645. DOI: 10.1017/S0022112076000177.

[46] M. Hino et al. "Experiments on the turbulence statistics and the structure of a reciprocating oscillatory flow". In: *Journal of Fluid Mechanics* 131.HY8 (1983), pp. 363–400. ISSN: 14697645. DOI: 10.1017/S0022112083001378.

[47] M. Ohmi. "Transition to turbulenec in a pulsatile pipe flow part 2, characteristics of reversing flow accompanied by relaminarization". In: *Bulletin of the JSME* 25.208 (1992), pp. 1529–1536. URL: https://www.jstage.jst.go.jp/article/bpb1993/17/11/17_11_1460/_pdf/-char/ja.

[48] D. Xu et al. "Transition to turbulence in pulsating pipe flow". In: *Journal of Fluid Mechanics* 831 (2017), pp. 418–432. ISSN: 14697645. DOI: 10.1017/jfm.2017.620. arXiv: 1709.03738.

[49] D. Feldmann, D. Morón, and M. Avila. "Spatiotemporal intermittency in pulsatile pipe flow". In: *Entropy* 23.1 (2021), pp. 1–19. ISSN: 10994300. DOI: 10.3390/e23010046.

[50] D. Xu et al. "Nonlinear hydrodynamic instability and turbulence in pulsatile flow". In: *Proceedings of the National Academy of Sciences of the United States of America* 117.21 (2020), pp. 1–7. ISSN: 10916490. DOI: 10.1073/pnas.1913716117.

[51] D. Xu, B. Song, and M. Avila. "Non-modal transient growth of disturbances in pulsatile and oscillatory pipe flows". In: *Journal of Fluid Mechanics* 0 (2020), pp. 1–10. ISSN: 14697645. DOI: 10.1017/jfm.2020.940. arXiv: 2008.04616.

[52] J. Gomez, Huidan Yu, and Yiannis Andreopoulos. "Role of flow reversals in transition to turbulence and relaminarization of pulsatile flows". In: (2021), pp. 1–42. DOI: 10.1017/jfm.2021.269.

[53] N. Barrere et al. "Vortex dynamics under pulsatile flow in axisymmetric constricted tubes". In: *Papers in Physics* 12 (2020), p. 120002. ISSN: 1852-4249. DOI: 10.4279/pip.120002. arXiv: 1904.10547.

[54] S.A. Ahmed and D.P. Giddens. "Pulsatile poststenotic flow studies with laser Doppler anemometry". In: *Journal of Biomechanics* 17.9 (1984), pp. 695–705. ISSN: 00219290. DOI: 10.1016/0021-9290(84)90123-4.

[55] S.S. Varghese, Steven H. Frankel, and Paul F. Fischer. *Direct numerical simulation of stenotic flows. Part 2. Pulsatile flow*. Vol. 582. July. 2007, pp. 281–318. ISBN: 0022112007005. DOI: 10.1017/S0022112007005836.

[56] J. Samuelsson et al. "Breaking axi-symmetry in stenotic flow lowers the critical transition Reynolds number". In: *Physics of Fluids* 27.10 (2015). ISSN: 10897666. DOI: 10.1063/1.4934530. URL: http://dx.doi.org/10.1063/1.4934530.

[57] K. Jain. "Efficacy of the FDA nozzle benchmark and the lattice Boltzmann method for the analysis of biomedical flows in transitional regime". In: *Medical and Biological Engineering and Computing* 58.8 (2020), pp. 1817–1830. ISSN: 17410444. DOI: 10.1007/s11517-020-02188-8. arXiv: 2005.07119.

[58] A. Trigui et al. "Experimental and numerical investigation of pulsed flows in asevere aortic stenosed model". In: *Medical Engineering and Physics* 90 (2021), pp. 33–42. ISSN: 18734030. DOI: 10.1016/j.medengphy.2021.02.006. URL: https://doi.org/10.1016/j.medengphy.2021.02.006.

[59] C. Tropea et al. *Springer Handbook of Experimental Fluid Mechanics*. Vol. 91. 5. 2012, pp. 1689–1699. ISBN: 9788578110796. DOI: 10.1017/CBO9781107415324.004. arXiv: arXiv:1011.1669v3.

[60] DLR. *Warum Vögel flattern, Flugzeuge aber besser nicht*. Accessed: 15-02-2021. URL: https://www.dlr.de/next/DesktopDefault.aspx/tabid-6628/10887_read-24703/gallery-1/gallery_read-Image.69.14960/.

[61] C. Willert and J. Kompenhans. "PIV Analysis of Ludwig Prandtl's Historic Flow Visualization Films". In: (2010), pp. 1–4. arXiv: 1010.3149. URL: http://arxiv.org/abs/1010.3149.

[62] P.O Ayegba and L. C. Edomwonyi-Otu. "Turbulence statistics and flow structure in fluid flow using particle image velocimetry technique: A review". In: *Engineering Reports* 2.3 (2020), pp. 1–49. ISSN: 2577-8196. DOI: 10.1002/eng2.12138.

[63] M. Raffel and C.E. Willert. *Particle Image Velocimetry. A practical guide*. 2017. ISBN: 9783319688510. DOI: 10.3139/9783446436619.

[64] M. Hamdi et al. "Comparison of different tracers for PIV measurements in EHD airflow To cite this version : HAL Id : hal-01833545 Comparison of different tracers for PIV measurements in EHD airflow". In: *Experiments in Fluids* 55 (2014), p. 1702.

[65] R.D. Keane and R.J. Adrian. "Optimization of particle image velocimeters. I. Double pulsed systems Optimization of particle image ve I oci m e te rs. Part I: Double pulsed systems". In: *Meas. Sci. Technol. Meas. Sci. Technol* 1.1 (1990), pp. 1202–1215. URL: http://iopscience.iop.org/0957-0233/1/11/013.

[66] W. Thielicke and E.J. Stamhuis. "PIVlab – Towards User-friendly, Affordable and Accurate Digital Particle Image Velocimetry in MATLAB". In: *Journal of Open Research Software* 2 (2014). ISSN: 2049-9647. DOI: 10.5334/jors.bl.

[67] W. Thielicke. "The flapping flight of birds Digital Particle Image Velocimetry". In: *University of Groningen The* (2014).

[68] J. Westerweel, G.E. Elsinga, and R.J. Adrian. “Particle image velocimetry for complex and turbulent flows”. In: *Annual Review of Fluid Mechanics* 45.January (2013), pp. 409–436. ISSN: 00664189. DOI: 10.1146/annurev-fluid-120710-101204.

[69] S. M. Pizer et al. “Adaptive Histogram Equalization and Its Variations.” In: *Computer vision, graphics, and image processing* 39.3 (1987), pp. 355–368. ISSN: 0734189X. DOI: 10.1016/S0734-189X(87)80186-X.

[70] J. Westerweel and R.J. Adrian. *Particle Image Velocimetry*. Cambridge University Press, 2011. ISBN: 9780521440080.

[71] M. Raffel et al. “Analytical and experimental investigations of dual-plane PIV”. In: *Optical Techniques in Fluid, Thermal, and Combustion Flow* 2546.September 1995 (1995), p. 75. ISSN: 0277786X. DOI: 10.1117/12.221511.

[72] R. J. Adrian, C. D. Meinhart, and C. D. Tomkins. “Vortex organization in the outer region of the turbulent boundary layer”. In: *Journal of Fluid Mechanics* 422 (2000), pp. 1–54. ISSN: 00221120. DOI: 10.1017/S0022112000001580.

[73] H. Huang, D. Dabiri, and M. Gharib. “On errors of digital particle image velocimetry”. In: *Measurement Science and Technology* 8.12 (1997), pp. 1427–1440. ISSN: 09570233. DOI: 10.1088/0957-0233/8/12/007.

[74] D. Dabiri. “Cross-Correlation Digital Particle Image Velocimetry-A Review”. In: *Department of Aeronautics & Astronautics Box 352400 University of Washington* (2006), pp. 1–54.

[75] R. J. M. Bastiaans. *Cross-correlation PIV; theory, implementation and accuracy*. Vol. 99. 1993. 2000, p. 39. ISBN: 903862851X.

[76] J. Westerweel, D. Dabiri, and M. Gharib. “The effect of a discrete window offset on the accuracy of cross-correlation analysis of digital PIV recordings”. In: *Experiments in Fluids* 23.1 (1997), pp. 20–28. ISSN: 07234864. DOI: 10.1007/s003480050082.

[77] B. Wieneke. *PIV Uncertainty Quantification and Beyond*. December. 2017, p. 211. ISBN: 978-94-92516-88-6. DOI: 10.13140/RG.2.2.26244.42886.

[78] F. Scarano and M. L. Riethmuller. “Advances in iterative multigrid PIV image processing”. In: *Experiments in Fluids* 29.SUPPL. 1 (2000). ISSN: 07234864. DOI: 10.1007/s003480070007.

[79] R.D. Keane and R.J. Adrian. “Theory of cross-correlation analysis of PIV images”. In: *Applied Scientific Research* 49.3 (1992), pp. 191–215. ISSN: 00036994. DOI: 10.1007/BF00384623.

[80] J. Westerweel and F. Scarano. “Universal outlier detection for PIV data”. In: *Experiments in Fluids* 39.6 (2005), pp. 1096–1100. ISSN: 07234864. DOI: 10.1007/s00348-005-0016-6.

[81] A. M. Hoving et al. “A Systematic Review for the Design of In Vitro Flow Studies of the Carotid Artery Bifurcation”. In: *Cardiovascular Engineering and Technology* 11.2 (2020), pp. 111–127. ISSN: 18694098. DOI: 10.1007/s13239-019-00448-9.

[82] S. G. Yazdi et al. “A Review of Arterial Phantom Fabrication Methods for Flow Measurement Using PIV Techniques”. In: *Annals of Biomedical Engineering* 46.11 (2018), pp. 1697–1721. ISSN: 15739686. DOI: 10.1007/s10439-018-2085-8.

[83] M.C. Brindise, M. Busse, and P. Vlachos. "Density- and viscosity-matched Newtonian and non-Newtonian blood-analog solutions with PDMS refractive index". In: *Experiments in Fluids* 0.0 (2018), p. 0. ISSN: 1432-1114. DOI: 10.1007/s00348-018-2629-6. URL: http://dx.doi.org/10.1007/s00348-018-2629-6.

[84] O. San and A.E. Staples. "An improved model for reduced-order physiological fluid flows". In: *Journal of Mechanics in Medicine and Biology* 12.3 (2012). ISSN: 02195194. DOI: 10.1142/S0219519411004666. arXiv: 1212.0188.

[85] Sonotec. *Sonotec technical data sheet, Sonoflow*. Accessed: 10-01-2021. URL: https://www.sonotec.eu/fileadmin/user_upload/business_units/1-non-invasive-fluid-monitoring/products/ultrasonic-flow-meter/sonoflow-co-55/td-sonoflow-co-55-v2-0-en-sonotec.pdf.

[86] Vivitro Labs. *Vivitro Superpump*. Accessed: 10-04-2021. URL: https://vivitrolabs.com/wp-content/uploads/2018/09/1764_ViVitro_SalesSheetJuly2018_SuperPump.pdf.

[87] B. Vennemann and T. Rösgen. "A dynamic masking technique for particle image velocimetry using convolutional autoencoders". In: *Experiments in Fluids* 61.7 (2020), pp. 1–11. ISSN: 14321114. DOI: 10.1007/s00348-020-02984-w. URL: https://doi.org/10.1007/s00348-020-02984-w.

[88] Bronkhorst High-Tech BV. *Bronkhorst-propar Python package*. Accessed: 15-10-2020. URL: https://www.bronkhorst.com/int/products/accessories-and-software/flowware/python/.

[89] W. Wen et al. "The influence of bubbles on the performance of ultrasonic flow meter". In: *Applied Mechanics and Materials* 678 (2014), pp. 285–289. ISSN: 16627482. DOI: 10.4028/www.scientific.net/AMM.678.285.

[90] K. Bai and J. Katz. "On the refractive index of sodium iodide solutions for index matching in PIV". In: *Experiments in Fluids* 55.4 (2014). ISSN: 07234864. DOI: 10.1007/s00348-014-1704-x.

[91] M. L. Byron and E. A. Variano. "Refractive-index-matched hydrogel materials for measuring flow-structure interactions". In: *Experiments in Fluids* 54.2 (2013). ISSN: 07234864. DOI: 10.1007/s00348-013-1456-z.

[92] E. R. Polanco et al. "Fabrication of refractive-index-matched devices for biomedical microfluidics". In: *Journal of Visualized Experiments* 2018.139 (2018), pp. 2–7. ISSN: 1940087X. DOI: 10.3791/58296.

[93] Y. Matsuda et al. "Three-dimensional flow measurements around micro-pillars made by UV-NIL in water via micro-digital holographic particle tracking velocimetry (Micro-DHPTV)". In: *Journal of Photopolymer Science and Technology* 33.5 (2020), pp. 557–562. ISSN: 13496336. DOI: 10.2494/photopolymer.33.557.

[94] A Bakker. "CFD, Kolmogorov's Theory". In: *Darmouth College* (2005).

[95] S. D. Peterson and M. W. Plesniak. "The influence of inlet velocity profile and secondary flow on pulsatile flow in a model artery with stenosis". In: *Journal of Fluid Mechanics* 616.December (2008), pp. 263–301. ISSN: 00221120. DOI: 10.1017/S0022112008003625.

[96] D. Orešković and M. Klarica. "A new look at cerebrospinal fluid movement". In: *Fluids and Barriers of the CNS* 11.1 (2014), pp. 1–3. ISSN: 20458118. DOI: 10.1186/2045-8118-11-16.

## Appendix A

# Results of highest volumetric flow rate with the Coriolis flow sensor

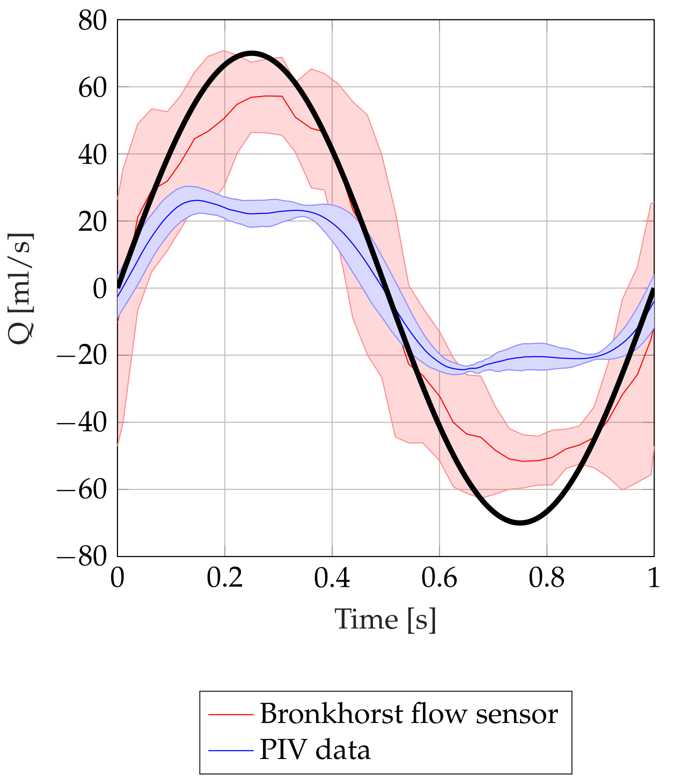


FIGURE A.1: Volumetric profile with errors bars of the PIV data and the Coriolis flow sensor. A sine waveform with a peak volumetric rate of 70 ml/s is implemented. The black line represents a perfect sine waveform.